CHARACTERIZATION OF A NEW D-D NEUTRON GENERATOR SYSTEM FOR NEUTRON ACTIVATION ANALYSIS OF MANGANESE IN BONE IN-VIVO

by

Elizabeth Helen Jaye

A Thesis

Submitted to the Faculty of Purdue University

In Partial Fulfillment of the Requirements for the degree of

Master of Science

School of Health Sciences

West Lafayette, Indiana

May 2022

THE PURDUE UNIVERSITY GRADUATE SCHOOL

STATEMENT OF COMMITTEE APPROVAL

Dr. Linda Nie, Chair

Department of Health Sciences

Dr. Aaron Bowman

Department of Health Sciences

Dr. Keith Stantz

Department of Health Sciences

Approved by:

Dr. Aaron Bowman

To my parents, Jim and Elaine, whose unwavering love, support, and encouragement have helped me reach heights I never thought I could.

ACKNOWLEDGMENTS

I would like to express my sincere gratitude to Dr. Linda Nie who has been the most incredible advisor and mentor to me over the last two years. Her instruction, advice, guidance, and kindness have been some of the greatest highlights of my graduate experience. I have learned so much from her, not only about the subject matter of the research, but about being a good researcher, scholar, and person. No matter how busy she was, she would always make time for me and my questions; always responding with optimism and encouragement. Without her support, this work would not have been possible.

I am also grateful to my committee members Dr. Keith Stantz and Dr. Aaron Bowman. They have been supportive since the beginning of this work and have given me great suggestions for ways to improve my work. Also, I want to recognize my lab members, Patrick, Sana, Alexis, and Song. It was such an honor and pleasure to learn from them, work with them, and get to know them as friends.

TABLE OF CONTENTS

LIST OF TABLES

LIST OF FIGURES

ABSTRACT

Neutron Activation Analysis (NAA) is a non-invasive method for assessing the qualitative and quantitative elemental composition of a sample. One application of this technique is in-vivo quantification of specific elements in the human body. An important element in terms of human exposure assessment is Manganese (Mn). Mn is the fourth most used industrial metal and can be an inhalation exposure hazard specifically for welders. Over exposure to Mn can lead to neurological degeneration issues similar to Parkinson's disease. It has been found that bone is a good biomarker for Mn as Mn is deposited in the bone and remains for long periods of time, allowing for an assay to reveal long term exposure information. The method of using NAA to quantify levels of Mn in-vivo using the bones in the human hand is being explored in this work. The NAA system used, involves a deuterium-deuterium neutron generator and an N-type High Purity Germanium Detector. It is critical to have the performance of the entire system characterized using phantoms and cadaver bones before the system can be used for in-vivo measurements. The goal of this work is to determine the neutron yield of the generator system, the neutron and photon dose received by a sample, the detection limit of Mn with this system, and to evaluate the Mn detection capability of the system using cadaver bones from occupationally exposed Mn miners. The parameters were determined through a combination of simulation with Monte Carlo N-Particle Code (MCNP), experiments using Mn doped bone phantoms and cadaver bones, and various dosimetry tools such as TLDs and EPDs. The neutron yield for the D-D 109M generator was estimated to be 2.24E+09 +/- 2.15E+07 neutrons per second for this work. The Mn detection limit for the system was estimated to be 0.442 ppm. The equivalent dose received by the sample during the standard 10-minute irradiation was estimated to be 8.45 +/- 2.05 rem. The results found for the human cadaver bones were mixed. It was found that the system was able to successfully detect Mn in cadaver bones. Unexpectedly, however, three of the samples showed little to no Ca signal. In addition, significant amounts of soft tissue and bone marrow exist in the samples. Therefore the Mn concentration in the bones was not able to be accurately estimated. A relative metric of Mn concentration was used instead and showed a slight positive increase from the unexposed to exposed samples but was not statistically significant.

CHAPTER 1. INTRODUCTION

1.1 Manganese in the Human Body

1.1.1 Manganese as an Essential Nutrient

Manganese (Mn) is an element essential for the optimal function of the human body. It is a transition metal that serves as a structural and catalytic cofactor for many proteins and enzymes created in the body[1]. Several examples of these enzymes that rely on Mn are Superoxide dismutase, Pyruvate carboxylase, and Aminopeptidase[2]. It has been found in animal and human studies that insufficient levels of Mn can lead to dermatitis, decrease in HDl cholesterol levels, and osteoporotic effects on the bones[2]. The effects seen from Mn deficiencies illustrate the essential role Mn plays in many areas of the body. Optimal levels of Mn in the body have been found to range from 0.3 to 2.9 ppm depending on the tissue[1]. Tissues with high metabolic activity such as bone, liver, and kidney will have higher concentrations of Mn than other tissues.

Humans regularly take in the essential Mn they need as it is readily found in our environment. It is the twelfth most abundant element on Earth[3]. Mn is mainly found in the Earth's crust but as natural erosion occurs, the Mn is liberated and deposited into the soil, air, and waterways. This allows for humans to take in Mn through breathing it in the air, drinking it in water, and eating crops that were grown in soil containing Mn. The majority of Mn intake is through consumption of water and food. Drinking water contains various concentrations of Mn depending on geographical location but it typically ranges from 1 μg/L to 2 mg/L[3]. Foods that contain the highest levels of Mn are rice, nuts, whole grains, and legumes[3].

When Mn is taken in via ingestion, only 3-5% of the amount ingested is absorbed by the GI tract[3]. The Mn is absorbed by the cells in the intestinal wall through passive diffusion and active transport and makes its way into the blood stream. It has been found that women typically have a 30% greater absorption of Mn by the GI tract than men[3]. If taken in via inhalation, the Mn is absorbed in the lung tissue and then enters the blood stream. Once the Mn gets into the blood stream it is quickly delivered to different tissues throughout the body. Within the blood, normal concentrations of Mn range from 4-15 μg/L[3]. The tissues with the highest concentrations of Mn are the liver, pancreas, bone, kidney, and brain. Notably for this work, Mn accumulates readily in

bone with normal concentrations around 1 ppm[3]. This corresponds to 40% of the total body Mn being stored in the bone[3]. Mn is stored in the bone for longer periods of time, as compared to other soft tissue and fluid compartments, which along with its high accumulation of Mn makes it an excellent biomarker for measuring Mn levels in humans.

1.1.2 Manganese Toxicity

Although Mn is critical for many processes in the human body, too much can lead to toxicity. Overexposure to Mn can lead to neurodegenerative damage that can lead to a syndrome called Manganism which is closely related to Parkinson's disease. In most cases of overexposure, the Mn is inhaled by workers in occupational settings such as mining and welding. During the mining and welding processes, small particles of Mn are broken off and become airborne. In a study performed by Zheng of Mn-poisoned welders in Beijing China, it was found that one welding site had airborne Mn levels of 25.7 mg/m^3 which is 128 times higher than the Chinese national standard limit[4]. From this same study, it was also found that the blood Mn levels of the workers ranged from 3-36µg/L and urine Mn levels ranged from 2-30µg/L[4].

When Mn gets into the blood stream it can enter the brain via three pathways which are entrance via the olfactory nerve in the nasal cavity, entrance via the capillaries of the blood-brain barrier, and entrance through the choroid plexus of the CSF-blood barrier[4]. Although the brain receives lower levels of Mn than other tissues in the body (around 0.1% of the total blood Mn[3]), it is the most susceptible organ to Mn toxicity. One hypothesis for why neurons are more susceptible to Mn damage than other cells is that they have a longer life span and higher energy demand[3]. Once the Mn enters the brain, it targets and creates dysfunction in neurons in the globus pallidus and striatum of the basal ganglia[4]. The exact mechanism behind the neurotoxicity is not well understood but it is hypothesized that elevated Mn levels may trigger increased iron uptake in the body. These increased levels of iron in neuronal cells can produce oxidative stress that leads to neuronal damage[4]. This neuronal damage leads to symptoms including headaches, insomnia, memory loss, emotional instability, hand tremors, speech disturbances, and festinating gait. Very extreme cases result in the patient having a "cock-walk" in which they walk on their toes and lean forward. In occupationally overexposed individuals, these symptoms begin to show, on average, 16 years after the initial exposure[4]. It has been found that longer periods of overexposure lead to a greater number of symptoms and more severe symptoms.

1.2 Manganese Biomarkers and Measurement Methods

When looking to measure the amount of Mn in the human body, an appropriate biomarker must be chosen and evaluated. According to the NIH, a biomarker is "An objective measure that captures what is happening in a cell or an organism at a given moment[5]." Specifically, an exposure biomarker gives information about the levels of a certain chemical inside the body. To study Mn exposure there have been several biomarkers used throughout the years.

The most extensively studied and used biomarker for Mn exposure is Mn concentration in the blood. As discussed in section 1.1.1, once Mn is taken in through ingestion or inhalation it is absorbed by the GI tract and lungs and enters the blood stream. Therefore, one would think that taking a blood sample and measuring the Mn concentration would be a good indicator of Mn exposure. Also, the simplicity of a blood draw makes this an easy biomarker to collect and study. Studies measuring the blood Mn levels of occupationally exposed workers have unfortunately found it to not be a very promising biomarker. The studies found that blood Mn can only indicate recent and active exposures and it is only a modest way of differentiating between Mn-exposed workers and controls at an individual level[6]. This is likely because Mn is cleared from the blood very quickly. The biological half-life for Mn in blood plasma is less than 2 hours[6]. Because of this, blood Mn levels cannot be counted on to provide accurate, long term exposure information.

Other biomarkers for Mn exposure that have been explored are saliva, urine, hair, feces, and toenails. All of these biomarkers would be very simple to collect non-invasively. It was found that the performance of saliva as a Mn biomarker was equal to that of blood. Urine was not a successful Mn biomarker because the majority of Mn is cleared via feces and therefore the Mn concentration in urine is not representative of the total body burden. In studies looking at hair as a Mn biomarker, there were large increases in the Mn hair concentration in exposed dry-cell battery plant workers and Mn smelters. The authors of this study concluded that the large increase in Mn concentration may be coming from external contamination depositing from the air onto the workers' hair. This makes it difficult to assess how much Mn came from inside the body and how much was due to external contamination. Finally, it was found that with feces and toenails that there was significant variation in Mn concentration between samples taken from exposed workers. This large variation suggests that these are likely not reliable biomarkers.

A Mn exposure biomarker that has been researched more recently is Mn concentration in bone. As discussed in section 1.1.1, about 40% of the total Mn in the body is stored in the bone

which makes it a promising biomarker candidate. One reason that it was not studied as much as blood and other bodily fluids is that there was initially no way to take a non-invasive assay of the bone of a living person. Advances in technology, especially in the area of neutron activation analysis, have made non-invasive bone assays possible. This has opened the door for using bone as a biomarker. One major advantage to using bone as opposed to blood, is that it is believed that Mn stays within the bone for years after exposure and may continue to accumulate over a lifetime. If this is true, it will allow for data to be extracted about a person's Mn exposure long after the exposure has occurred and give an idea about the total exposure they have received. A recent study by Conley et. Al from 2022 found that bone Mn was more sensitive to elevated Mn exposures than blood Mn or brain Mn[7]. In order to estimate how Mn levels would change over a lifetime, Conley studied the bone Mn concentration in rats throughout their lifespan. They found that in control mice that did not receive elevated Mn, the bone Mn concentrations naturally decreased across the lifetime. In mice that received prolonged elevated Mn, the levels of Mn bone concentration were elevated compared to the control mice. However, this elevated level remained fairly constant throughout the lifetime of the mice. No accumulation effect was observed, showing that being exposed to more and more Mn will not keep increasing the Mn bone concentration. [7]. This may indicate that bone will not be able to give as accurate of a cumulative lifetime exposure estimate as originally thought but it is still a good long-term exposure biomarker.

1.3 Neutron Activation Analysis

Neutron activation analysis (NAA) is a technique that is used to both qualitatively and quantitatively assess the elemental composition of a sample. NAA allows for the detection of major elemental components as well as elements present in trace amounts. It provides detection sensitivities far superior to other analysis methods [8]. One of the other major advantages of NAA over other elemental analysis techniques is that it is completely non-invasive and non-destructive to the sample. This makes it an ideal candidate for in-vivo measurements.

The crux of NAA is the neutron capture reaction with the target element of interest. Neutrons are neutral subatomic particles and because of their lack of charge, they can easily penetrate through the coulomb field of the electron cloud and get close to the nucleus. At this close distance, it is possible that the neutron will enter and be captured by the nucleus. The likelihood that the neutron will be captured by the nucleus varies based on its energy as well as the target

element that it is interacting with. This probability of being captured is represented by the neutron absorption cross section which is unique for each element and varies with the energy of the neutron. The unit of cross section is 10^{-24} cm which is given a special unit called barns [9]. As the energy of the neutron gets lower, the neutron absorption cross section increases, with the largest cross sections being for thermal neutrons. Thermal neutrons have energies below 0.5 eV. At these low energies, the neutrons are moving slowly and therefore spend more time near the nucleus, allowing more opportunity for capture to occur.

Once the neutron has been captured by the nucleus, a compound nucleus is formed. This compound nucleus is in an excited energy state and is therefore unstable. In order to return to its preferred lower energy state, the compound nucleus will undergo radioactive decay, typically beta decay since it has an excess of neutrons. Along with a beta particle and antineutrino, a gamma ray is often emitted during beta decay. For all atoms of the same element, the gamma ray or rays released after the neutron capture reaction will always have the same energies. These gamma ray energies are characteristic to each element.

The final stage of the NAA process is to detect and count the gamma rays produced from the decaying compound nucleus. In this work, the gamma rays were detected using a High Purity Germanium detector (HPGe). A HPGe detector allows for excellent energy resolution between gamma ray peaks so that the counts from the isotope of interest can be resolved from any other nearby peaks.

1.3.1 Neutron Activation Analysis for Manganese

The target element of interest for this work is Manganese 55 (Mn-55). This is a stable element with 25 protons and 30 neutrons. The neutron absorption cross section for Mn-55 is shown in Figure 1.1. As seen in Figure 1.1, the neutron absorption cross section increases with a 1/v relationship for energies lower than ~100 eV. It is therefore advantageous to use thermal neutrons in order to enhance the neutron capture by the Mn-55 atoms.

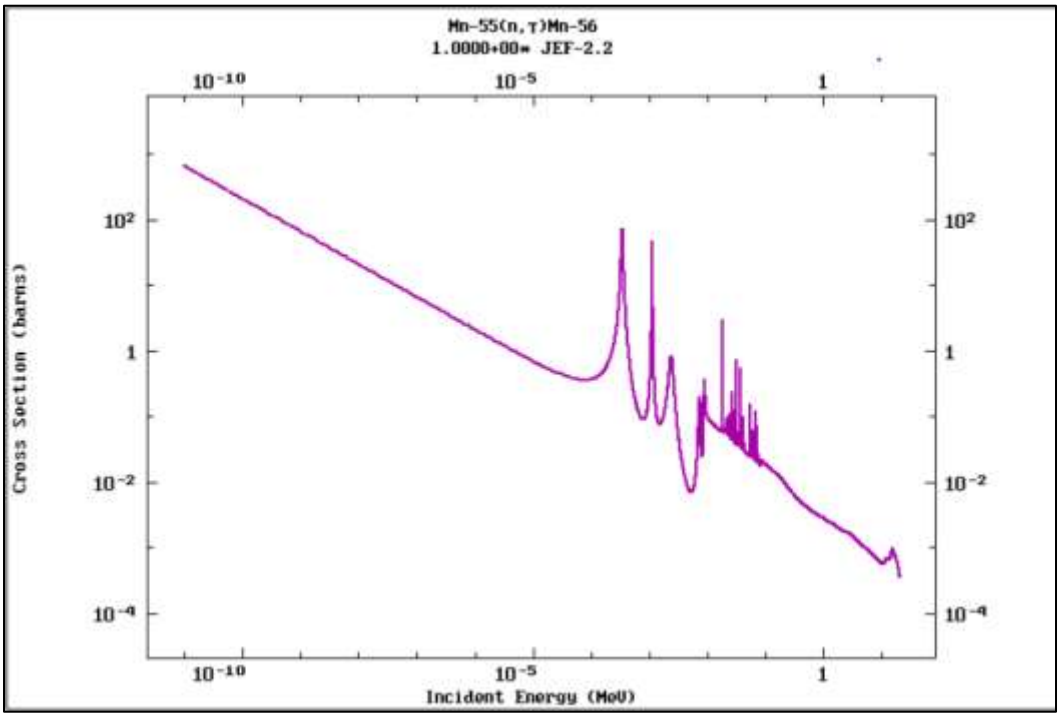

Figure 1.1. Neutron Absorption Cross Section for Mn-55 [10]

The reaction utilized in this work for the activation of Mn-55 is presented in Equation 1.

$$^{55}_{25}Mn + n \rightarrow {}^{56}_{25}Mn^{*} \rightarrow {}^{56}_{26}Fe + \beta^{-} + \bar{\nu} + \gamma\ [846.8\ keV] \qquad (1)$$

In the equation above, the superscripts represent the mass number of the isotope while the subscripts represent the atomic number. The unstable Mn-56 has a half-life of 2.58 hours and decays via beta decay to the stable Fe-56. The branching ratio for the 846.8 keV gamma is 98.9% meaning that a gamma of this energy will be emitted 98.9% of the time that this isotope decays [11].

1.3.2 Neutron Source

The neutrons used in this work were produced using the deuterium-deuterium fusion reaction which is given by Equation 2.

$$^{2}_{1}H^{+} + {}^{2}_{1}H^{+} \rightarrow {}^{3}_{2}He + {}^{1}_{0}n + 3.27\ MeV \qquad (2)$$

Naturally, the two deuterium ions repel each other due to their electrostatic repulsion. Therefore, “activation energy” is required to overcome the repulsive forces and fuse the two deuterium ions into one, heavier nucleus[12]. This energy is provided through acceleration of one ion toward the other. The fusion process results in the production of a Helium-3 atom, a neutron of energy 2.45 MeV, as well as 3.27 MeV of excess energy.

As discussed previously, the ideal neutron energy for use in NAA is in the thermal range. In order to slow down the 2.45 MeV fast neutrons produced from DD fusion, hydrogenous materials are used for moderation. Since a neutron is of a similar size to a hydrogen atom, it loses the maximum amount of energy possible during elastic scattering events with hydrogen compared to other, higher Z elements. Because of this large energy loss, it takes fewer interactions to moderate the neutron down to a thermal energy. The hydrogenous material used in this work his high-density polyethylene which has the chemical formula C_2H_4.

1.3.3 Monte Carlo Simulation of Mn NAA

An important tool for both experimental planning and validation is simulation. Simulation allows the user to have a prediction of what will happen experimentally as well as allow them to see how changing different parameters will affect experimental outcomes without having to spend the time and money to make those physical changes. The simulation in this work was done using the Monte Carlo code, Monte Carlo N-Particle 6 (MCNP6). According to the user manual, “MCNP is a general-purpose, continuous-energy, generalized-geometry, time-dependent, Monte Carlo radiation-transport code designed to track many particle types over broad ranges of energies.”[13] It allows the user to create unique geometries, material compositions, specific source definitions, and a variety of output tallies.

There are three major components that make up an MCNP simulation input file; the cell card, surface card, and data card. The surface card is where the geometry is defined. Surfaces can be defined using 2-dimensional planes and 3-dimensional volumes known as macrobodies. Once the surfaces have been defined, the cell card can be generated. The cell card defines volumes within the geometry and assigns them a specific material composition. All volumes of the geometry in the input file must be defined by a single cell and there can be no overlap between cell volumes. Finally the data card contains all other information including the type of particles being simulated (photon, electron, neutron), the importance of each particle type, the source specification, material

definitions, tally specifications, and the number of particles to be simulated. For this work 1E+06 particles were simulated.

1.3.3.1 Irradiation Simulation

To simulate the irradiation and therefore neutron activation of samples by the neutron generator system, a unique MCNP6 input file was created. The main goal of this file was to provide neutron activation information as well as radiation dose information. Since neutron activation requires the use of thermal neutron interactions, special modifiers needed to be used in this file. For materials such as the moderator and reflector, in which the majority of thermal neutron interactions are occurring, it is essential that the scattering events are correctly modeled. By using the modifier, MT, MCNP will draw scattering cross section data from a library based on the S(alpha, beta) scattering law for thermal neutrons. The interaction cross sections from this library will only be used for particles below 2 eV. For all energies above 2 eV, the cross section data is based on the free-gas model[13]. An example of the MT modifier in use is given below.

```
mt236 grph.10t
```

This is a material modifier line for the material defined by number 236 which in this case was graphite. This signals the software to draw specific thermal neutron cross section data from this graphite library whenever there is a particle below 2eV in a cell with material defined as graphite.

1.3.3.2 γ Detection Simulation

An N-type HPGe detector was used in this work to detect the gamma signal produced from NAA. When performing experiments with signals as low as those from NAA, it is critical that the detection system being used is well characterized. Most important is the system's detection efficiency for energies of interest. In order to simulate the detection efficiency of our N-type HPGe detector, and MCNP input file was created. An experimental test as well as a simulated test were completed using a multi-nuclide vial source which gave off photons of a wide range of energies.

The simulation was modified in order to match the simulated efficiencies to the experimental efficiencies.

1.4 In-Vivo Neutron Activation Analysis

The phrase in-vivo comes from the Latin word *vivere* which means “to live” and thus means “within a living organism.”[14] The end goal of this research work is to translate these experiments to in-vivo Mn assays using the human hand. The subject will place their hand in the irradiation cave while there body remains well shielded by the polyethylene assembly. It is therefore critical to determine the radiation dose that will be received by a participant. The occupational dose limit set by the NRC is a total effective dose of 5 rem annually and a committed dose equivalent to any individual organ or tissue of 50 rem [15]. Since the hand is considered an individual tissue, the limit of 50 rem is the pertinent limit. In order to be conservative, a value 10% of this limit (5 rem) will be used as the guiding limit to stay within for this work.

CHAPTER 2. CHARACTERIZATION OF THE NEUTRON ACTIVATION AND DETECTION ABILITY FOR MANGANESE

2.1 Introduction

As mentioned in Chapter 1, it is critical to evaluate and characterize the performance of the neutron activation analysis system for Mn detection. Before transitioning this system for in-vivo use in humans, its ability to detect Mn in bone must first be demonstrated and validated with simulation and experiments. The critical parameters to estimate are the neutron flux of the generator, the amount of Mn activation that occurs in a sample, the amount of the activated Mn signal that is measured by the HPGe system, and the minimum detectable concentration of Mn.

This chapter contains a detailed description of the neutron generator system and HPGe detector system used as well as the creation of MCNP simulations of both. The MCNP simulation of the neutron generator system is used to simulate the amount of Mn activation expected in bone phantoms irradiated by the system. This information is used to create a simulated calibration curve of Mn signal detected versus Mn concentration in a sample. The HPGe simulation is used to estimate detection efficiencies of the detector which is needed to estimate the neutron yield of the generator through gold foil activation. Finally, the chapter concludes by discussing Mn bone phantom experiments. The results from these experiments are used to estimate the detection limit of the system.

2.2 Materials and Methods

2.2.1 Neutron Generator Irradiation System

2.2.1.1 Neutron Generator

The neutron generator used in this work is a model DD-109M generator from Adelphi Technologies, Inc. This generator makes use of the deuterium-deuterium fusion reaction to produce a large yield of fast neutrons which are moderated to the thermal regime by an integrated moderator. The major components of the generator are the generator head, heat exchanger, deuterium supply, and the electronics rack.

A schematic of the generator head is shown in Figure 2.1. The entire generator head is kept at a low vacuum pressure by an active turbo and roughing pump that run constantly during operation. Keeping the head at vacuum pressure ensures that there is no air or other substances that could interfere with the fusion reaction or cause electrical arcing. The next major component is the Electron-Cyclotron Resonance (ECR) plasma source. The ECR is driven by a microwave source that produces microwaves using a magnetron and waveguide tuner. These microwaves are used by the ECR to ionize the deuterium gas into high density D+ ion plasma. The D+ ions are then accelerated toward a titanium target housed within the acceleration chamber. This is done by establishing a negative bias on the target to create a large potential. The first D+ ions that strike the target become implanted on the surface and form titanium hydrate. From here, subsequent ions that strike the target will interact with ions imbedded in the target[16]. The large acceleration gives the ions enough energy to undergo fusion and thus produce neutrons.

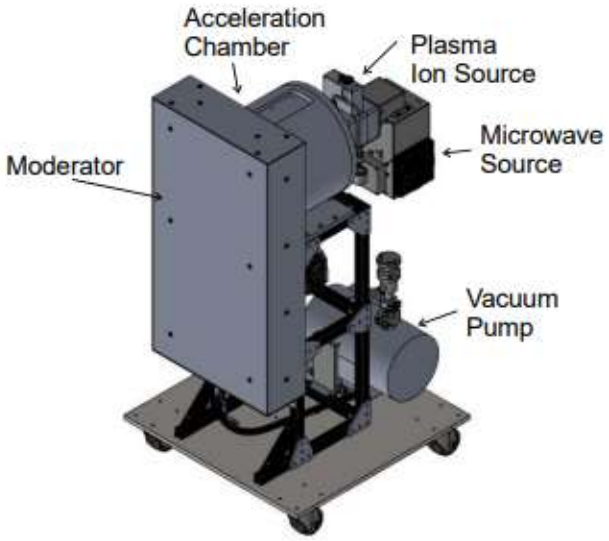

Figure 2.1. D-D 109M Generator Head[16]

The fusion reaction produces a large amount of heat, as do the high voltage electrical components. Therefore, the system must be well cooled to prevent overheating. Coolant is flowed through the target using a Neslab Merlin M150 heat exchanger and an additional EXC-800 Chiller from Koolance is used to cool the magnetron and ion source. The deuterium is supplied to the ECR

from a bottle of compressed gas with a supply line. The flow and input pressure of the gas can be controlled using 3 regulating valves. The electronics rack contains the high voltage power supply for the system as well as all communication and control equipment. An Ethernet cable is used to connect the electronics rack to a laptop computer with the *Adelphi Control GUI* that is used to adjust parameters and run the system.

2.2.1.2 Irradiation Assembly

The irradiation assembly used for this work is centered around the DD 109M generator. Since the end goal of this work is to use this system for in-vivo measurements, the system needs to be well shielded to reduce the dose to participants. Additional moderation was also needed to further thermalize the neutron flux beyond the capability of the built-in moderator. To meet these needs, a custom high-density polyethylene moderation and shielding assembly was constructed around the generator. A photo of the assembly is shown in Figure 2.2.

Figure 2.2. Custom Shielding Assembly Surrounding Generator

There are roughly 20 inches of polyethylene to both the left and right, 10 inches above, and 24 inches distal to the generator head. There is also an open area for placing samples for irradiation as can be seen on the left in Figure 2.2. This is referred to as the irradiation cave. There is an

additional 11 cm of polyethylene between the built-in moderator and the edge of the irradiation cave. The dimensions of the cave are 10cm x 8cm x 10cm.

2.2.1.3 MCNP Simulation of Irradiation Assembly

MCNP6 was used to create a simulation of the entire neutron irradiation assembly. This work was started using a pre-existing input file for the system created by former group member Patrick Byrne. The geometry of the existing input file was edited to more accurately represent the system in its current state. This consisted mostly of making adjustments to the moderation assembly as the neutron generator itself remained unchanged. Visual Editor was used extensively to visualize the geometry of the input file and a final rendering of the geometry can be seen in Figure 2.3. This figure represents a cross sectional cut of the system in order to see the generator head and the irradiation cave.

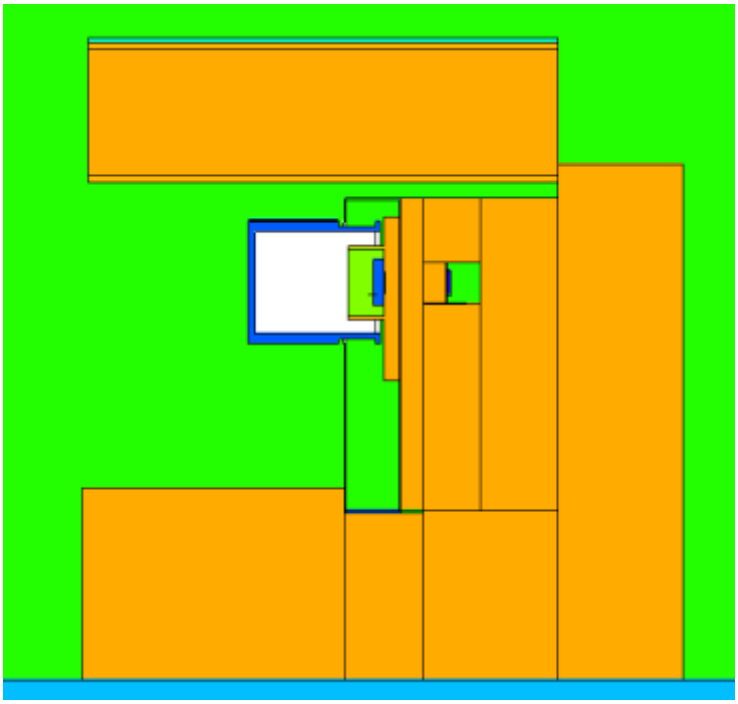

Figure 2.3. Visual Editor Representation of the MCNP Neutron Generator System Geometry

An important feature that needed to be added to the model was the Mn bone phantoms. Preexisting physical bone phantoms created by former group member Michal Abel were used as

the template for the phantoms in the simulation. These phantoms were cylinders with 8.5 cm diameter and 1 cm height. Each had a unique concentration of Mn ranging from 0 to 40ppm. The composition of the phantoms is a mixture of Ca, S, O, H, N, Cl, Na, Mg, and Mn in ratios matching those stated by ICRP for human bone. A sample of the material definition line of 1 ppm manganese bone phantom is given below.

```
m12   1001.70c       -0.0228  $1ppm (1.3291E-08)
7014.70c      -0.00559 16032.70c   -0.18111 25055.70c   -1.1e-06
11023.70c     -0.00713 8016.70c    -0.55543 20040.70c   -0.22251
17035.70c     -0.00311 12024.70c   -0.00232
```

m12 represents that this material has been designated as “material number 12.” The numbers without a minus sign represent the unique Z and A identification numbers of each isotope in the format ZZZAAA where ZZZ is the atomic number and AAA is the mass number. The .70c indicates which cross section library is to be used for each isotope. The numbers with the minus sign represent the fractional amount of that isotope in the total composition of the material. Material identification lines are needed for all materials used. As discussed in section 1.3.3.1 MT modifiers were used for polyethylene, graphite and aluminum.

Neutrons, photons, and electrons were included in this simulation with an equal importance of 1 in all cells and a total number of particles of 1E+06 was used. Various flux and dose tallies were included and will be discussed later in Chapter 3. The important tally for modeling the neutron activation of the system is the F4 flux tally combined with the FM4 modifier. This tally outputs the number of activated target atoms in the volume of a specified cell per source neutron per second. An example of the format of this tally is shown below.

```
F4:N CellNumber

FM4 Multiplier MaterialNumber 102

SD 1
```

The first line creates a tally of average neutron flux in the specified cell. The second line acts to modify this tally. The material number is the unique MCNP ID number chosen for the material of interest which in this work was 25 for Mn. 102 specifies the radiative capture cross section library to be used. The multiplier is a number that must be calculated using Equation 3.

$$Multiplier = \frac{\left(\frac{mass}{V}\right)*N_A}{M} * 10^{-24} \left[\frac{atom}{barn\ cm}\right] \quad (3)$$

Mass = Mass of the element of interest within the volume

V = Volume of the cell

N_A = Avogadro's Number

M = Atomic number of the element of interest

10^{-24} = Conversion from cm to barns

The default output of this tally has units of activated atoms per cm^3. By including SD 1, the default output is multiplied by the volume of the cell. This results in the final output representing the activation of the specified element in the volume of the cell.

2.2.1.4 Calculating the Simulated Activated Mn Gamma Counts

The activation tally output from the previous section is used to calculate the expected number of counts due to activated Mn-56 that would be seen after a phantom is irradiated and measured with the HPGe detector. The equation used to determine the counts is given by Equation 4.

$$Counts = (R\ x\ F_n\ x\ S)\ x\ D\ x\ C\ x\ \epsilon\ x\ \theta \quad (4)$$

R = MCNP Activation tally output; number of atoms activated per source neutron per second

Fn = Yield of the neutron generator; neutrons per second

S = Correction factor for saturation activity being reached

D = Correction factor for decay occurring during the set decay period between irradiation and counting

C = Correction factor accounting for decay during the counting interval

ε = Detection efficiency of the HPGe for the specific gamma energy

θ = Branching ratio of the gamma ray of interest

$$S = \left(1 - e^{-\lambda t_i}\right) \qquad D = e^{-\lambda t_d} \qquad C = \frac{(1-e^{-\lambda t_c})}{\lambda} \quad (5, 6, 7)$$

The equations for the S, D, and C correction factors are given above in Equations 5, 6, and 7. In these equations, lambda represents the decay constant for Mn-56 and the various t values represent irradiation time, decay time, and counting time respectively. The product of the three factors in parenthesis in Equation 4 gives the total number of activated Mn atoms. All other factors correct for decay and the efficiency of the detector. They are needed to determine the actual number of counts which will be measured by the detector. This number will always be less than the number of atoms that are activated because some of the signal will be lost to decay and detection inefficiency.

Using these simulated counts for each unique Mn concentration bone phantom, a calibration curve can be generated. The calibration curve has concentration of Mn in units of ppm on the x-axis and the number of counts detected on the y-axis. This relationship should be linear in nature and the slope of this linear line gives the counts expected per ppm of Mn. Generating this curve allows us to determine the concentration of Mn in an unknown sample based on the counts measured by the HPGe system. The complete MCNP input file for the neutron generator system is provided in Appendix A.

2.2.2 High Purity Germanium Detector System

2.2.2.1 High Purity Germanium Detector

The High Purity Germanium (HPGe) Detector used in this work is model GMX100P4-95-A GAMMA-X HPGe detector from ORTEC. This detector has a coaxial configuration and is an n-type. N-type means that the impurities in the semiconductor are electron donors and increase the number of conduction electrons available. A major advantage of the n-type HPGe over the p-type is that the dead layer, or region insensitive to gamma rays on the edges of the crystal, is much thinner. This allows for more efficient detection of low energy gammas with short penetration capabilities [17]. For an N-type HPGe a negative voltage bias is needed to create the depletion region which is the active volume where gamma rays can be detected. This specific detector operates with a high voltage bias of 4500 Volts. An example of the coaxial geometry and biasing is shown if Figure 2.4. Instead of the traditional liquid nitrogen cooling, this detector is electronically cooled using an X Cooler III from ORTEC.

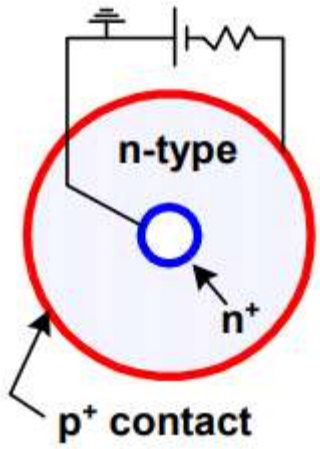

Figure 2.4. Coaxial N-type HPGe Crystal [17]

2.2.2.2 Experimental HPGe Detector Setup

For experimental use, the HPGe detector is surrounded by a custom assembly of lead bricks. This is done to isolate the detector from the outside world to prevent detection of any background radiation. Although the lead is not able to attenuate all background radiation, it greatly reduces the amount that is detected. Reducing the background as much as possible is critical in order to get the lowest Mn detection limit possible. Some photos of the assembly are given in Figure 2.5.

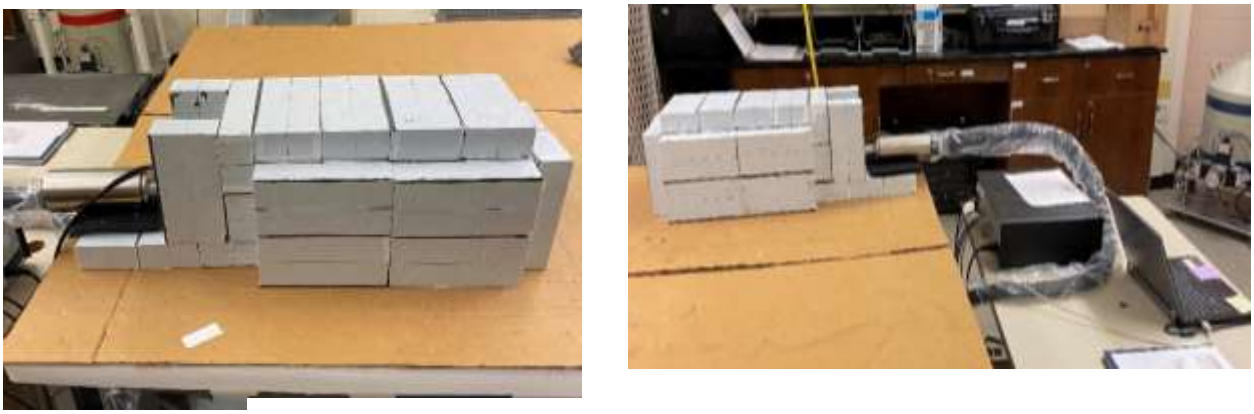

Figure 2.5. HPGe Detector System Assembly

The detector is connected to a laptop computer that has Maestro-32 Multi-Channel Analyzer Emulator software from ORTEC. The Maestro software allows the user to set all operating parameters for the detector as well as control data measurement, collection, and analysis parameters. All data collected by the detector is presented in the Maestro software as a spectrum of counts verses channel number. The channel numbers must be calibrated by the user to correspond to the correct gamma energy.

2.2.3 Bone Phantom Experiments

2.2.3.1 Bone Phantoms

As mentioned in section 2.2.1.3, the bone phantoms used in this work were created by Michael Abel, a former lab member. These phantoms were created to replicate the elemental composition of bone as stated by ICRP while also containing various concentrations of Mn. The five compounds used in various amounts to create these phantoms were $CaSO_4 * 2H_2O$, NH_4Cl, $NaNO_3$, $MgSO_4$, and $Mn(NO_3)_2$. The various concentrations of Mn used were 0, 0.5, 1, 2, 5, 10, 15, 20, 30, and 40 ppm. The geometry of the phantoms were cylinders of diameter 8.5 cm and height of 1 cm. The phantoms were vacuum sealed in plastic bags to protect them from damage or contamination. A picture of one of the bone phantoms is shown in Figure 2.6.

Figure 2.6. Mn Bone Phantom

2.2.3.2 Experimental Phantom Irradiation Procedure

For the irradiation of the Mn bone phantoms, each phantom was placed in the irradiation cave flush with the left wall of the cave. This is the wall proximal to the neutron source. The parameters used to produce neutrons with the generator were a magnetron voltage of 4 kV, a target voltage of 110 kV, and a mass flow of 2.10. The phantoms were then irradiated for 10 minutes. The choice of 10 minutes was made due to work from prior students that suggested it was the ideal balance of time for thorough target element activation and a reasonable dose to the sample. Immediately following the irradiation, the sample was left to decay for 5 minutes. This allowed enough time for the sample to be removed and set up for detection.

2.2.3.3 Experimental HPGe Measurement Procedure

For measurement with the HPGe detector, the bone phantoms were placed directly against the face of the detector as shown in Figure 2.7. Placing the phantom as close as possible to the detector increases the geometry factor and thus enhances the overall detection efficiency. Once in place, lead bricks were placed to completely seal off the detector and the sample from the outside world to keep background low. A spectrum was then collected for 1 hour and recorded in the Maestro software. A 1-hour measurement time was chosen because a long counting time ensures that more counts will be observed. Larger counts result in better counting statistics and less uncertainty. A time period longer than 1 hour was not chosen because when we move to doing human hand measurements, we do not want the participant to have to sit in front of the detector for too long.

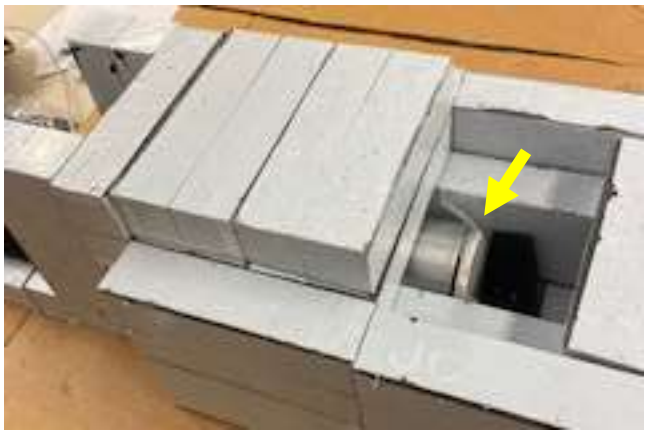

Figure 2.7. Bone Phantom Placement in HPGe Measurement System

2.2.3.4 Spectrum Fitting for Gamma Ray Peak Analysis

The result of the experiment is a gamma ray spectrum from the Maestro software. This spectrum gives the number of counts detected at each energy ranging from 0 to around 4000 keV. To extract the relevant count information from the peak of interest, which is the Mn peak at 846.7 keV, the data in that region must be analyzed with peak fitting. Peak fitting is the use of a mathematical equation to model the shape of the data. To fit the peaks, a peak fitting script was created using MATLAB.

The most important component of developing the script was choosing the correct equation to model the Mn peak. At its simplest, a gamma ray photo peak has the shape of a Gaussian distribution and can be fit with a simple Gaussian equation. However, it was found that our peak was more complex and needed other modifications to the equation. The low energy left side of the peak was showing a "tail" that deviated from the typical Gaussian fit. Also, it was found that there was a nearby Magnesium (Mg) peak at 843 keV that was overlapping with the Mn peak. Because of this, both peaks needed to be fit by the equation and then subtracted from each other. Lastly, the background counts needed to be modeled and subtracted as well.

In order to determine the best fitting equation to account for all parameters mentioned, the work of Jin et. al was referred to. This work gave examples of different fitting equations specifically for gamma ray response functions of germanium detectors[18]. Jin recommends fitting the full energy peak with a simple Gaussian equation shown in Equation 8.

$$f(x) = a * \exp\left[-0.5\left(\frac{(x-b)}{c}\right)^2\right] \quad (8)$$

In Equation 8, a is the amplitude of the peak, b is the value of the centroid of the peak, and c is the width of the Gaussian peak. In order to account for low energy tailing of the full energy peak, which is the result of incomplete charge collection, Jin uses a Gaussian function convolved with an exponential function which is given by Equation 9.

$$f(x) = e * \exp\left(\frac{(x-b)}{c}\right)^2 * erfc\left(\frac{(x-b)}{c}\right) \quad (9)$$

Parameters b and c are the same in Equation 9 as in Equation 8. e is the amplitude of the tail and erfc is the complementary error function. When added to one another, Equations 9 and 8 model the Mn peak. The Mg peak does not exhibit the low energy tailing and can thus be modeled

using a pure Gaussian equation such as that shown in Equation 8 but with its own unique values for a and b.

To model the background counts, two elements were used. The first was simply a constant function. This assumes that the background is a constant value across all channels. A "flat continuum" was used in addition to the constant function to better model the background. The flat continuum is the combination of a constant function combined with a Gaussian and is given by Equation 10.

$$f(x) = h * erfc\left(\frac{(x-b)}{c}\right) \tag{10}$$

In Equation 10, b and c are the same as for Equations 8 and 9. Combining all of these elements gives the final fitting equation. This equation is given by Equation 11.

$$f(x) = a * \exp\left[-0.5\left(\frac{(x-b)}{c}\right)^2\right] + e * \exp\left(\frac{(x-b)}{c}\right)^2 * erfc\left(\frac{(x-b)}{c}\right) + f * \exp\left[-0.5\left(\frac{(x-g)}{c}\right)^2\right] + d + h * erfc\left(\frac{(x-b)}{c}\right) \tag{11}$$

The summation of Equation 11 at all x values in the chosen range around the Mn peak gives the gross counts attributed to the Mn peak, Mg peak, and the background combined. To determine the net counts from the Mn peak alone, the gross counts are subtracted by the summation of the following Equation 12 which gives the counts from the Mg peak and the background alone.

$$g(x) = f * exp\left[-0.5\left(\frac{(x-g)}{c}\right)^2\right] + d + h * erfc\left(\frac{(x-b)}{c}\right) \tag{12}$$

2.2.3.5 Estimation of Neutron Yield Using Bone Phantom Experimental Results

The first of three methods used in this work to estimate the neutron yield of the D-D 109M neutron generator was comparing the Mn neutron activation results from the bone phantom experiments with the MCNP simulated Mn bone phantom neutron activation. As discussed in section 2.2.1.3, the combination of the F4 neutron flux tally and FM4 multiplier can be used in MCNP to simulate the number of target atoms that will be activated per source neutron. This result can be used along with Equation 4 to calculate the estimated counts that will be measured with the HPGe detector following the activation of the sample. One of the parameters in Equation 4 that is

needed to calculate the simulated counts, is the neutron flux of the system. This is the unknown flux, or neutron yield, that is to be solved for. By performing the experimental irradiation and measurement of the bone phantoms as described in sections 2.2.3.2 and 2.2.3.3, the experimental counts will be measured. These experimental results can be used in conjunction with the simulated results to solve for the neutron yield. Since the counts will be known due to experiment, the only unknown in Equation 4 is neutron yield. The equation can then be rearranged to solve for neutron yield as shown in Equation 13.

$$Neutron\ Yield = \frac{Experimental\ Counts}{R*S*C*D*\epsilon*\theta} \tag{13}$$

In Equation 13, R is the output of the MCNP Mn bone phantom activation simulation in units of activated atoms / (source n / sec). The parameters S, C, and D were calculated using the same irradiation, decay, and measurement times as used in the experiments which were 10 minutes, 5 minutes, and 1 hour respectively. An estimation for neutron yield was calculated based on simulated and experimental results from all ten bone phantoms to observe the reproducibility of the estimate.

2.2.4 Estimation of Neutron Yield Using Activation Foils

One method for detecting neutrons and determining the yield of a neutron source is the use of activation foils. This is the second method used in this work to estimate the neutron yield. Activation foils contain elements that will become radioactive through the neutron capture reaction discussed in section 1.3. As the radioactive atoms decay, they emit gamma rays of a particular energy that can be measured and used to determine the original strength of the neutron source. For this work, gold foils were chosen mainly because they were readily available in our lab. The neutron activation and subsequent decay of the gold foils is shown in Equation 14.

$$^{197}_{79}Au + n \rightarrow {}^{198}_{79}Au^{*} \rightarrow {}^{198}_{80}Hg + \beta^{-} + \gamma\ [411.7\ keV] \tag{14}$$

In this reaction, the unstable Au-198, with a half-life of 2.6797 days, is created during the neutron activation process. It decays via beta decay to the stable Hg-198 and emits a gamma ray of 411.7 keV energy with a branching ratio of 99.9%[11]. To estimate the neutron yield of this neutron generator, the activation of the gold foil will be performed experimentally with the system

as well as simulated in MCNP. The experiment will give results of counts detected and the MCNP simulation will give results of counts detected per source neutron per second. The experimental result can then be divided by the simulated result to solve for the unknown neutrons per second which is the yield.

2.2.4.1 Simulation of Gold Foil Activation with MCNP

To simulate the activation of a gold foil with the neutron generator system, the MCNP input file described in 2.2.1.3 was used. The bone phantom in the irradiation cave was replaced with a gold foil placed flush with the wall proximal to the neutron source. The modeled foil was circular and had a diameter of 1.3 cm and a thickness of 50.8 micrometers. The total mass of gold in this foil was calculated to be 0.126 grams. The multiplier for the activation tally was calculated using Equation 3. To determine the number of counts expected when the irradiated foil is measured with the HPGe, Equation 4 must be used.

2.2.4.2 Estimating the Detection Efficiency for the N-Type HPGe Detector

A critical parameter used in Equation 4 to determine the simulated counts measured by the HPGe detector is the detection efficiency for the specific gamma ray energy being measured. Detection efficiency represents the fraction of the total number of gamma rays detected to the number of total gamma rays emitted from a source. The detection efficiency varies with gamma energy. The detection efficiency at the energy of 411.7 keV, was unknown for this HPGe detector and was needed to calculate an accurate simulated count number. In order to estimate the detection efficiency, an MCNP simulation of the detector was created.

Starting with an existing input file of an HPGe detector from former student Colby Newman, an input file for this N-Type HPGe detector was created. The geometry of the file was adjusted to match the dimensions specified in the manual from ORTEC. The custom lead brick shielding assembly was also modeled into the file. A representation of the geometry in Visual Editor is given in Figure 2.8. The input file itself is included in Appendix A.

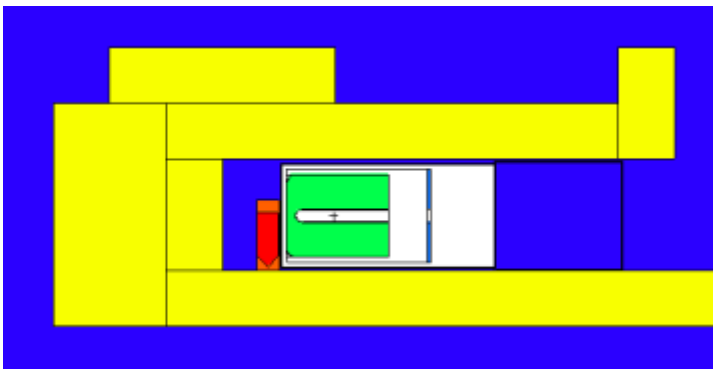

Figure 2.8. Visual Editor Rendering of HPGe MCNP Simulation Geometry

The source that was modeled was a multi-nuclide vial source from Eckert & Ziegler Isotope Products. This source is a mix of nine different radionuclides in a 5.17753 gram, 2M HCl solution. On the date of calibration, March 1, 2019, the total source strength was 5.137 micro-Curie. The data sheet provided when the source was purchased included the name of the nuclides, energy of the gammas, half-lives, branching ratio of the gammas, concentrations of activity, and the gammas per second per gram on the date of calibration. This information is provided in Table 2.1 with the values for activity and gammas per second decay corrected to the date, November 11, 2021.

Table 2.1. Multi-Nuclide Vial Source Data

Nuclide	Energy [keV]	Half-life [days]	Branch Ratio	Current Activity [Bq]	Gammas per second	MCNP Input	Fractional Amount
Cd-109	88	462.6	0.036	12206.36	443.10	1.23E-02	1.93E-02
Co-57	122	271.8	0.86	168.95	144.62	4.01E-03	6.29E-03
Te-123m	159	119.7	0.84	9.99	8.39	2.33E-04	3.65E-04
Cr-51**	320	27.7	0.099	0.00	0.00	3.52E-12	5.52E-12
Sn-113	392	115.1	0.65	26.24	17.03	4.72E-04	7.40E-04
Sr-85**	514	64.8	0.98	0.33	0.32	8.97E-06	1.41E-05
Cs-137	662	11012.1	0.85	8376.77	7128.63	1.98E-01	3.10E-01
Y-88	898	106.6	0.94	34.05	32.01	8.88E-04	1.39E-03
Co-60	1173	1924.3	0.999	7599.99	7598.48	2.11E-01	3.30E-01
Co-60	1333	1924.3	0.999	7599.99	7598.48	2.11E-01	3.30E-01
Y-88	1836	106.7	0.99	34.05	33.85	9.39E-04	1.47E-03

The column in Table 2.1 labeled MCNP Input is a value calculated in order to define the source in MCNP. To define a source in MCNP, the energy of each particle emitted from the source along with the probability of each particle to be emitted during a decay event must be defined. To determine this value, the gammas per second emitted by the specific energy gamma is divided by the total activity of the source. The geometry of the source was modeled as being homogenously distributed throughout the volume of liquid in the vial. The nuclides marked with the ** were not included in the simulation since the majority of the activity had decayed away.

To simulate the detection response of the germanium crystal to the various energy photons, an F8 pulse height tally is used. The output of this tally is the pulses (or counts) expected in each energy bin per source particle. Since detection efficiency is the number of photons detected compared to the number of photons emitted, a simulated detection efficiency can be calculated using the tally output at each energy and the fractional amount of that specific gamma ray. The Fractional Amount column of Table 2.1 is calculated by dividing the gammas per second for each specific nuclide by the sum of all gammas emitted per second. Thus simulated efficiency is calculated using Equation 15.

$$Simulated\ Eff. = \frac{Output\ of\ F8\ tally}{Fractional\ Amount} = \frac{\left[\frac{pulses}{total\ source\ photons}\right]}{\left[\frac{specifc\ energy\ photons}{total\ source\ photon}\right]} = \left[\frac{pulses}{specific\ energy\ photon}\right] \quad (15)$$

2.2.4.3 Validating Simulated Efficiency Experimental Efficiency

In order to validate the accuracy of the simulated detection efficiencies calculated with MCNP, an experiment matching the simulation was conducted. The real multi-nuclide vial source was placed flush against the HPGe detector and a 1-hour measurement was collected. This experiment was conducted on November 11, 2021 and thus the activity should be the same as the activity simulated in the MCNP file. A MATLAB peak fitting script similar to that discussed in section 2.2.3.3 was used on each peak individually to determine the counts measured from each. There were no nearby peaks to the peaks of interest so each peak could be fit as is without subtracting out neighboring peaks. To calculate the experimental detection efficiency, Equation 16 was used.

$$Experimental\ Eff. = \frac{counts\ measured}{A*BR*time} \quad (16)$$

In Equation 16, A is activity in Bq, BR is the branching ratio of the specific gamma ray, and time is the length of measurement in seconds. Multiplied together, the denominator gives the actual number of gammas emitted from the source during the counting period.

To better match the simulated efficiency to the experimental efficiencies, different iterations of the HPGe MCNP input file were created. Each iteration had a different thickness of dead layer on the Ge crystal. The dead layer is a region on the edges of the crystal that is insensitive to gamma rays. Files with the original dead layer thickness of 0.7 mm stated in the detector manual, plus 1 mm, plus 2 mm, plus 2.5 mm, and plus 3 mm of dead layer thickness were simulated.

2.3 Results

2.3.1 MCNP Simulation Mn Bone Phantom Activation Results

The MCNP simulation of the neutron generator irradiation assembly was run for each of the 10 Mn bone phantoms. The output of the Fm4 activation tally for each simulation is shown in Table 2.2. Using the Fm4 tally outputs and Equation 4, the simulated counts were determined. The values of the parameters in Equations 4, 5, 6, and 7 that were used to calculate the simulated counts are given in Table 2.3. An important parameter to note is the detection efficiency for the 846.7 keV gamma. For this work we used an estimated detection efficiency of 0.048 or 4.8%. Also, important to note is the choice of neutron yield. As mentioned, the exact yield of the generator is not known with great certainty. The value used here is 3E+09 which is the current estimation being used by our group based on numbers from Adelphi.

Table 2.2. MCNP Mn Bone Phantom Simulation Results

Mn Concentration [ppm]	Mn Activation Tally Output [activated atoms/source n]	Mn Counts
0	N/A	0
0.5	1.82813E-09	35.566385
1	3.65733E-09	71.153587
2	7.31611E-09	142.33538
5	1.82855E-08	355.74556
10	3.65591E-08	711.25961
15	5.48552E-08	1067.2114
20	7.31380E-08	1422.9044
30	1.09665E-07	2133.5395
40	1.46161E-07	2843.5715

Table 2.3. Parameter Values Used for Simulated Mn Count Calculations

Parameter	Value
Irradiation time	600 s
Decay time	300 s
Measurement time	3600 s
S Factor	0.043822475
D Factor	0.977843303
C Factor	3156.642939
Neutron Yield	3E+09 n/s
Detection Efficiency	0.048
Branching Ratio	0.9988

Using the simulated counts in Table 2.2, a simulated calibration curve was created. It is shown in Figure 2.9.

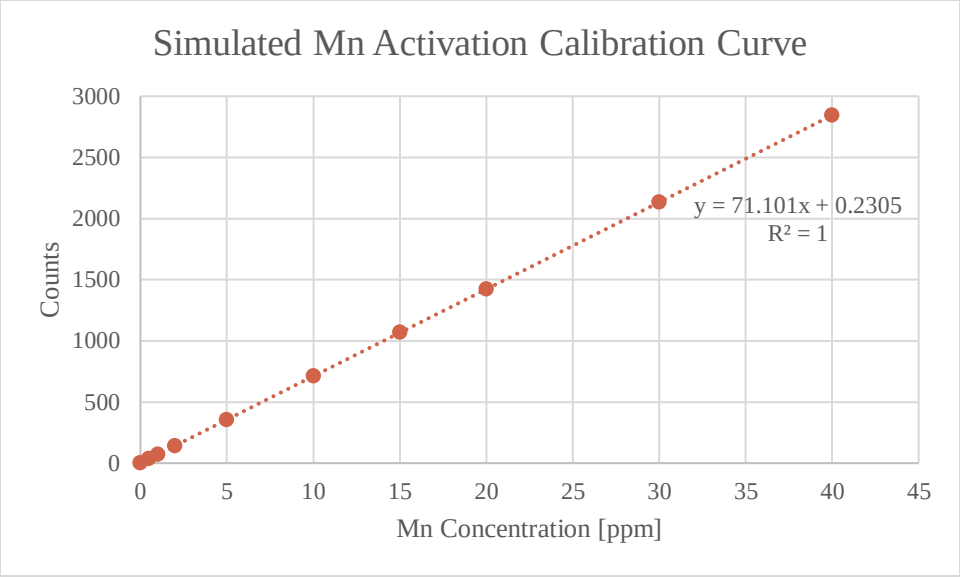

Figure 2.9. Simulated Mn Activation Calibration Curve

The calibration curve shows the relationship between Mn concentration in the sample and the counts detected by the HPGe system. This allows for the Mn concentration of an unknown sample to be determined based on the number of counts measured. It can be seen in Figure 2.9 that the relationship between Mn concentration and counts is perfectly linear with an R^2 value of 1. This is what is expected; as you increase the amount of Mn in the sample, you should see a linear increase in the number of counts detected. The slope of the linear trend line is 71.101 which means that there will be 71.101 counts detected by the HPGe system for every 1 ppm of Mn in the sample.

It is important to note that this calibration curve is only valid for experiments that have the same irradiation and measurement times; in this case 10 minutes of irradiation, 5 minutes of decay, and 1 hour of counting. A different combination of irradiation and measurement times would lead to a different number of counts per Mn concentration and would require its own unique calibration curve.

2.3.2 Experimental Mn Bone Phantom Activation Results

2.3.2.1 Experimental Counts from Mn Bone Phantoms

The set of Mn bone phantoms were individually irradiated and measured using the protocol of 10 minutes of irradiation, 5 minutes of decay, and 1 hour of counting. The result of each experiment was a gamma ray spectrum collected with the Maestro software. An example of a collected gamma spectrum is given by Figure 2.10.

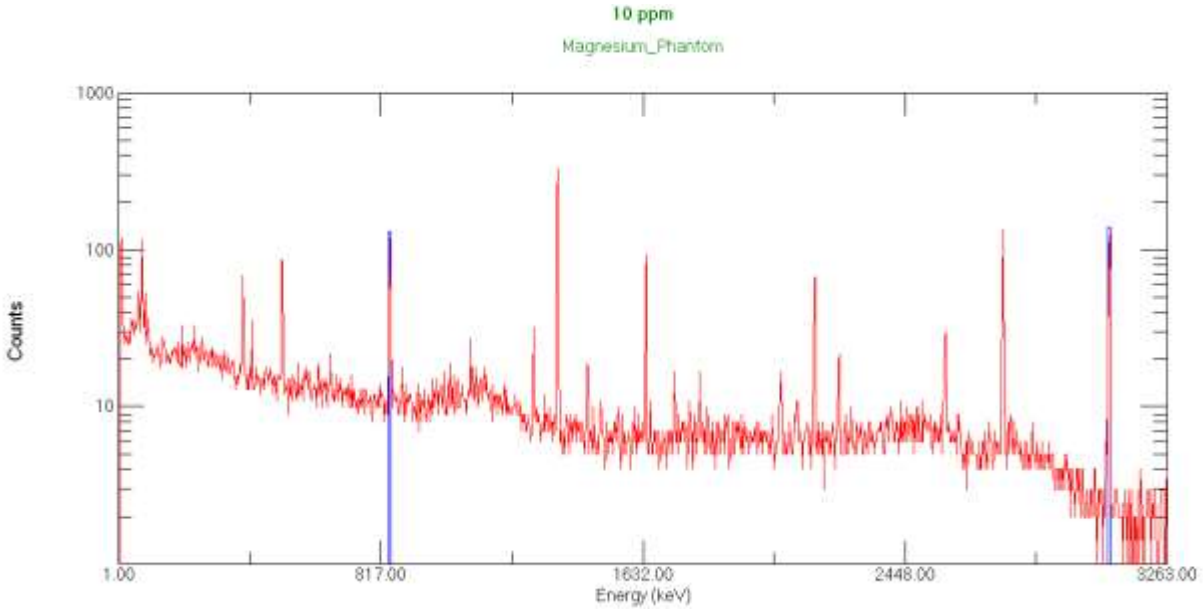

Figure 2.10. Gamma Spectrum of the 10 ppm Mn Bone Phantom

To determine the number of 846.7 keV photons emitted from Mn-56 decay, a MATLAB peak fitting script employing Equation 12 was used. An example of the peak fitting for the 5 ppm Mn phantom is given in Figure 2.11. The larger peak on the right is the 846.7 keV Mn-56 peak and the smaller peak on the left is the 843 keV Mg peak.

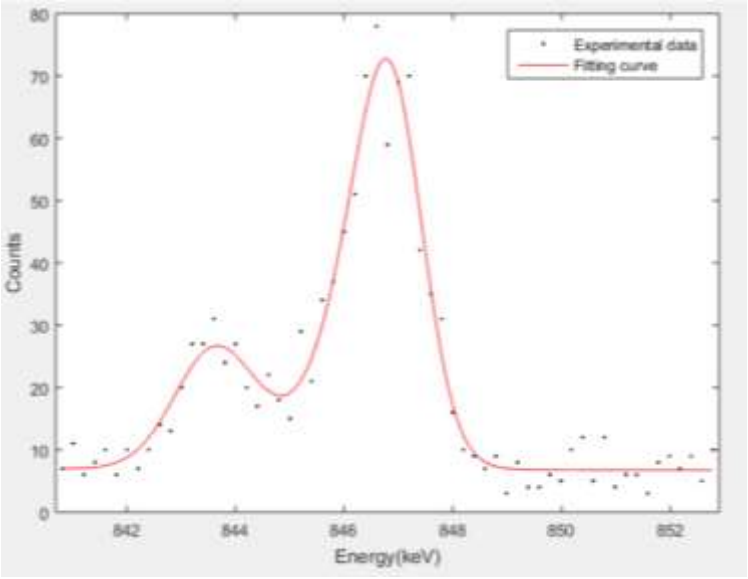

Figure 2.11. MATLAB Fitting of the Mg and Mm Photopeaks of the 5 ppm Mn Bone Phantom

Using this fitting script, the values of Gross, Net Mn, Net Mg, and Background counts were determined for each phantom. These values are presented in Table 2.4.

Table 2.4. Experimental Results of Mn Bone Phantom Irradiation and Measurement

Phantom	**Net Mn Counts**	**Mn Uncertainty**	**Net Mg Counts**	**Gross Counts**	**Background**
0	335.74	+/- 24.19	157.91	948	454.35
0.5	352.52	+/- 24.18	185.07	890	352.41
1	345.59	+/- 20.88	163.7	930	420.71
2	394.99	+/- 26.79	151.76	973.97	427.22
5	619.26	+/- 30.08	170.91	1208	417.83
10	906.62	+/- 34.91	127.51	1426	391.87
15	1075.2	+/- 36.49	150.09	1639	413.71
20	1416.8	+/- 37.56	148.83	1972	406.37
30	1880.3	+/- 38.10	174.53	2495	440.17
40	2324.5	+/- 43.72	230.13	3044	489.37

In all phantoms, there should be the same amount of Mg thus the net Mg counts should be roughly constant for each phantom. Also, since the measurement conditions were the same for all phantoms, the background counts should also be roughly constant for all phantoms. As a metric to determine the constancy of the net Mg counts and background counts for the phantoms, the mean and standard deviation were calculated for these two parameters. Then all values were checked to see if they lied within +/-3 sigma of the mean. This data is presented in Table 2.5

Table 2.5. Statistics of Experimental Mn Bone Phantom Measurements

	Mg Counts	Background Counts
Average Counts	166.044	421.401
Standard Deviation [σ]	27.640	36.547
+/- 3σ Confidence Interval	83.121 - 248.966	311.757 - 531.044

It was found that the net Mg and background counts for all phantoms fell within the 3σ confidence interval which is an indicator that the level of neutron activation and measurement was the same for all phantoms. Because of this, it can be assumed that the changes in the net Mn counts for each phantom were due to different concentrations of Mn and no other factors.

When looking at the net Mn counts in Table 2.4, some unexpected results can be seen from the 0 ppm phantom. The net Mn counts from the 0 ppm phantom are 335 counts. The 0 ppm phantom should not have any Mn in it and should therefore show 0 counts from Mn. The fact that a significant number of counts were seen for the 0 ppm phantom indicates that there was Mn contamination in the phantoms. This could have occurred if there were errors made during the creation of the phantoms, whether by human error or if some of the compounds used were contaminated with Mn. If the level of Mn contamination is the same throughout all of the phantoms, then the contamination can simply be subtracted out. This will be explored further in the next section.

2.3.2.2 Experimental Mn Bone Phantom Calibration Curve

Using the data in Table 2.4, an experimental calibration curve was generated for the bone phantoms. It is plotted along with the simulated bone phantom calibration curve from Figure 2.10, in Figure 2.12.

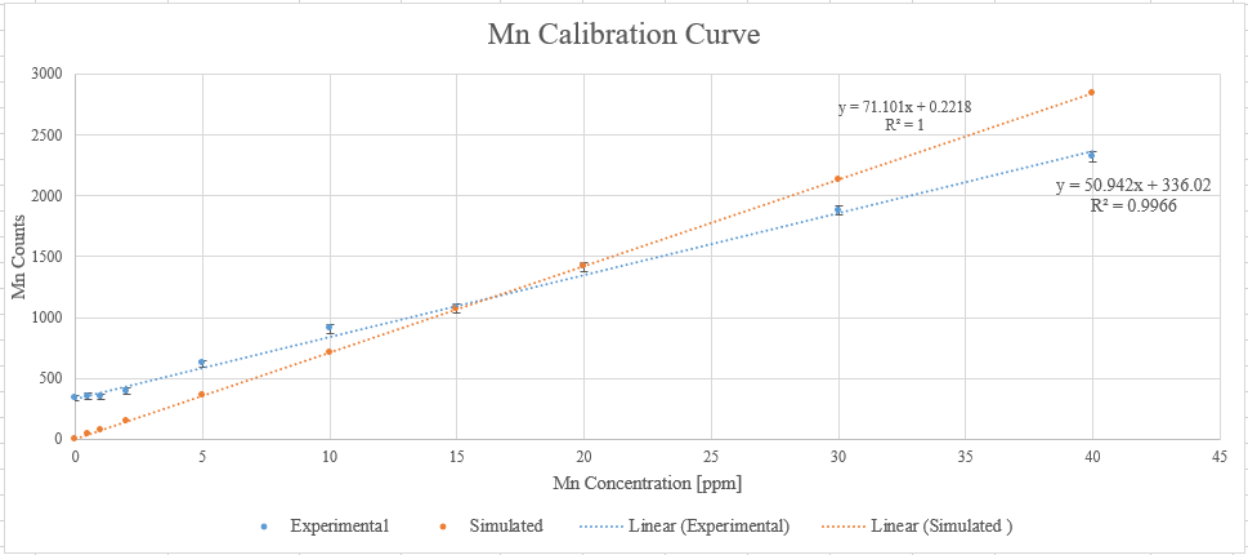

Figure 2.12. Mn Bone Phantom Experimental Calibration Curve

It can be seen that the experimental calibration curve differs significantly from the simulated calibration curve. The first major difference is that the slope of the experimental curve is not as steep as the slope of the simulated curve. This means that the experiment showed there are fewer counts per ppm concentration of Mn than originally estimated by the simulation. The steeper slope of the simulated curve likely indicates that too large of an estimate was used for the neutron yield when calculating the simulated counts. The experimental slope will be used instead of the simulated slope since the experiment more accurately represents the true performance of our system. The value for the experimental slope, 50.942, suggests that for every 1 ppm of Mn in a sample, 50.942 counts will be measured.

The other major difference between the experimental curve and the simulated curve is the y-intercept. The y-intercept of the experimental curve is at 336.02 while it is at 0 for the simulated curve. This larger y-intercept in the experimental curve is due to Mn contamination in the phantoms as mentioned at the end of section 2.3.2.1. This point on the experimental curve indicates that the 0 ppm phantom, which should have no Mn, had a level of Mn that produced 336.02 counts.

Since the entire experimental curve has a very strong linear relationship, with an R^2 of 0.9966, it signifies that the level of Mn contamination is constant in all phantoms. If this was not the case, and the contamination was in random amounts, the data points would be scattered and not linearly increasing. Because of this constant contamination, the counts found in the 0 ppm phantom can be subtracted from all of the other phantom counts. This will create a calibration curve with the same slope as the experimental curve but will be shifted down to have a y-intercept of 0. This can be done by subtracting 336.02 counts from each of the measured phantom counts to remove the counts attributed to contamination. Therefore, the final experimental calibration curve is given in Figure 2.13 with the equation given by Equation 17.

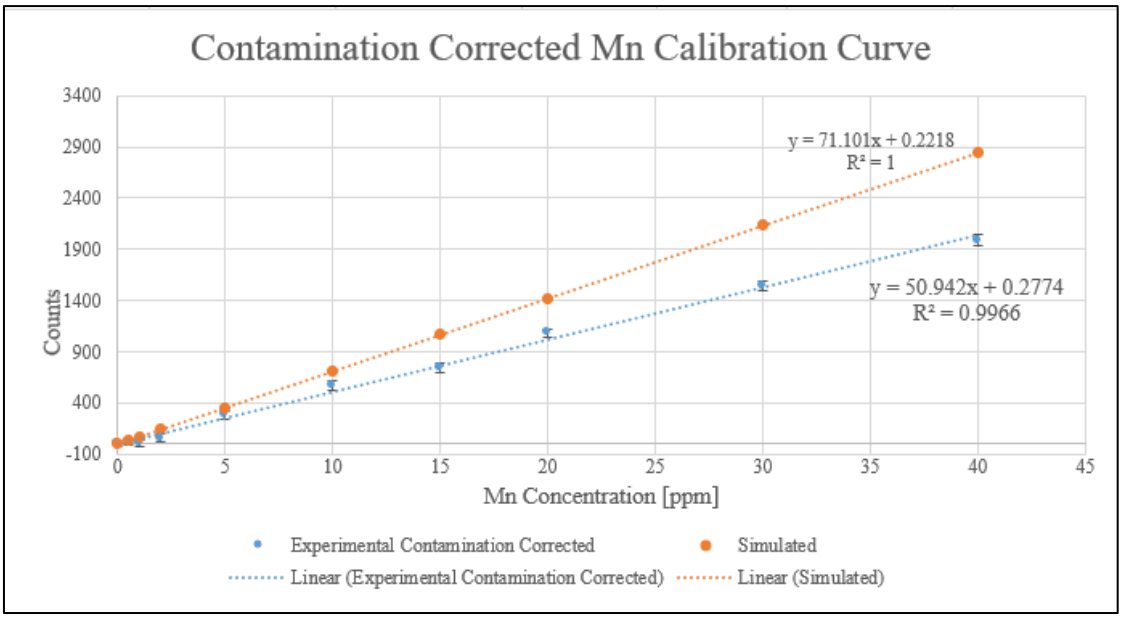

Figure 2.13. Contamination Corrected Mn Bone Phantom Calibration Curve

$$Y = 50.942 * X + 0.2774 \quad (17)$$

2.3.2.3 Estimation of Experimental Mn Detection Limit

The detection limit refers to the lowest concentration of Mn that is above zero and can be determined within a 97% confidence interval. This means that one can be 97% sure the measured Mn signal is accurate. In applications where measured concentrations are likely low, it is critical to minimize the detection limit to maximize the sensitivity of the measurement system. In this work, detection limit was calculated using Equation 18.

$$\text{D. L.} = \frac{2*\sqrt{\text{BKG}}}{C} \quad (18)$$

In Equation 18, D.L. is the detection limit in units of ppm, BKG is the background counts for the 0 ppm phantom within an interval of 4σ, and C is the slope of the calibration curve. The background was found to be 126.8 counts. The slope of the calibration curve, C, gives the counts expected per ppm of Mn in the sample. The slope of the calibration curve was 50.942 counts/ppm Mn as seen in Equation 6. Using these values and Equation 18, the experimental estimate of detection limit was 0.4421 ppm.

It is important to note that this detection limit estimate is only valid for experiments following the same condition of 10 minutes of irradiation, 5 minutes of decay, and 1 hour of counting. Other experimental conditions will lead to a different detection limit. This experimental Mn detection limit can be compared to a previously determined Mn detection limit for our lab's older DD 109 neutron generator that was determined by former student Yinzi Liu. Liu found that the Mn detection limit for the experimental conditions of 10 minutes of irradiation, 10 minutes of decay, and 1 hour of counting (only difference from this work is an extra 5 minutes of decay) was 0.428 ppm[19].

2.3.2.4 Neutron Yield Estimation Results Using Bone Phantom Data

The first step to use the bone phantom experimental and simulation data to estimate the neutron yield, was to correct the measured experimental bone phantom counts for contamination. As seen previously in Table 2.4 and Figure 2.12, there was a constant level of Mn contamination in all ten bone phantoms. As described in section 2.3.2.2, the amount of contamination in each phantom was 336 excess counts. To correct for this, 336 counts were simply subtracted from each of the experimental counts in Table 2.4. These corrected counts are those used to estimate the yield because they better represent the counts that would be seen if the phantoms actually contained the concentrations they were supposed to. The MCNP simulation results used for the estimation calculation were presented in Table 2.2. These values from experiment and simulation were used with Equation 13 to calculate the neutron yield estimate from each phantom. These results are given in Table 2.6.

Table 2.6. Neutron Yield Estimates from Mn Bone Phantom Activation Data

Phantom	MCNP Simulation Output [Activated Mn Atoms / Source n]	Experimental Counts	Neutron Yield [Neutrons/s]	Uncertainty [+/- neutrons/s]
0 ppm	N/A	0 +/- 34.2	N/A	N/A
0.5 ppm	1.82813E-09	16.78 +/- 34.2	1.42E+09	4.44850E+08
1 ppm	3.65733E-09	9.85 +/- 31.9	4.15E+08	2.07788E+08
2 ppm	7.31611E-09	59.25 +/- 36.1	1.25E+09	1.17315E+08
5 ppm	1.82855E-08	283.52 +/- 38.6	2.39E+09	5.01941E+07
10 ppm	3.65591E-08	570.88 +/- 42.5	2.41E+09	2.76260E+07
15 ppm	5.48552E-08	739.46 +/- 43.8	2.08E+09	1.89791E+07
20 ppm	7.31380E-08	1081.06 +/- 44.7	2.28E+09	1.45257E+07
30 ppm	1.09665E-07	1544.56 +/- 45.1	2.17E+09	9.78632E+06
40 ppm	1.46161E-07	1988.76 +/- 49.9	2.10E+09	8.12848E+06

The results of the neutron yield estimate are relatively consistent, especially for the phantoms with Mn concentration 5-40 ppm. The small amounts of fluctuation between these estimates are expected because the level of neutron production always varies slightly between runs. It makes sense that the estimates from the 0.5, 1, and 2 ppm data are lower than the others. The first reason is that the experimental Mn peaks collected for these phantoms were much smaller than the others since they contained less Mn. Smaller signals lead to larger relative measurement uncertainty because they are more difficult to discern from the background with certainty then larger peaks. Increased uncertainty in the experimental counts would lead to a less accurate estimate of the neutron yield. Also, these phantoms were irradiated first after the generator had not been operated in a while. It is known that there can be a bit of a warm-up period for this neutron generator during which the neutron yield is a little lower when it is first operated before leveling off to a more stable neutron flux.

Aside from being consistent with each other, the numerical values of the estimates are in line with what was expected. The vendor for this generator quotes that it can produce neutron yields of up to 3.0E+09. This would be at the highest end of its neutron production capability and the true operating value of the yield is expected to be lower than this peak value. Therefore, a yield estimate of around 2.2E+09 is highly probable. In order to establish the best estimate for the neutron yield, the average of the neutron yield estimated for the 5ppm-40ppm phantoms was

calculated. This average value is 2.24E+09 +/- 2.15E+07 neutrons per second. This is a 0.9% relative uncertainty.

2.3.3 HPGe Simulation and Neutron Yield Determination Results

2.3.3.1 HPGe Simulation of Detection Efficiency

An MCNP input file of the n-Type HPGe detector system was created matching the geometry given by the manual and using a multi-nuclide vial source as discussed in section 2.2.4.2 in order to simulate the detection efficiency at various photon energies. The results of the F8 pulse height tally from the simulation are given in Table 2.4. The unit of the tally output is pulses (or detection events) per source photon. By dividing the MCNP F8 tally output by the fractional amount of each photon, which was given previously in Table 2.1, the simulated detection efficiency for each energy photon was calculated and is given in Table 2.7 and Figure 2.13.

Table 2.7. MCNP HPGe Efficiency Simulation Results

Nuclide	Photon Energy [keV]	MCNP F8 Tally Output	Simulated Detection Efficiency
Cd-109	88	2.20E-03	1.14E-01
Co-57	122	7.97E-04	0.1268454
Te-123m	159	6.37E-05	0.174542342
Sn-113	392	7.40E-05	0.099994139
Cs-137	662	1.56E-02	0.050229718
Y-88	898	7.38E-05	0.053040692
Co-60	1173	1.18E-02	0.035706516
Co-60	1333	1.09E-02	0.032989578
Y-88	1836	3.95E-05	0.026822988

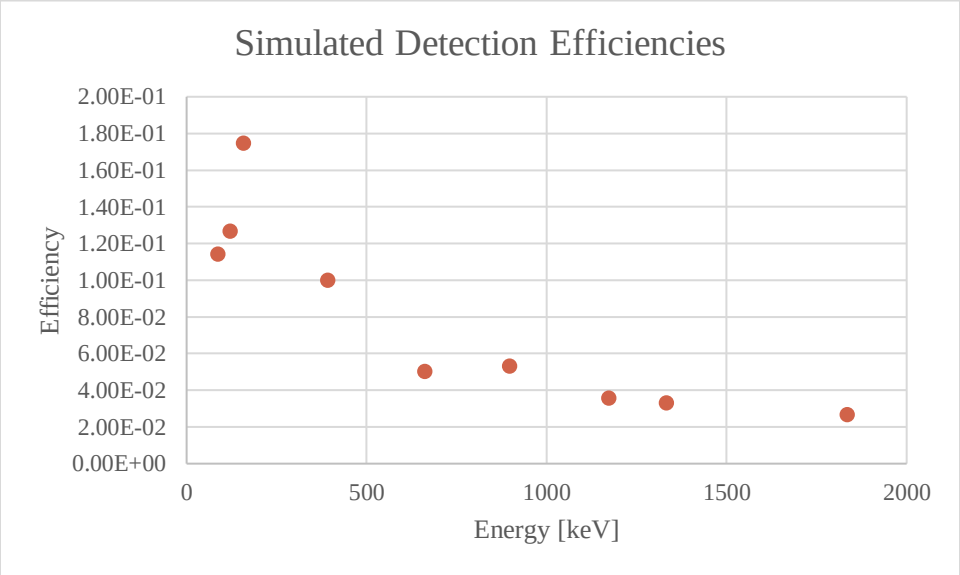

Figure 2.14. Simulated Detection Efficiencies of the N-Type HPGe Detector

Overall, the shape of the curve in Figure 2.14 is what is expected. The efficiency starts lower for the lowest energy photons and then reaches a peak efficiency before falling as energy increases. This occurs because very low energy photons have very little penetrating ability and often get absorbed before they can enter into the crystal and be detected. Then you hit a sweet spot in energy and therefore penetration capability where the photon has just enough energy to penetrate the crystal but not enough to cross through without interacting. Finally, as you continue to increase

energy and penetration ability, the photon will most likely pass through the crystal without interacting.

One deviation from the expected results is the efficiency for 662 keV. It is expected that the curve would take on a smooth exponential decay following the peak efficiency, but this point does not follow the smooth curve. It is lower than expected.

2.3.3.2 HPGe Experimental Detection Efficiency

The physical multi-nuclide source that had been used as the model for the MCNP detection efficiency simulation was experimentally measured with the HPGe system on November 11, 2021. The result of the measurement was a gamma ray spectrum that needed to be analyzed using the peak fitting MATLAB script. Each peak of interest was fit individually to determine the number of counts attributed to each unique photon energy. An example of the fitting for the 662 keV Cs-137 peak is given in Figure 2.15.

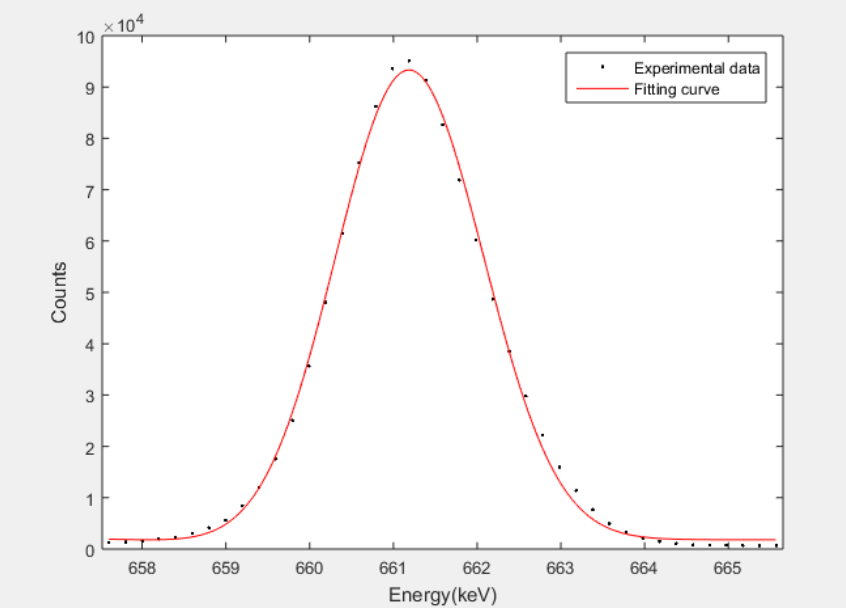

Figure 2.15. MATLAB Peak Fitting of Cs-137

To determine the experimental efficiency for each photon energy, the experimental counts measured were divided by true number of photons emitted during the measurement interval as

shown previously in Equation 15. The experimental detection efficiency for each photon energy is given in Table 2.8 and is plotted in Figure 2.16.

Table 2.8. Experimental Detection Efficiencies Found Using Multi-Nuclide Standard

Nuclide	Photon Energy [keV]	Experimental Detection Efficiency	Uncertainty
Cd-109	88	0.118	+/- 4.01E-04
Co-57	122	0.109	+/- 4.06E-04
Te-123m	159	0.085	+/- 2.72E-03
Sn-113	392	0.056	+/- 1.03E-03
Cs-137	662	0.040	+/- 5.76E-04
Y-88	898	0.033	+/- 7.65E-04
Co-60	1173	0.022	+/- 4.26E-04
Co-60	1333	0.020	+/- 4.63E-04
Y-88	1836	0.016	+/- 7.61E-04

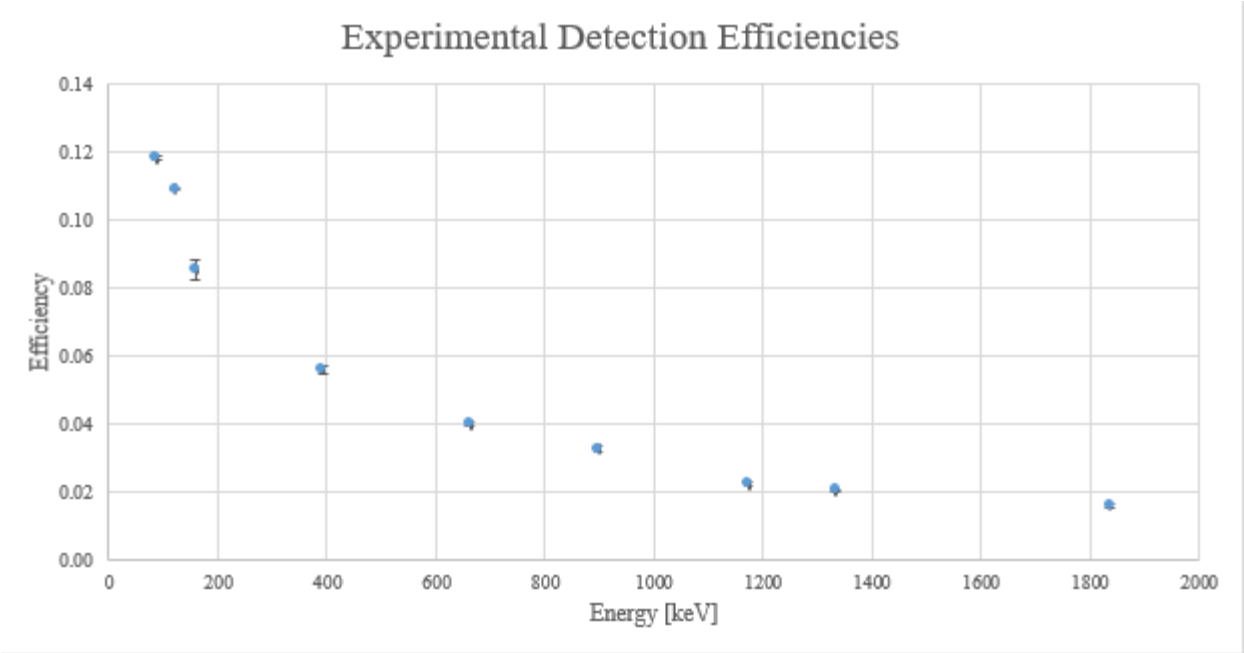

Figure 2.16. Experimental Energy Efficiency Curve of Multi-Nuclide Standard

The results of the experimental detection efficiencies were initially puzzling. The expected curve shape shown by the simulated efficiencies in Figure 2.14 was not seen in the experimental efficiencies in Figure 2.16. The experimental data shows a continuous decrease in efficiency with energy; no peak followed by a decrease as expected. To eliminate the possibility that this was due to human error, a second experimental measurement was made. These results gave the same curve shape. It was concluded that the lack of the efficiency peak at low energies was likely due to the fact that the activity of the lower energy photons was too low because the source was several years old. This introduces larger uncertainty in the count measurement. When count rates are low, the uncertainty of the measurement increases meaning that one cannot be as certain about where the true value lies. This large uncertainty may explain why the low energy efficiencies are not as expected.

To determine if this was the problem, a new multi-nuclide source with a high activity was purchased by the lab. Due to delayed shipping, the experimental measurement of the new source was not able to be performed in time for the completion of this work.

2.3.3.3 Altering MCNP Simulation of HPGe to Better Match Experimental Results

Although it was found in the previous section that the experimental detection efficiency data was not as expected for low energy photons, an attempt was still made to alter the MCNP simulation of the HPGe to better match the experimental efficiency; especially at higher energies. The parameter modified in the MCNP input file was the thickness of the dead layer of the Ge crystal. The original simulation used the dead layer thickness specified by the manufacturer but there can always be error in the manufacturing process which might mean that the thickness of the dead layer of our particular detector could be slightly different. An explanation of the various simulation trials is given in Table 2.9.

Table 2.9. Description of Various HPGe Simulation Iterations

Simulation #	Description
1	Original thickness, 0.7 mm
2	Plus 1 mm, Total 1.7 mm
3	Plus 2 mm, Total 2.7 mm
4	Plus 2.5 mm, Total 3.2 mm
5	Plus 3 mm, Total 3.7 mm

A plot containing the efficiencies from all of the simulation trials compared to the experimental efficiency is given in Figure 2.17.

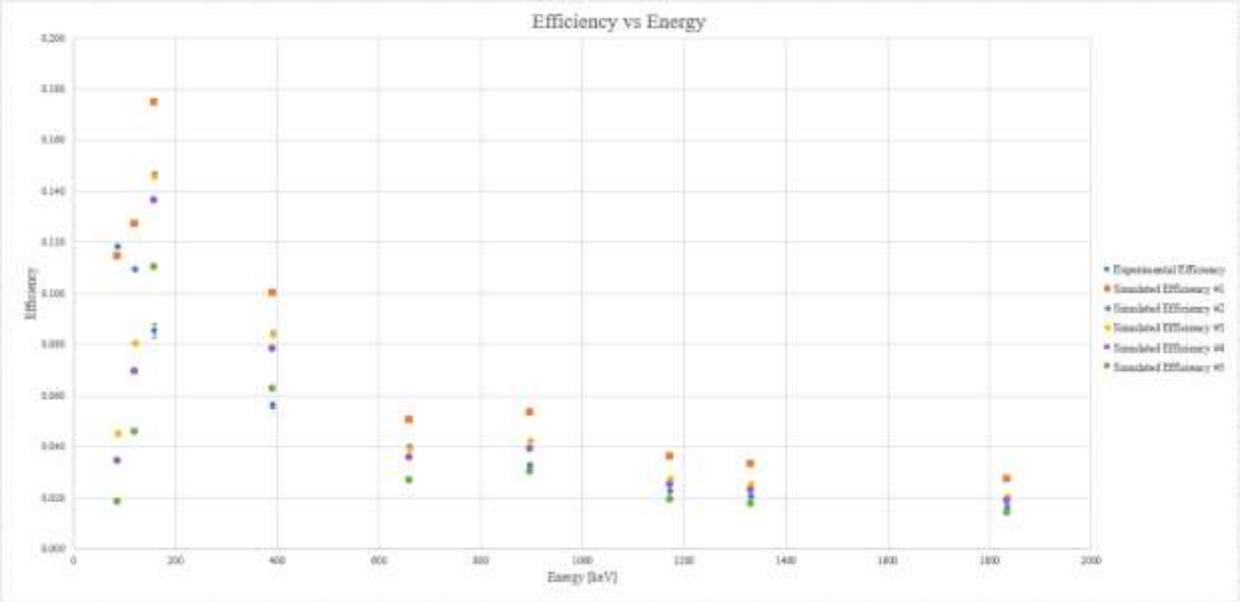

Figure 2.17. Simulated Detection Efficiencies from Various MCNP Simulation Iterations

From Figure 2.17, it is seen that for all 5 simulations, there is much closer agreement to the experiment at higher photon energies. At the lower photon energies there is a large spread in efficiencies between the 5 simulations. This makes sense because lower energy photons have a very low penetration ability which means that increasing the dead layer thickness even by a small amount will make a large difference in the number of photons that can reach the active volume of the detector and be detected. For higher energy photons with large penetration ability, the effect of small increases in dead layer thickness is not as significant.

It is difficult to extract meaningful information about which simulation best matches the experimental low energy efficiencies because of the experimental issues discussed in the previous section. If the true experimental efficiencies of the low energy photons are lower than the current estimate, there would be better agreement with the simulated results and one simulation could be chosen that best represents the efficiencies for all energies. Until new experimental data is collected with the new source, a good estimation of the detection efficiencies cannot be determined with enough certainty.

2.3.3.4 Neutron Yield Determination Using Gold Foil Activation

Due to the fact that an accurate estimate of the detection efficiency of the 411 keV Au gamma was not able to be determined through simulation as discussed in the previous section, the method of determining neutron yield through gold foil activation was not able to be used at this time. Based on the current simulation results, the efficiency for this gamma could be anywhere between 4-10%. This makes a very significant difference in the estimation of yield.

An experiment was conducted irradiating the gold foil for 10 minutes followed by 5 minutes of decay and 1 hour of counting. After using the MATLAB fitting script on the 411 keV photopeak, it was determined that there were 88,500 counts detected. An MCNP simulation was also run of the gold foil irradiation and measurement. The result of the Fm4 tally was 1.36E-5 Au atoms activated per source neutron. From here, the simulation and the experimental results were used along with two different simulated detection efficiencies to see how much the uncertainty in detection efficiency would affect the final yield calculation. Detection efficiencies of 4% and 10% were used since they represented the two extremes of the range of simulated efficiencies. The calculation method used was outlined in section 2.2.4. The results of the neutron yield calculation using these two efficiencies are given in Table 2.10.

Table 2.10. Neutron Yield Estimates Using Gold Foil Activation Method

Detection Efficiency Used	**Calculated Neutron Yield**
4%	1.66E9
10%	4.15E9

The percent difference between the two different calculated yields is 150%. This is an unacceptable level of uncertainty for the neutron yield which is a value that must be known with high certainty to perform accurate simulations and dose measurements for the system. To get a better estimation of yield, a second method based on dose was used and is discussed in Chapter 3.

2.4 Discussion

The first major points of discussion are the simulated and experimental calibration curves. The simulated curve showed more detected counts per ppm of Mn than the experimental curve did. This is likely explained by choosing too large of an estimated neutron yield to calculate the simulated counts. Multiplying all of the data points by a larger constant would shift the curve to a steeper slope as seen in the simulated curve. This suggests that the actual neutron yield is lower than the estimate of 3E+09 neutrons/s that was used. Also, there was found to be around 340 counts worth of Mn contamination in all bone phantoms. This was likely due to contaminated compounds being used to produce the phantoms. This constant contamination was subtracted out of all the measurements in order to determine a usable experimental calibration curve. Although it was accounted for, it would still be advantageous to create a set of new Mn bone phantoms without Mn contamination and measure them to confirm the accuracy of this calibration curve.

Using the experimental calibration curve, a Mn detection limit of 0.442 ppm was estimated for this system. This is a little worse than the Mn detection limit previously determined by Liu for our older generator system. This result is a bit unexpected since it is believed that the new generator used in this work has a higher neutron yield than the old generator used by Liu. We believed that a larger neutron yield would allow for more Mn activation and thus a lower detection limit. This suggests that there is a larger fast neutron flux in the irradiation cave but the same thermal flux in the cave as with this old system. More fast flux will not increase neutron activation, only increase dose. Therefore, more work should be done in the future with simulation to optimize the thermal neutron flux in the irradiation cave in order to improve the neutron activation. A good place to start would be more MCNP simulations of various moderator and reflector materials and geometries.

The neutron yield estimation method utilizing the Mn bone phantom simulation and experimental results allowed for a very good estimate of the neutron yield to be calculated. The average value of the neutron yield was determined to be 2.24E+09 +/- 2.15E+07 neutrons per

second. This value aligns very closely to what was expected based off the information provided by Adelphi Technologies at the time of purchase. Since this result was seen consistently between several of the phantoms and aligns with expected results, this is considered our best estimate for the neutron yield of the D-D 109M generator and will be used as the "true" value for the rest of this work. This value is also significantly higher than the neutron yield for the older D-D 109 generator system which is around 7E+08. This is a great confirmation, since the newer generator was purchased with the hopes of having a greater yield and thus the potential for better neutron activation ability than the old system.

The final area of discussion is the unexpected results with the HPGe detection efficiency experiment and simulation. As seen in Figure 2.17, the shape of the experimental efficiency versus energy curve did not match the shape of the simulated curve. The simulated curve, with the efficiency peaking at the beginning and then falling at all higher energies, is the shape that is expected from theory. The experimental efficiencies did not show any peaking at low energies; only a continual decrease with energy. This is likely due to the fact that the standard source used was several years old and some of the lower energy photon emitting isotopes had decayed away to low levels. Low count rates lead to larger uncertainties which could explain why the peaking behavior was not seen. To confirm this hypothesis, a newer standard source will be used in the future to create an experimental efficiency curve. Because the HPGe detection efficiency simulation could not be validated with sufficient certainty, an accurate estimate of the detection efficiency for gold was unable to be determined. Without this gold efficiency, the method of gold foil activation to determine the neutron yield was not able to be completed. Future work should be done to pursue this method once a better estimate of the gold efficiency is determined.

CHAPTER 3. DOSIMETRY

3.1 Introduction

This neutron activation analysis system will eventually be used to perform in-vivo bone measurements of the human hand. Because there will be living participants being irradiated, it is critical that the radiation dose that they will receive is accurately estimated and below the regulatory limit. As mentioned previously, the regulatory limit to an extremity for a radiation worker is 50 rem annually[15]. In order to be conservative and in line with the As Low As Reasonably Achievable (ALARA) philosophy of radiation protection, the dose limit imposed on this system is 10% of the annual limit, thus 5 rem. To accurately estimate the dose, a combination of TLD badges, MCNP simulation, and EPDs were used. This chapter details the methods used and the dose results found

3.2 Materials and Methods

3.2.1 TLD Dose Measurements

3.2.1.1 TLD Badges

One method of measuring dose is through the use of Thermoluminescent Dosimeters (TLDs). These are passive radiation detectors that store the dose information of an irradiation event. They must be manipulated afterwards to extract the dose information. The TLDs used in this work were Genesis Ultra TLD-BP TLDs from Mirion. This detector is sensitive to photons, betas, and neutrons. It has the ability to detect neutrons from thermal energies up to 6 MeV. This means that it will be able to detect the full spectrum of neutron energies seen in the irradiation cave of the neutron generator system. This detector is quoted to have a minimum reportable dose of 1 mrem.

In order to be read, these TLDs must be shipped back to Mirion where they have the proper calibration that allows for the light output from the TLD to be converted into a dose value. The dose results received back from Mirion will include photon dose and neutron dose.

3.2.1.2 TLD Irradiation Protocol

In order to get an estimate of the neutron and photon doses received by a sample in the irradiation cave of the neutron generator, four TLDs were irradiated. By using different placements of the four TLDs in the cave, three specific dose questions were explored. For the first irradiation, three TLDs were used and they were placed according to the geometry shown in the schematic in Figure 3.1.

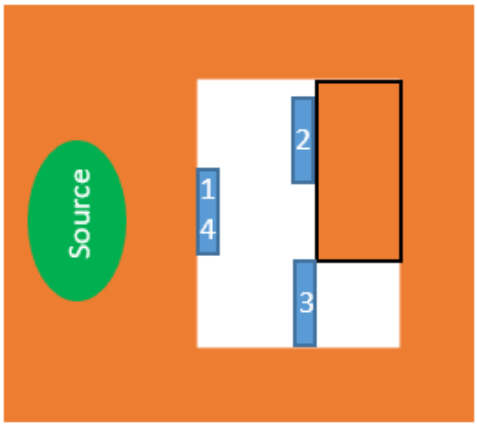

Figure 3.1. Schematic Diagram of TLD Placement in the Irradiation Cave

Figure 3.1 provides a top-down view of the irradiation cave. The three blue boxes represent the three TLDs that were irradiated. TLD #1 was placed flush with the left wall of the cave which is the wall proximal to the generator head. This TLD placement was chosen to most closely represent the dose received by a sample since samples are always placed flush with the left wall of the cave. The placement of TLDs #2 and #3 was chosen for two purposes; one to show if the dose fluctuates between different location in the cave and two, to show the effect of back scatter on the dose. To achieve the first purpose, TLD #2 was placed in the upper half of the cave while TLD #3 was placed in the bottom half of the cave. To achieve the second goal, TLD #2 was mounted on a block of polyethylene in order to observe if there was any dose enhancement due to backscatter. To observe the effects of no backing, TLD #3 was taped to the polyethylene block at the edge so that its entire backside was open to the air of the cave.

The fourth TLD, TLD #4, was irradiated on its own in the same placement as TLD #1. This was done in order to collect more data at the main dosimetric point of interest in order to observe

the reproducibility. It is important to know if the dose is consistent between generator runs. Both sets of the TLDs were irradiated for 10 minutes.

3.2.2 MCNP Simulated Dose Estimates

MCNP, which was discussed previously for its use of simulating neutron activation, can also be used to simulate the dose received from a specific source. There are several methods that can be used within MCNP6 to simulate dose. For this work, two different methods were used to simulate neutron dose received by a sample. Only one method was used to simulate photon dose since that is a more straight forward calculation. All three methods are discussed below.

3.2.2.1 MCNP Dose Simulation Using Built-In Dose Functions

The first method used for simulating the neutron dose received by a sample with this system was to use one of MCNP's built in dose conversion functions. With this method the user must first create an F4 flux tally in the cell of interest and then modify this flux tally with one of the built-in dose functions. These dose functions contain conversions to go from flux to effective dose. Each built in dose function has slightly different values and methods of converting from flux to dose. For this work, the built-in dose function based off conversion data from NCRP-38 1971 was used to simulate neutron dose. The tally input is given by the following:

```
F4:n 29
DF4 IU 2 IC 20
```

The first line of code creates the F4 neutron flux tally in cell number 29 which is the cell ID number of the bone phantom. The second line of code calls the dose function to modify the first tally. IC 20 indicates the specific built in dose function that is to be used and IU 2 specifies the unit of the modified tally output[13]. The unit chosen is sieverts/h/(source particle/s). Therefore, to calculate the equivalent dose received by the sample, Equation 19 must be used.

$$\text{Eq Dose} = \text{Tally Output} * \text{Irr. Time} * \text{Flux} = \frac{\text{Sv·s}}{hr \cdot source\ n} * hr * \frac{Source\ n}{s} * \frac{100\ rem}{Sv} = rem \quad (19)$$

This same method of built-in dose functions was also used to simulate the photon dose. The user creates an F4 flux tally of photons in the desired cell and then converts it to dose by calling the chosen built-in dose function. The tally input is shown below.

```
F4:p 29
DF4 IU 2 IC 10
```

Just as with the neutron dose method, an IU of 2 was used. IU of 2 specifies the units of output as sieverts/h/(source particle/s). For photon dose, an IC of 10 is used. This indicates that the dose function based off data from ICRP-21 1971 will be used. Equation 19 can be used to calculate the equivalent photon dose using the MCNP output.

3.2.2.2 MCNP Dose Simulation Using Custom Flux to Dose Conversion Factors

The other method used to simulate the neutron dose was entering in a custom point wise response function of flux to dose conversion factors to modify the neutron flux tally. This method also requires the user to start with an F4 neutron flux tally in the cell of interest but differs from the previous method in that the user inputs their own flux to dose conversion factors to modify the original tally. Since the conversion from flux to dose varies with the energy of the particle, the flux tally must be broken up into smaller energy bins with a unique flux to dose conversion factor for each bin. The flux to dose conversion factors used for this method come from the ICRP 74 Report. The tally input is given by the following:

```
F4:n 29
DE4  1.00E-09 1.00E-08 2.53E-08 1.00E-07 2.00E-07 5.00E-07 1.00E-06 2.00E-06
     5.00e-06 1.00E-05 2.00E-05 5.00E-05 1.00E-04 2.00E-04 5.00E-04 1.00E-03
     0.002 0.005 0.01 0.02 0.03 0.05 0.07 0.1 0.15 0.2 0.3 0.5 0.7 0.9 1 1.2 2 3
DF4  2.3760E-03 3.2400E-03 3.8160E-03 4.6440E-03 4.8600E-03 4.8960E-03
     4.7880e-03 4.6440E-03 4.3200E-03 4.0680E-03 3.8160E-03 3.5640E-03
     3.3840e-03 3.2040E-03 2.9880E-03 2.8440E-03 2.7720E-03 2.8800E-03
     3.7800e-03 5.9760E-03 8.5320E-03 1.4796E-02 2.1600E-02 3.1680E-02
     4.7520e-02 6.1200E-02 8.3880E-02 1.1592E-01 1.3500E-01 1.4400E-01
     1.4976e-01 1.5300E-01 1.5120E-01 1.4832E-01
```

Again, the first line of code creates the neutron flux tally in cell number 29 and the rest of the code converts the flux to dose. The DE lines break the flux tally into many smaller energy bins and the DF lines provide the specific flux to dose conversion factors for each corresponding energy bin. The final output from this tally has units of mrem/hr/(source n/s). In order to calculate the final equivalent dose received, Equation 20 is used.

$$\text{Eq Dose} = \text{Tally Output} * \text{Irradiation Time} * \text{Flux}$$
$$= \frac{\text{mrem} \cdot \text{s}}{hr \cdot source\ n} * hr * \frac{source\ n}{s} * \frac{10^{-3} rem}{mrem} = rem \tag{20}$$

3.2.3 Estimation of Neutron Yield Based on Dose

A second method for estimating the neutron yield of the D-D 109M Generator based on dose was also used. This method involved combining the results from the TLD measurements with the results of the MCNP dose simulations in order to back calculate for the neutron yield. From the TLD irradiation we have the equivalent dose received at that location for 10 minutes of irradiation. From the MCNP dose simulations, we have the effective dose per unit time and per source neutron/s at the same location as the TLDs. Using these two pieces of information, the neutron yield can be calculated by dividing the former by the latter as shown in Equation 21.

$$\text{Neutron Yield} = \frac{\text{TLD Dose}}{MCNP\ Simulated\ Dose\ Output * Irradiation\ Time} = \frac{Sv}{\frac{Sv \cdot s}{hr \cdot Source\ n} * hr} = \frac{Source\ n}{s} \quad (21)$$

3.2.4 EPD Dose Measurement

Another type of dose measurement device used in this work was an electronic personal dosimeter (EPD) from Fuji Electric Co. The model used was an NRF31 which is sensitive to both gamma and neutron radiation. One of the major advantages of an EPD is that it provides dose information in real time. The EPD can be placed in a radiation field and will display instantaneous dose readings. This EPD is capable of displaying live neutron and photon dose rates as well as integrated dose for the entire period that the EPD is powered on.

The issue with EPDs is that when it comes from the manufacturer, it is calibrated to a source at the manufacturer. In order to accurately measure the dose of the user's source, especially if the user's source is vastly different form the manufacture's source, the EPD must be calibrated to the user's source once purchased. In cases where the source strength and dose rates are known, it is easy for the user to adjust the calibration of the EPD using the Settings Software, NRZ, that comes with the device. In the case of our system, the source strength and the dose rates are unknown; that is what is trying to be determined by this work. Because of this, there was no way for the EPD to be calibrated to our source.

Since the EPD was not calibrated to our source, which would have required knowing the true dose produced and subsequent tuning of dose correct factors on the EPD software until the reading matched the true dose, the dose readings found using the device were only used as a reference. Since our neutron source is likely much different than the neutron source used to do the original calibration by the manufacturer, the neutron doses given by the device were expected to be inaccurate. Neutron dose calibration is more difficult in general since there are different radiation quality factors used to convert from energy deposition to dose based on the energy range of the neutrons. The gamma dose did appear to be accurate and consistent since gammas have an easier calibration from energy deposition to dose with a radiation quality factor is 1 for all gamma energies.

Even though the doses from the EPD are not accurate for our source, the EPD was still used as a useful tool during irradiation experiments as the readings are relatively accurate (i.e. all readings will differ from the real dose by a fixed factor). It is important to ensure that all samples

are receiving the same amount of radiation and therefore activation. This ensures that differences in measured results come from differences in the samples and not differences in the amount of irradiation. To help measure the constancy of activation between generator runs, the EPD was placed in the irradiation cave behind all of the bone phantom and cadaver bone samples during their irradiation. Even though the numerical value of the doses recorded with the EPD is not accurate to the true dose received, it is still indicative of the amount of radiation received. For example, the amount of radiation produced in one, ten-minute irradiation may result in an EPD neutron dose reading of 20 rem. Since it is not correctly calibrated, this does not mean there was actually 20 rem of dose received, but it is a valid metric of how much radiation was received. If the generator was run again for 10 minutes, and the EPD again showed a neutron dose of 20 rem, it can be concluded that there was an identical amount of radiation produced during that run. Because of this fact, the EPD was placed into the irradiation cave for all experimental irradiations to check for constancy.

3.3 Results

3.3.1 TLD Dose Results

The irradiated TLDs were mailed away to Mirion to be read. The TLD dose results from Mirion are presented in Table 3.1.

Table 3.1. TLD Dose Readings

TLD #	Total Deep Dose [rem]	Total Shallow Dose [rem]	Neutron Dose [rem]
1	16.265	15.460	17.023
2	16.709	16.066	14.733
3	17.212	16.550	18.080
4	14.211	13.664	14.857

According to the report from Mirion included with the results, the shallow dose is at a tissue depth of 0.007 cm, the deep dose is at a tissue depth of 1 cm, and the neutron dose is part of the reported deep and shallow doses. Therefore, the photon dose can be found by subtracting the neutron dose from the deep and shallow doses.

Overall, these results seem to be inaccurate. First, for TLDs #1, #3, and #4, the neutron dose is larger than both the deep and shallow doses. This does not make sense. According to the interpretation report, the neutron dose should be a part of the other two doses and therefore would need to be smaller than those doses. An attempt was made to contact Mirion for further explanation on this confusing result and the sales engineer was also unsure how to explain it. He was going to further investigate with some of the technical engineers but was unable to get us an explanation before the completion of this work.

Additionally, the neutron dose values seem to be much higher than expected. Past work by former lab members estimated that the neutron dose was on the order of 1 rem[19]. Also, looking at the results for each TLD in comparison to one another, the results expected were not seen. As described in section 3.2.1.1, TLDs #1 and #4 were irradiated in the same location. Thus, it is expected that these two badges would show similar dose results. This was not seen. Badge #1 had a neutron dose of 17.023 rem while badge #4 had a neutron dose of 14.857 rem. This is a significant difference and larger than would be expected from normal fluctuation in radiation yield. Also, badge #2 was placed in front of backing to see the backscatter enhancement while #3 was placed with no backing. It was expected to see a larger dose from badge #2 than badge #3 but the opposite was seen.

Unfortunately, due to all of these inconsistencies, the results from these TLD measurements are unreliable and will not be used as values for absolute dose as originally hoped. These results were still used to estimate a neutron yield along with the MCNP dose simulation in order to further assess their validity.

3.3.2 MCNP Simulation Results

3.3.2.1 MCNP Neutron and Photon Dose Simulation

The results from the various MCNP dose simulations for neutron and photon dose are presented in Table 3.2.

Table 3.2. MCNP Dose Simulation Outputs

Method	Result
Built-In Neutron Dose Function	2.01115E-10 Sv/hr/(source n / s)
User Entered Neutron Flux to Dose Conversion	2.37867E-05 mrem/hr/(source n / s)
Built-In Photon Dose Function	6.64936E-06 Sv/hr/(source n / s)

To transform these simulated results into estimates of equivalent dose, Equations 19 and 20 must be used. In order to use Equations 19 and 20, the yield of the neutron generator must be known. The yield used for these calculations was 2.24E+09 neutrons per second which was the best estimate for yield found in section 2.3.2.4. Also, an irradiation time of 10 minutes is used in Equations 19 and 20 since that is the irradiation time used for this work. Using the equations and best estimate for yield, the simulated doses were calculated and are presented in Table 3.3.

Table 3.3. MCNP Simulated Equivalent Doses

Method	Result
Built-In Neutron Dose Function	7.51 +/- 1.88 rem
User Entered Neutron Flux to Dose Conversion	8.88 +/- 2.22 rem
Built-In Photon Dose Function	248.24 +/- 64.6 mrem

The two methods used to calculate neutron dose resulted in similar dose estimates. The estimate from the built-in dose function method was 7.51 rem while the estimate from the user entered flux to dose conversion method was 8.88 rem. These results have 15.4% difference which shows how different dose calculation methods will affect the final estimate. Neutron dosimetry can be quite challenging due to the differing radiation quality factors needed for different energy neutrons. It is likely that the two different methods used slightly different approaches for applying these quality factors. To get the best estimate of the neutron dose, an average of the two was taken. This results in a neutron dose of 8.2 +/- 2.05 rem. This estimate is in line with prior lab members' estimates that were on the order of 1 rem.

The photon dose estimate was 248.24 mrem. This is a very reasonable number and aligns with the estimates from former lab members that used a better calibrated EPD. Their estimates were between 200-300 mrem.

The total estimated dose of 8.45 +/- 2.05 rem is higher than the dose limit chosen for this work which was 5 rem. This limit is conservative; 10% of the annual dose limit of 50 rem for an extremity. Since this is still within the regulatory limit, it is technically acceptable, but efforts should be made to reduce it to below the 5 rem limit to better abide by the ALARA principle.

3.3.2.2 Neutron Yield Estimation Using TLD Results and MCNP

Although the TLD results were determined to be inaccurate as discussed in section 3.3.1, the neutron dose estimates from TLDs #1 and #4 were still used to estimate the neutron yield of the system. This was done to further confirm the inaccuracy for the results. Using the average neutron dose from TLDs #1 and #4, which was 15.94 rem, and Equation 21, the estimated neutron yield was estimated for both MCNP neutron dose simulation methods. The results from the built-in dose function simulation method yielded a neutron yield estimate of 4.02E+09 neutrons per second. The user defined flux to dose conversion simulation method yielded a neutron yield estimate of 4.76E+09 neutrons per second. Both neutron yield estimates are higher than the quoted peak yield of 3E+09 neutrons per second. This means that it would be highly unlikely to have a dose as high as the TLD readings. It can therefore be confirmed that these TLD readings are not accurate to the true dose received inside the irradiation cave.

3.3.3 EPD Dose Measurement Results

As discussed previously, the EPD used in this work was not properly calibrated for this source. Therefore, the absolute dose reported from the device was not accurate, but it still provided useful reference dose information. The dose readings from the EPD were used to determine if the amount of radiation produced was consistent between all runs of the generator. The EPD was placed in the irradiation cave for all bone phantom and cadaver bone irradiations and the dose readings are presented in Tables 3.4 and 3.5

Table 3.4. EPD Readings from Bone Phantom Experiments

Phantom	**Neutron Dose [rem]**	**Photon Dose [mrem]**
0 ppm	14.25	308.1
0.5 ppm	13.38	330.55
1 ppm	13.05	294.9
2 ppm	13.59	311.9
5 ppm	14.06	324.9
10 ppm	13.56	314.7
15 ppm	13.88	330.10
20 ppm	13.46	343.6
30 ppm	13.38	365.3
40 ppm	14.55	298.3
Average	13.72	322.24
Standard Deviation	+/- 0.436	+/- 20.33

Table 3.5. EPD Readings from Cadaver Bone Experiments

Sample ID#	**Neutron Dose [rem]**	**Photon Dose [mrem]**
27900	12.86	285.1
27898	13.46	309.3
29699	12.25	302.2
29698	12.82	284.0
29697	12.36	308.9
25456	12.62	287.6
27899	13.05	293.7
25457	11.90	344.0
27895	12.59	290.0
29696	11.29	304.0
27896	12.05	278.4
27897	12.30	286.7
Average	12.46	297.8
Standard Deviation	+/- 0.5729	+/- 17.79

As seen in Tables 3.4 and 3.5, the EPD readings from inside of the irradiation cave are consistent between generator runs. All dose readings fall within +/- 3σ of the mean and can be considered statistically fluctuating around a common true value. This means that the differences in signal measured from these samples was due to differences in target element concentration alone and not changes in irradiation. Something interesting to note is that the average neutron and photon dose readings from the bone phantom trials are slightly higher than those for the cadaver bone trials. The cadaver bone irradiations were done the week following the bone phantoms which might suggest that there can be some drift in the neutron production of the machine from week to week.

Again, it is important to note that these dose values are relative and not absolute since the EPD is not properly calibrated to our source. The dose estimates obtained from the MCNP simulations are considered the true, absolute dose for 10 minutes of irradiation. These values were 8.2 rem for neutron dose and 248.24 rem for photon dose. Using these numbers as the true dose, the EPD seems to over estimate the neutron dose by a factor of ~1.5 and the photon dose by a factor of ~1.2.

3.4 Discussion

The dose results from the TLD readings ended up not being as useful as originally hoped. The values for the neutron dose were higher that the total dose for three of the TLDs which raised concerns about the accuracy of the reading method and final results. Also, the expected behaviors of reproducibility and backscatter dose enhancement were not seen. Along with these concerns, the dose values themselves seemed too high for the doses that were expected. As a means to verify the inaccuracy of these readings, the values were used along with MCNP simulation to estimate the neutron yield of the system needed to generate those doses. This resulted in neutron yield estimated of between 4-4.4E+09 neutrons per second which is unlikely for this system. For these reasons the dose reading from the TLDs were not usable.

Using two different methods of MCNP dose simulation to estimate the neutron and photon dose received during a 10-minute irradiation provided more reasonable dose estimates. The estimated average neutron dose calculated from the two MCNP methods and using a neutron yield estimate found in chapter 2 of 2.24E+09 n/s was 8.2 +/-2.05 rem. The estimated photon dose was 248.24 +/- 64.6 mrem. This gives a total dose of 8.45 +/- 2.05 rem. This result seems plausible when compared to the total equivalent dose estimated by Liu for the old D-D 109 system of 3.59

rem for 10 minutes[19]. If we assume that dose should scale proportionally with neutron yield, the higher yield estimated for the new system would result in a dose very close to our estimate. These estimates will be used as our best dose estimate. This estimate for dose is higher than the chosen limit of 5 rem and will required further optimization of the moderation of the assembly to reduce the dose to an acceptable level.

The EPD was used to check for consistency in the irradiation between generator runs. Since the EPD was not calibrated to our system, it could only be used in a relative sense. The results from the EPD showed that the level of irradiation was consistent for all the bone phantoms and again for the cadaver bones. While the reading between cadaver bone runs were all consistent, the average reading for the cadaver bones was slightly lower than that for the bone phantoms. This suggests that during different time periods (weeks or months) the neutron generation level may fluctuate slightly.

A final note of discussion is the choice to trust the simulated dose estimate over two experimental dose estimates that were in similar agreement (the TLDs and EPD). Typically, experimental results are considered more reliable than simulation because it better represents the true experimental conditions. The choice to trust the accuracy of the simulation over the TLD and EPD readings was made based on two factors. Firstly, as mentioned, an estimate of the neutron yield required to produce the doses measured with the TLD was determined to be around 4.4E+09 neutrons per second. The peak yield quoted for our device is around 3E+09 so it is unlikely that the true yield is high enough to produce the dose that was measured on the TLDs. The second factor explains why similar dose measurements were seen on the TLDs and EPD. Both devices were calibrated using a standard neutron source at their respective manufactures. We were unable to find out the identity of either calibration source, but it is likely that both manufacturers used a similar standard neutron calibration source. This would explain why the responses are so similar. Also, the standard source is likely much simpler in energy distribution than the unique neutron source produced from our generator. This means the calibration cannot accurately represent dose from our system. This would explain why the dose estimate from the TLDs and EPD is different than the dose expected.

CHAPTER 4. MANGANESE IN HUMAN CADAVER BONE

4.1 Introduction

After validating and characterizing the detections system's ability to detect Mn in bone using bone phantoms, the next step before the system can be used in-vivo is to use the system for measuring Mn in human cadaver bones. This way, there is still no risk to a living individual, but the system can be tested using real human tissue which will mimic the in-vivo measurement. In this chapter, the experimental irradiation and measurement of 12 human cadaver bone samples from Mn exposed and control miners will be presented.

4.2 Materials and Methods

4.2.1 Description of Human Cadaver Bone Samples

The human cadaver bones used in this work were provided by collaborators at Washington University School of Medicine. The bones were collected from human cadavers of 12 miners. Four of the miners were Mn miners while the other eight were asbestos miners. The eight asbestos miners that did not mine Mn were used as controls. For this work, we chose to not know which bones came from the Mn miners versus the control miners before we complete the Mn data analysis. This was done in order to evaluate the ability of our detection system to detect a real sample with Mn out of a group of controls. Each bone was given a sample ID number to keep track of which was which.

The bones were all sternum bones. Each bone sample was a different size and was cleaned of soft tissue to varying degrees. Some of the samples had significant amounts of muscle and fat surrounding the bone while others were mostly bare bone. It is unlikely that the various amounts of soft tissue will affect the Mn measurements since Mn is not stored in soft tissue unless the exposure was extremely recent. The different sizes of actual bone must be accounted for and the method used to do so is addressed in a later section. All samples were contained in Formalin jars stored in a refrigerator to prevent decomposition. In order to irradiate and measure the samples, they were removed from the Formalin, dried with paper towels, and then vacuum sealed in plastic bags. Following irradiation and measurement, the samples were placed back in the Formalin jars.

An example of one of the vacuum sealed bones is shown in Figure 4.1. Photos of all samples are in Appendix B.

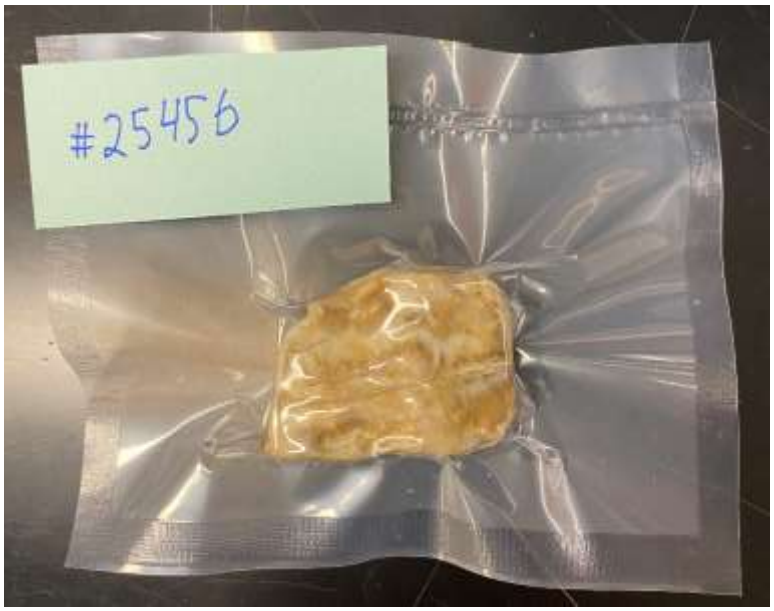

Figure 4.1. Human Cadaver Bone Sample #25456

4.2.2 Experimental Irradiation and Measurement Protocol

The irradiation of the bone samples was conducted in the same manner as the bone phantoms which was outlined in detail in section 2.2.3.2. The plastic sealed bones were placed flush against the left wall of the irradiation cave and irradiated for 10 minutes. Directly following the irradiation, 5 minutes were allotted for decay. During this decay period, the samples were moved from the irradiation cave to the HPGe measurement cave. The sample was placed flush with the detector surface and then enclosed by lead bricks. A measurement was collected for a total of 2 hours. This longer measurement time was chosen to increase the sensitivity of Mn detection. When measuring a smaller signal, it is advantageous to measure for a longer period of time in order to increase the amount of the total signal collected.

4.2.3 Normalization of Mn Counts to Ca Counts

As mentioned in section 4.2.1, the cadaver bone samples were different sizes. This introduces a bone mass dependence on the signal. For example, a large bone with 1 ppm Mn

concentration contains more Mn than a small bone with 1 ppm Mn concentration even though they have the same concentration. This is because the large bone has more mass and therefore more Mn. Since our detection system is calibrated to measure the concentration of Mn, a method needed to be developed to correct for the size dependence of the samples.

The method chosen was to normalize the Mn counts measured for each sample to the Calcium (Ca) counts for each sample. Ca is one of the major components of bone, constituting about 21.5% of bone mass[20]. Therefore, a more massive sample will have proportionally more Ca in it than a smaller sample. By dividing the Mn counts by the Ca counts, the difference in mass between samples is eliminated.

The amount of Ca can be measured by the neutron activation analysis of Ca-48. Ca-48 is activated by thermal neutron capture during the irradiation process and becomes Ca-49 which emits a gamma signal that can be detected. The process is outlined in Equation 22. The Ca-49 decays with a half-life of 8.72 minutes and emits a 3084.4 keV gamma ray with a branching ratio of 90.72% [11].

$$^{48}_{20}Ca + n \rightarrow {}^{49}_{20}Ca^{*} \rightarrow {}^{49}_{21}Sc + \beta^{-} + \bar{\nu} + \gamma\ [3084.4\ keV] \qquad (22)$$

The counts coming from the Ca-49 gamma ray were determined using the MATLAB peak fitting script described in section 2.2.3.3. The fitting equation used was the same as that used for Mn fitting except it did not include the component for a second nearby peak. The Ca peak stands on its own without close by peaks. To create a calibration curve of Mn normalized to Ca, the results from the experimental bone phantom measurements were used. The counts attributed to Ca were determined from the measured experimental spectrum of each bone phantom. Finally the points from the corrected Mn calibration curve in Figure 2.13 were divided by their corresponding Ca counts to create a Mn/Ca calibration curve which is shown in Figure 4.2 and the fitting equation is given in Equation 22.

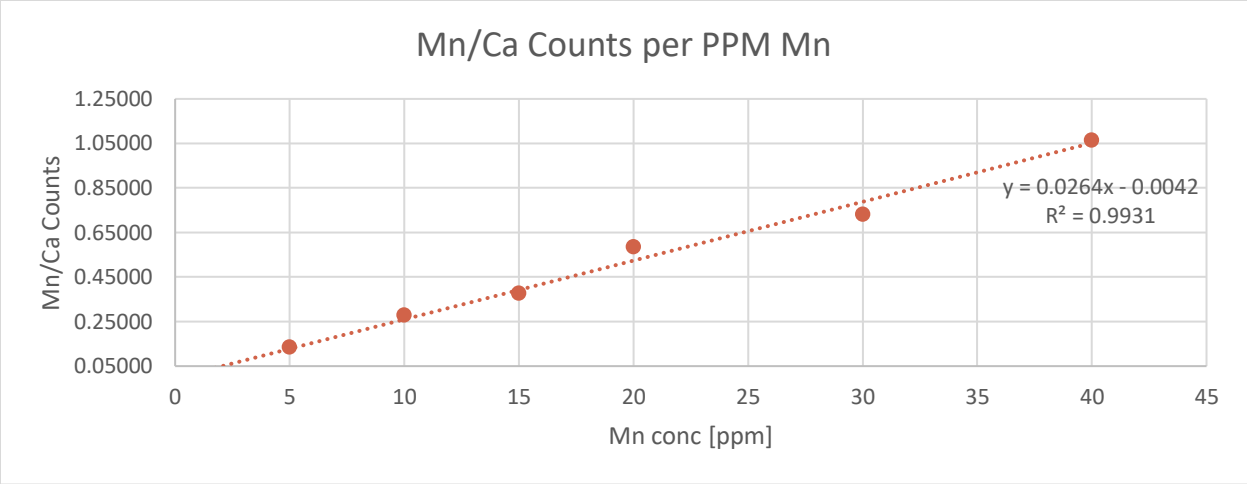

Figure 4.2. Mn Calibration Curve Normalized to Ca

$$Y = 0.0264 * X - 0.0042 \quad (22)$$

It is important to note that the bone phantom measurements used to create the calibration curve in Figure 4.2 were collected for 1 hour while the cadaver bone measurements were collected for 2 hours. Therefore, to use this calibration curve to determine the concentration of Mn in the cadaver bones, the 2-hour cadaver bone measurements must be scaled back to the counts that would have been observed from 1 hour only. To do this, Equation 4 must be manipulated and implemented. Previously, Equation 4 was used to solve for the number of counts expected for a given level of activation. Now, the counts are known and the activity of each sample can be solved for. Once we know the activity produced in each cadaver bone, the equation in its original form can be used along with a counting correction factor corresponding to 1 hour to estimate the counts expected in 1 hour instead of 2. Since the half-life of Mn-56 is longer than the counting time, it is expected that reducing the counting time by half will reduce the amount of counts by around half. The Ca-49, however, has a half-life of about 8 minutes so most of the counts are seen in the first hour. Therefore, the counts seen in 2 hours versus 1 hour will be very similar.

4.3 Results

4.3.1 Calcium Signals Measured from Cadaver Bones

As described in section 4.2.3, Ca is one of the major components of bone. Ca constitutes about 21.5% of the mass of bone according to ICRP Report 89[20]. Therefore, all cadaver bone samples will contain Ca, with larger samples having more Ca than smaller samples. The gamma signal emitted from the activated Ca-49 for each bone should be proportional to the mass of bone present in the sample. The number of Ca counts was determined by using the MATLAB peak fitting script to fit the Ca peak from the gamma spectra collected with Maestro. The masses of each sample along with the Ca signal measured after neutron activation are presented in Table 4.1. Also, the relationship between sample mass and Ca signal is plotted in Figure 4.3.

Table 4.1. Cadaver Bone Ca Signal Results

Bone ID#	Mass [g]	2 Hour Ca Counts
27900	5.83	42.46 +/- 7.30
27898	8.92	6.37 +/- 3.60
29699	20.39	78.16 +/- 9.70
29698	20.6	132.77 +/- 12.28
29697	21.12	72.74 +/- 9.49
25456	21.95	142.91 +/- 12.80
27899	30.18	123.38 +/- 11.66
25457	30.56	169.32 +/- 14.16
27895	44.68	59.95 +/- 8.79
29696	46.14	7.76 +/- 4.14
27896	65.2	174.18 +/- 15.19
27897	102.06	343.12 +/- 19.88

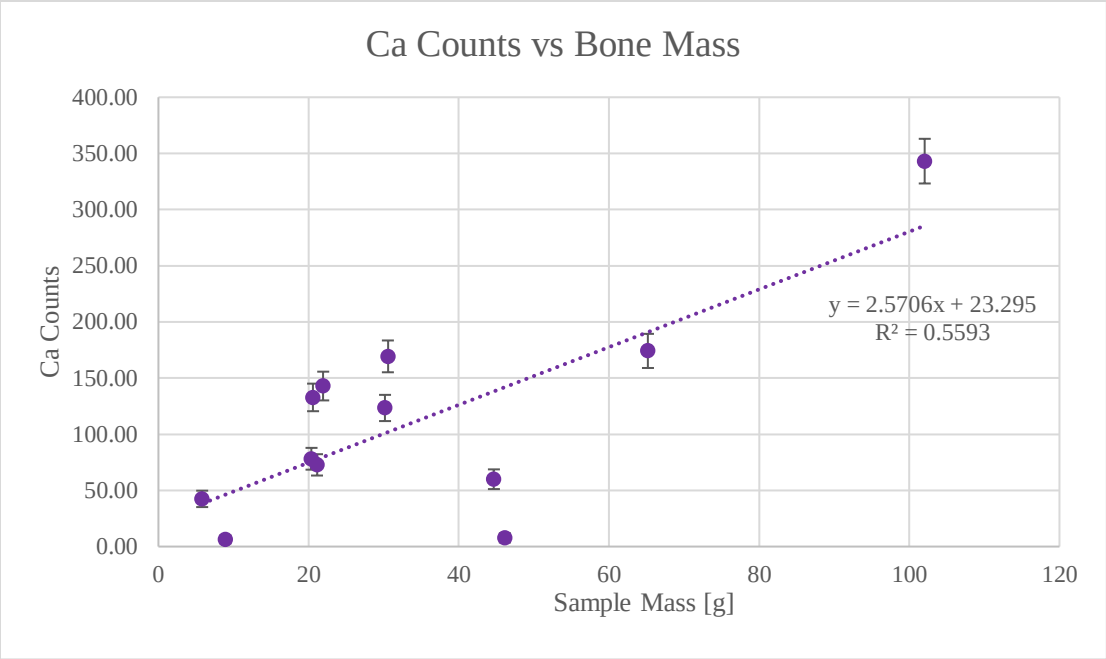

Figure 4.3. Relationship Between Bone Sample Mass and Ca Counts

With the exception of three samples, the correlation between sample mass and Ca counts is fairly strong and positive. There are some fluctuations from the trendline which make sense because the mass of the samples included bone as well as soft tissue. As mentioned before, some of the samples had more soft tissue while others were mostly bare bone. Therefore, the mass is not a perfect reflection of the amount of bone in the samples. If the mass had been of the bone alone, it is expected that a stronger correlation would be observed.

It must be addressed that there were three cadaver bone samples that showed extremely low to almost no Ca signals. These samples were #27898, #27895, and #29696. These results were unexpected and puzzling. At first, it was considered that perhaps there was no bone in these three samples, simply all soft tissue. The samples were closely examined through visual and physical examination and bone was clearly seen in all three. Next it was considered that perhaps there was an error with the irradiation or measurement of these samples, so these bones with the lowest Ca signals were irradiated and measured again. The repeated measurements showed identical results of extremely low Ca signals.

The Ca signal versus sample mass was replotted, excluding the three very low Ca signal samples. This is given by Figure 4.4. When the three low Ca signal samples are removed, the R^2

value increases from 0.5593 to 0.8596. This shows that aside from those three unusual samples, there is a strong, positive correlation between Ca signal and sample mass.

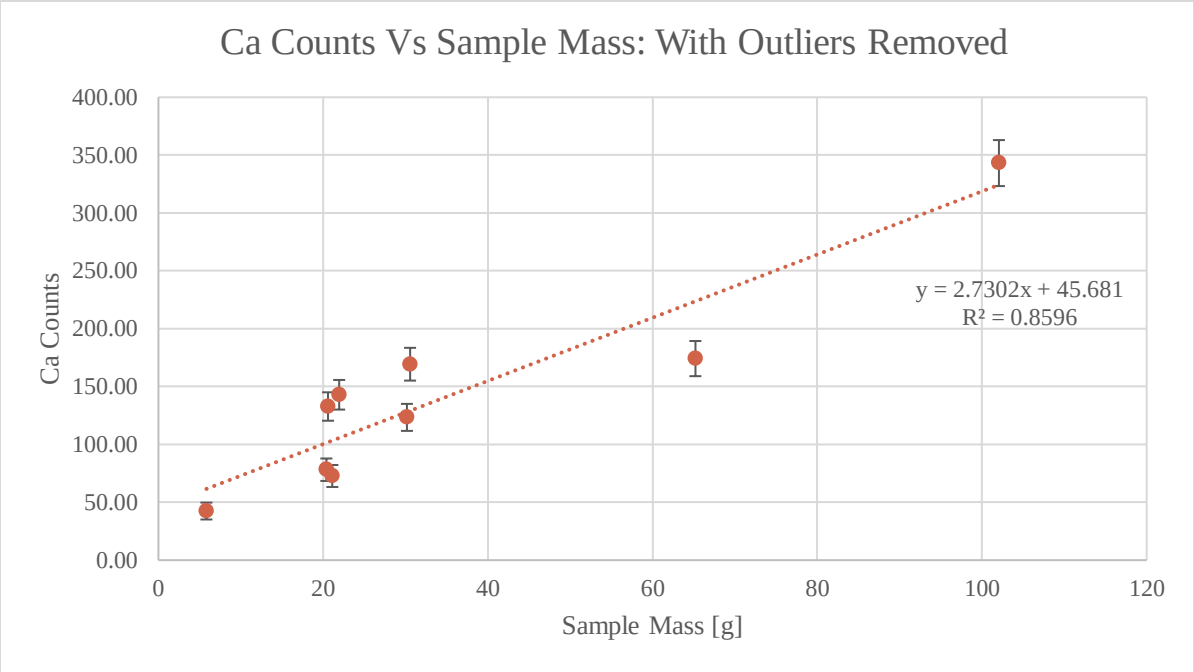

Figure 4.4 Ca Counts vs Sample Mass with Three low Ca Signal Samples Excluded

Since these low Ca signals could not be explained by the reasoning above, there is currently no explanation for these results. Further analysis and work must be performed to look for an explanation of these unexpected results since there should be clear Ca signals coming from all bones.

4.3.2 Mn Signals and Determination of Mn Concentration

4.3.2.1 Mn Signals Measured from Cadaver Bones

After the cadaver bones were irradiated and measured with the HPGe detector, the gamma ray spectra were collected using the Maestro software. The spectra were then uploaded into the MATLAB peak fitting script and were fit in the region of 846 keV which is the energy of the Mn-56 gamma. The majority of the bones had low Mn signals since two thirds of the bones were from control individuals but several of the samples showed distinct peaks at the 847 keV energy. An

example of one of the distinct Mn peaks fit with the MATLAB script is shown in Figure 4.5. This comes from sample #29698. The Mn counts from each of the samples are presented in Table 4.2.

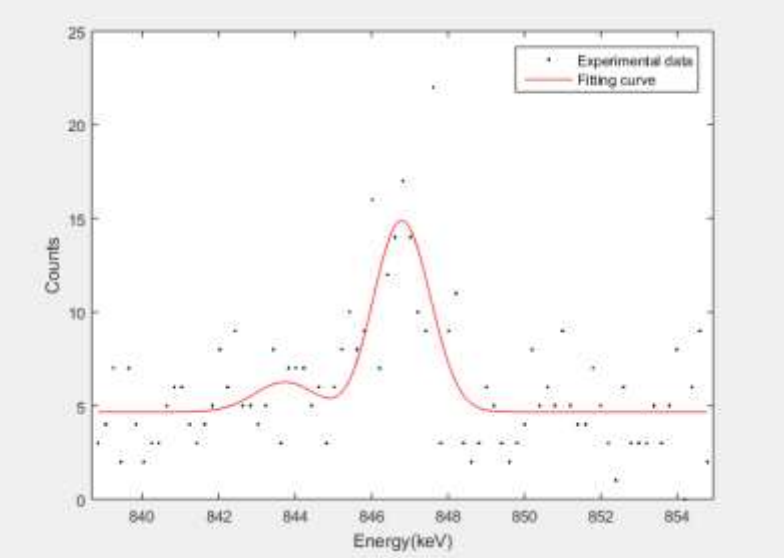

Figure 4.5. Mn Signal from Cadaver Bone #29698

Table 4.2. Cadaver Bone Mn Signal Results

Sample ID#	2 Hour Mn Counts
27900	25.43 +/- 9.95
27898	22.42 +/- 10.73
29699	80.05 +/- 13.74
29698	84.58 +/- 14.92
29697	32.57 +/- 13.67
25456	38.71 +/- 13.49
27899	33.77 +/- 14.00
25457	5.78 +/- 13.68
27895	34.04 +/- 13.65
29696	47.83 +/- 12.54
27896	21.09 +/- 16.73
27897	50.66 +/- 15.74

The 2-hour Mn signals were plotted versus sample mass and this relationship is shown in Figure 4.6.

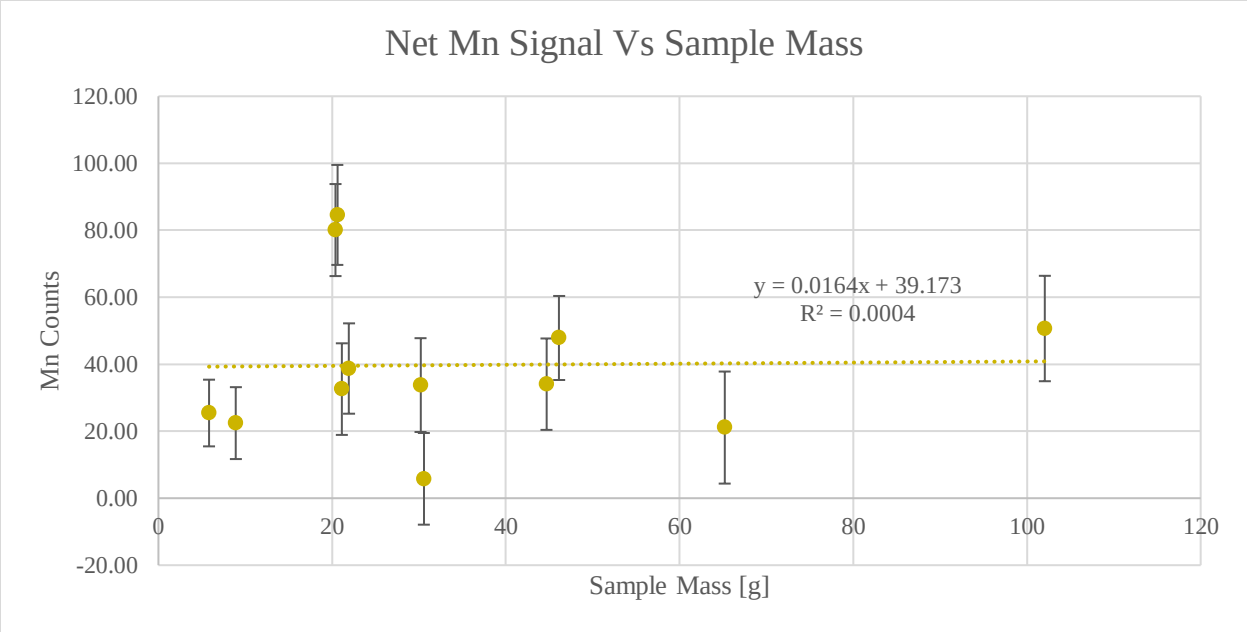

Figure 4.6. Net Mn Signal Versus Sample Mass

As shown in Figure 4.6 there does not appear to be any relationship between the Mn signal and the mass of the samples. This result is unexpected. Since 8 of the 12 bones came from unexposed workers, it would be assumed that 8 of the bones would have similar Mn bone concentrations of around 1 ppm as suggested by ICRP as the standard Mn concentration in bone[20]. If this were the case, an increasing trend would be seen in the Mn signals as the sample mass increased. This is because a larger bone with 1 ppm Mn concentration will have more Mn in it than a smaller bone with 1 ppm Mn concentration. Along with an increasing relationship seen with 8 of the samples, we should also see 4 samples that rise above the standard increasing trend. These would be the 4 exposed bones. These results suggest that the unexposed bones may not have similar Mn concentrations and calls for more exploration which is included in later sections.

At this stage, the four bones showing the highest Mn signal were samples #29699, #29698, #29696, #27897. These Mn signals must be normalized to their corresponding Ca signal to estimate the Mn concentration in each bone sample.

4.3.2.2 Estimation Results of Mn Concentration in Cadaver Bone

The Mn and Ca counts determined from the 2-hour cadaver bone measurements were scaled back to 1-hour counts using the method outlined in section 4.2.3. Then the 1-hour Mn counts were divided by the 1-hour Ca counts. Finally, these ratios of 1-hour Mn to Ca counts were used along with Equation 22 to estimate the Mn concentration for each cadaver bone sample. The results along with their uncertainties are presented in Table 4.3. The three bones with few or no calcium signal were excluded from the table.

Table 4.3. Cadaver Bone Mn Concentration Estimates

Sample ID#	1 Hour Mn Counts	1 Hour Ca Counts	1 Hour Mn/Ca Ratio	Mn Concentration [ppm]
27900	14.41 +/- 5.64	42.10 +/- 7.24	0.34 +/-0.15	13.17 +/- 5.63
29699	45.38 +/- 7.79	77.50 +/- 9.62	0.59 +/- 0.12	22.52 +/- 4.77
29698	52.14 +/- 8.46	131.65 +/- 12.17	0.40 +/- 0.07	15.23 +/- 2.79
29697	18.46 +/- 7.75	72.13 +/- 9.41	0.26 +/- 0.11	9.84 +/- 4.33
25456	21.94 +/- 7.65	141.71 +/- 12.69	0.15 +/- 0.06	5.96 +/- 2.14
27899	19.14 +/- 7.94	122.34 +/- 11.57	0.16 +/- 0.07	6.02 +/- 2.56
25457	3.28 +/- 7.76	167.90 +/- 14.04	0.02 +/-0.05	0.75 +/- 1.78
27896	11.95 +/- 9.48	172.72 +/- 15.06	0.07 +/- 0.06	2.66 +/- 2.12
27897	28.72 +/- 8.92	340.24 +/- 19.72	0.08 +/- 0.03	3.25 +/- 1.03

The majority of the Mn concentration estimates seen in Table 4.3 are higher than expected as only four of the cadaver bone samples came from individuals who were occupationally exposed to Mn. All other samples were not occupationally exposed and should therefore have an Mn bone concentration level close to the ICRP standard value of 1 ppm. Only one sample, #25457, had an Mn bone concentration estimate that was close to this value. All other estimates were higher than this value making it difficult to determine which of the 3 samples were from occupationally exposed workers. Further work is needed to determine whether there is an overestimation in Mn concentration for these cadaver bones or if the bone Mn concentration for these bones are in fact high.

To include all the samples in the analysis, we used the relative concentration, i.e. the ratio of Mn counts measured from the 2-hour measurements divided by the mass of the sample. The principle here is that a sample with a high Mn concentration will yield a larger Mn signal per unit

mass. It is important to state again that the samples had varying amounts of soft tissue so the sample mass is not from bone alone. This introduces some variability in the accuracy of this metric. It would be best to have the mass of the bare bone. These estimates are presented in Table 4.4.

Table 4.4. Mn Signal Per Unit Mass in Cadaver Bone Samples

Sample ID#	Mass [g]	Mn Counts/Mass
27900	5.83	4.362 +/- 0.726
27898	8.92	2.513 +/- 0.435
29699	20.39	3.926 +/- 0.531
29698	20.6	4.465 +/- 0.533
29697	21.12	1.542 +/- 0.273
25456	21.95	1.764 +/- 0.291
27899	30.18	1.119 +/- 0.198
25457	30.56	0.189 +/- 0.034
27895	44.68	0.762 +/- 0.116
29696	46.14	1.037 +/- 0.135
27896	65.2	0.323 +/- 0.051
27897	102.06	0.496 +/- 0.090

This method of estimating the relative Mn concentration in the cadaver bone samples suggest that samples #27900, #29699, #29698, and #27898 have the largest Mn concentration. Therefore, this is the best guess for the four samples that came from occupationally exposed miners.

To determine if there was any relationship between Mn signal per sample mass and sample mass, these parameters were plotted against each other in Figure 4.7. The relationship observed was very interesting. It would be expected that there is no relationship between the relative concentration of Mn and the mass of the sample. A smaller or larger bone sample should not have any effect on the Mn concentration. However, a significant decreasing logarithmic relationship was observed. This suggests that the smaller bone samples had higher Mn concentrations than larger samples. An initial thought to explain this observation was that perhaps there was attenuation of the Mn signal in the larger samples, but the penetrating power of the gamma rays emitted is large enough that the attenuation caused by the sample should be minimal. Another possible explanation is that different methods were used when harvesting the bones. Perhaps the

person harvesting the bones from the exposed workers preferred to take smaller samples while the person harvesting bones from the unexposed workers took larger samples. This is possible though not likely. It is unlikely that our collaborators would have used different harvesting techniques for the two groups. This observation calls for more analysis of the bones to explore other possible explanations.

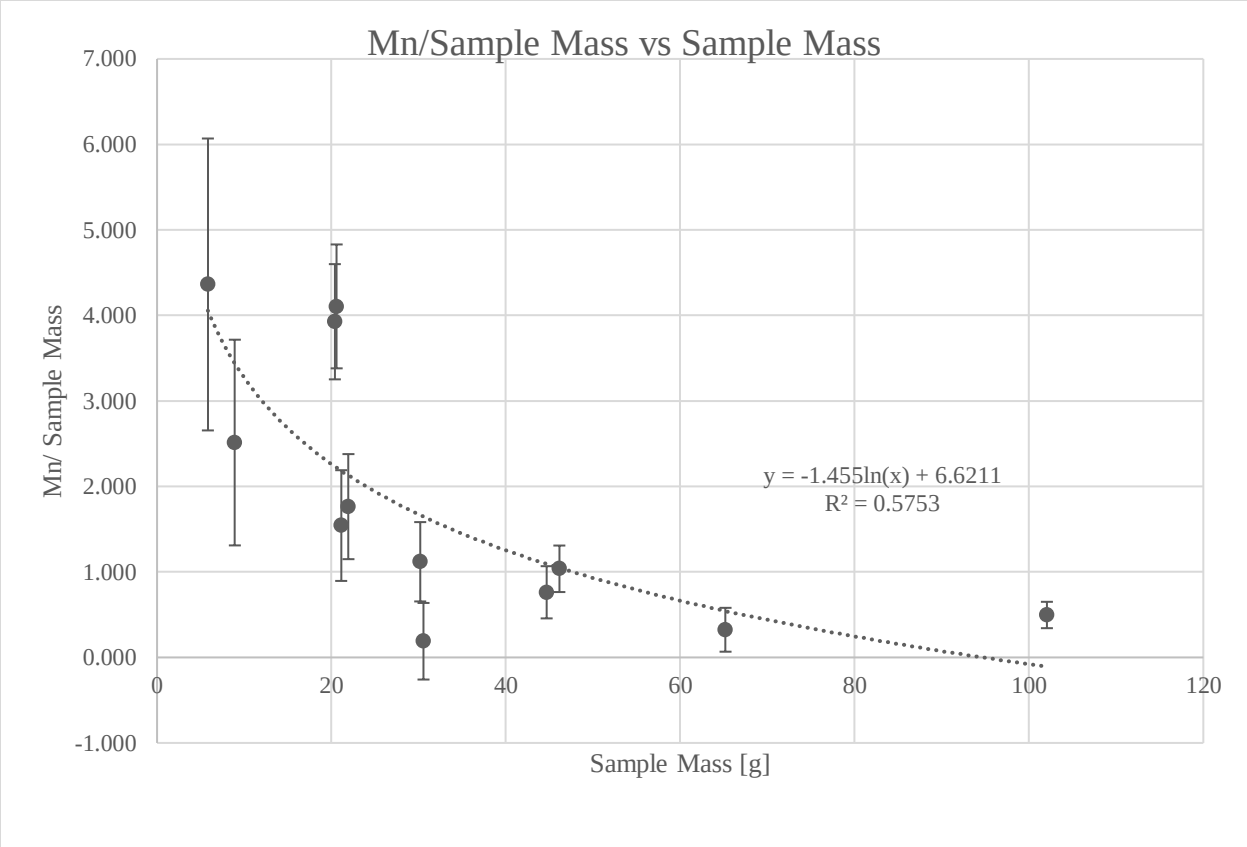

Figure 4.7. Mn Signal per Sample Mass Versus Sample Mass

4.3.2.3 Identity of Exposed Bones and Statistical Analysis

After making our best guess at identifying the 4 bones coming from the Mn miners, our collaborator was contacted to learn the true ID#'s of the exposed bones. The ID#'s of the four samples coming from the Mn miners were #27900, #29698, #27895, and #27896. Therefore, we were only able to correctly identify two of the exposed samples using the Mn per sample mass metric. Some statistical analysis was performed to see if there were any significant differences in the results seen between the exposed and unexposed samples.

The main metric used to see if there was any significant difference in the response between the exposed and unexposed samples was the beta value of a linear regression of the Mn per sample mass plotted on a binary curve. The beta value indicates the amount of change in the dependent variable seen between the two independent variables, here unexposed (0) and exposed (1). A large beta value shows that there is a significant change in the dependent variable, here Mn per sample mass, when the independent variable is changed. These linear regression plots are shown in Figures 4.8.

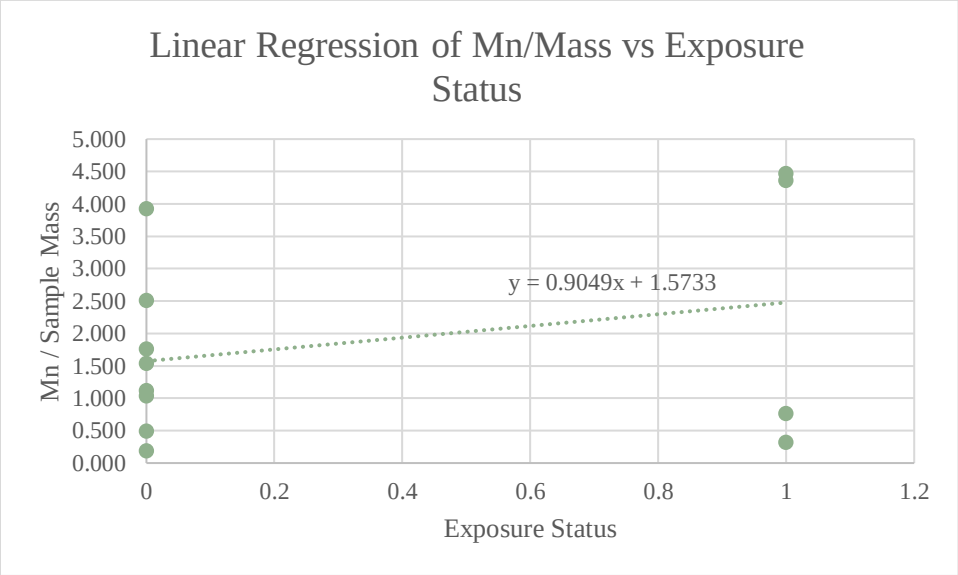

Figure 4.8. Linear Regression of Mn/Mass vs Exposure Status

The beta value found for Mn per sample mass and exposure status was 0.9094. While the regression shows minor positive trends, it is not statistically significant.

This lack of statistically significant increase can be partially explained by two things. First, there were several bones from unexposed individuals that gave large Mn signals. This drives the overall average of net Mn counts and Mn per sample mass up for the unexposed group. This in turn lowers the beta value. Also, some of the bones had significantly more soft tissue than others. This drives up the value for the mass of the sample without increasing the amount of bone present. If the samples with large amount of soft tissue had been better cleaned, the mass would have been lower and some of the Mn per sample mass ratios would have increased. This is particularly relevant for the two exposed samples that had very low Mn per sample mass ratios. These two

samples had some of the most soft tissue of all the samples. This means that their sample mass values were higher than what it would be for bare bone alone.

The large Mn signals coming from nonexposed individuals suggest that they may have been unknowingly exposed to Mn. Further data should be gathered on those individuals to see if they could have been exposed to Mn as well. In order to address the issues of varying amounts of soft tissue, efforts should be made going forward to clean as much soft tissue off of the bones as possible.

4.4 Discussion

This portion of the work aimed to evaluate the system's ability to determine Mn concentration in human cadaver bone samples. The cadaver bone samples used were from 12 miners of whom 4 were Mn miners. The goal was to see if the system would be sensitive enough to determine which 4 samples came from the occupationally exposed miners. The first major take away is that Mn signals were able to be detected in the cadaver bones. All of the bones showed Mn signals with some being higher than others, suggesting these came from Mn exposed individuals. Confirming this ability is an important step of continuing to work toward the goal of using this system for in-vivo measurements. The Mn signals observed, however, did not follow the trend expected when plotted versus sample mass. There was no significant relationship between Mn signal and sample mass. This suggests that Mn concentration was not consistent between the unexposed samples.

It was also found that three of the bone had little to no Ca signal. This result was unexpected and cannot be explained at this time. Because of this, the method used for estimation of Mn concentration using the normalized Mn/Ca calibration line will overestimate the concentrations. Therefore, accurate estimates of the Mn concentration in the cadaver bones were unable to be determined. As a means for estimating the relative Mn concentration in the bones, the Mn signals measured were divided by the sample masses. This provided a metric of Mn counts per sample mass. Using this metric, there were four samples that stood out above the rest and were the best estimate for the 4 bones coming from Mn exposed workers. These bones were #27900, #29699, #29698, and #27898.

After comparing these results to the four true exposed samples, we were only able to correctly identify two of them. Statistical analysis was performed to determine if there was any

statistically significant variation between the Mn signals measured between the exposed and unexposed samples. While it was found that there was a slight positive increase in Mn per Mass between the unexposed and exposed groups, it was not statistically significant. By cleaning bones of all soft tissue and investigating further into possible unknown Mn exposures of the unexposed workers, a more statistically significant trend would likely be seen. It was also found that there was a significant relationship between Mn per Mass and Sample Mass. Smaller samples were found to have higher relative Mn concentrations than larger bones which was unexpected.

CHAPTER 5. CONCLUSION

The first portion of this work aimed to assess the capability of the new, D-D 109M neutron generator and HPGe detection system's ability to detect Mn concentration using MCNP simulation and physical experiments. The first major finding was an estimate of the neutron generator's neutron production capability. The best estimate found for the neutron yield in this work was 2.24E+09 +/- 2.15E+07 neutrons per second. This value is on par with what was expected and shows a large increase in neutron yield compared to the older D-D 109 system which has a yield of 7E+08 neutrons per second. This increased neutron yield will hopefully allow for better neutron activation in samples. The level of Mn activation achievable with the current system configuration and experimental irradiation and measurement procedure was determined to be about 50 counts per ppm concentration of Mn in the sample. This led to an estimated Mn detection limit of 0.428 ppm. This is slightly worse than the detection limit estimated by Liu for the older D-D 109 generator[19]. This suggests that even though the new system has a higher total neutron flux than the old system, the thermal fluxes are about the same. This means that the extra neutron flux is currently going to waste in terms of neutron activation and is simply increasing the dose. This calls for better optimization of the new generator's moderation and reflection assembly to increase the thermal flux, increase the neutron activation, and decrease the detection limit.

The second portion of the work focused on estimating the equivalent dose received by a sample for the current irradiation protocol of 10 minutes. Using MCNP simulation, the best estimate found in this work for neutron dose was 8.2 rem and 248.24 mrem for photon dose. This gives a total equivalent dose of 8.48 +/- 2.05 rem. This estimate is larger than the guiding dose limit for this work which was 5 rem. 5 rem is a conservative value that is 10% of the 50 rem annual limit for an extremity. Therefore, the dose is below the annual limit but work should still be done to further minimize the dose and bring it below the 5 rem threshold. It is always a best practice to keep the dose As Low As Reasonably Achievable. An ideal balance must be struck between keeping the dose low while still maintaining a strong neutron activation ability.

The third and final portion of this work aimed to assess the system's ability to detect Mn concentration in human cadaver bones. The system was able to measure Mn signal in all bone samples, with some signals more pronounced than others. This finding confirmed that the system is able to detect Mn in small amounts present in human bone which is promising for the future

goals of using this system for in-vivo bone measurements. An unexpected finding was also found in this portion of the work. The Ca signal in three of the bone samples was almost undetectable. This was very puzzling as all bone should contain the same percentage of Ca. These low Ca signals made it very difficult to make an accurate estimate of the Mn concentration in the bones using the normalized Mn/Ca calibration curve. Although we were unable to determine the Mn concentration in the bones as originally hoped, we were able to analyze a relative metric to estimate the bone Mn concentration. This metric was Mn counts per unit sample mass. These results showed a slightly higher average value in the exposed versus unexposed samples, but the difference was not statistically significant. This could likely be improved by cleaning the bones of soft tissue and checking for any unknown Mn exposures in the unexposed workers. A significant relationship between Mn counts per unit sample mass and sample mass was observed which was not expected. The size of the sample should not have an effect on the Mn concentration in the sample. This observation along with the 3 very low Ca signals were the two most interesting findings in this section. At this time, no explanation could be found for either. Further work should be pursued to find an explanation to these interesting observations.

Future work should include further improving the detection limit of the system, finding the reason for the low Ca counts and unexpected trend between Mn concentration and sample mass for the cadaver bones, optimizing the calibration procedure for in-vivo bone Mn quantification, comparing the IVNAA bone Mn results with the results from a “gold standard” method for cadaver bones, and analyzing more bones (i.e. increasing sample size).

APPENDIX A. MCNP INPUT FILES

Neutron Generator Assembly Input File

```
MCNPX Visual Editor Version X_24E
   1   208  -2.699 -1 :-20 :-21 :-22 :-23 :(-24 25 ) IMP:N=1 IMP:P=1 IMP:E=1
   2   204 -0.001225 1 2 3 4 5 6 7 8 9 10 11 12 13 14 15 16 17 18 19 &
20 21 22 23 24 25 90 100 101 103 104 105 106 &
107 108 110 116 122 135 136 137 &
123 124 127 128 129 130 131 132 133 134 91 -200 IMP:N=1 IMP:P=1 IMP:E=1
   3   256   -0.93 (-2 15 16 ):-3 :-4 :-5 :-6 :-7 15 17 18 19 #4&
IMP:N=1 IMP:P=1 IMP:E=1
   4   999 -1.69e-010 #12 #13 -8 IMP:N=1 IMP:P=1 IMP:E=1
   5   204 -0.001225 200 IMP:N=0 IMP:P=0 IMP:E=0
   6   208  -2.699 (-9 10 ):(-11 12 ):(-13 14 ) IMP:N=1 IMP:P=1 IMP:E=1
   7     0        #3 #4 #12 #13 #14 -10 IMP:N=1 IMP:P=1 IMP:E=1
   8     0        #3 #4 #13 #14 -12 :-14 IMP:N=1 IMP:P=1 IMP:E=1
  10   317   -4.98 -15 IMP:N=1 IMP:P=1 IMP:E=1
  11   209   -8.96 #10 -16 IMP:N=1 IMP:P=1 IMP:E=1
  12   498  -4.506 -17 IMP:N=1 IMP:P=1 IMP:E=1
  13   208  -2.699 -18 19 IMP:N=1 IMP:P=1 IMP:E=1
  14     0        #4 #12 -19 IMP:N=1 IMP:P=1 IMP:E=1
  15     0        #6 #8 -25 IMP:N=1 IMP:P=1 IMP:E=1
  16   256   -0.93 -90 IMP:N=1 IMP:P=1 IMP:E=1
  17   252  -11.35 -100 IMP:N=1 IMP:P=1 IMP:E=1 $lead
  18   252  -11.35 -101 IMP:N=1 IMP:P=1 IMP:E=1 $lead
  20   256   -0.93 -103 IMP:N=1 IMP:P=1 IMP:E=1
  21   256   -0.93 -104 IMP:N=1 IMP:P=1 IMP:E=1
  22   256   -0.93 -105 IMP:N=1 IMP:P=1 IMP:E=1
  23   256   -0.93 -106 IMP:N=1 IMP:P=1 IMP:E=1
  25   256   -0.93 -107 IMP:N=1 IMP:P=1 IMP:E=1
  26   256   -0.93 -108 IMP:N=1 IMP:P=1 IMP:E=1
  29    19   -1.85 -91 IMP:N=1 IMP:P=1 IMP:E=1 $phantom
 306   256   -0.93 -110 IMP:N=1 IMP:P=1 IMP:E=1
  35   524   -0.64 -116 IMP:N=1 IMP:P=1 IMP:E=1
  41   524   -0.64 -122 IMP:N=1 IMP:P=1 IMP:E=1
  42   252  -11.35 -123 IMP:N=1 IMP:P=1 IMP:E=1
  44   228   -2.35 -124 IMP:N=1 IMP:P=1 IMP:E=1
  53   256  -0.93 -127 IMP:N=1 IMP:P=1 IMP:E=1 $moderator brick added
  54   256  -0.93 -128 IMP:N=1 IMP:P=1 IMP:E=1 $moderator half brick
  55   256  -0.93 -129 IMP:N=1 IMP:P=1 IMP:E=1 $moderator half brick
  56   256  -0.93 -130 IMP:N=1 IMP:P=1 IMP:E=1
  57   256  -0.93 -131 IMP:N=1 IMP:P=1 IMP:E=1 $moderator main center peice
  58   256   -0.93 -132 IMP:N=1 IMP:P=1 IMP:E=1 $moderator underneath 1
  59   256   -0.93 -133 IMP:N=1 IMP:P=1 IMP:E=1 $moderator underneath 2
  60   256   -0.93 -134 IMP:N=1 IMP:P=1 IMP:E=1 $moderator back piece
  61   252  -11.35 -135 IMP:N=1 IMP:P=1 IMP:E=1 $lead around head
  62   252  -11.35 -136 IMP:N=1 IMP:P=1 IMP:E=1 $lead around head
  63   252  -11.35 -137 IMP:N=1 IMP:P=1 IMP:E=1 $lead around head
```

```
c    Aluminum cover - face
   1       rpp -20.3 20.3 -38.1 38.1 6.3325 6.65
c    square of moderator
   2       rpp -19.9824 19.9824 -6.2 33.8 2.5124 6.3324
c    moderator
   3       rpp -19.9824 -16.4774 -6.2 33.8 -6.052 2.5124
c    moderator
   4       rpp 16.4774 19.9824 -6.2 33.8 -6.052 2.5124
c    moderator
   5       rpp 10.4574 16.4774 -6.2 33.8 1.8774 2.5124
c    moderator
   6       rpp -16.4774 -10.4574 -6.2 33.8 1.8774 2.5124
c    outside of cylinder of moderator
   7       rcc 0 17.8 -6.052 0 0 8.5644 9.525
c    inside of cylinder of moderator
   8       rcc 0 17.8 -6.052 0 0 8.5644 8.67375
c    outside of aluminum cylinder, in contact with moderator
   9       rcc 0 17.8 0.5039 0 0 1.27 15.1765
c    inside of aluminum cylinder, in contact with moderator
  10       rcc 0 17.8 0.5039 0 0 1.27 12.7635
c    outside of aluminum cylinder (thinner), in contact with moderator
  11       rcc 0 17.8 -8.3861 0 0 8.89 13.9065
c    inside of aluminum cylinder (thinner), in contact with moderator
  12       rcc 0 17.8 -8.3861 0 0 8.89 12.7635
c    outside of aluminum cylinder (thicker)
  13       rcc 0 17.8 -30.2555 0 0 21.8694 15.1765
c    inside of aluminum cylinder (thicker)
  14       rcc 0 17.8 -28.3505 0 0 19.9644 12.7635
c    target:  copper/water mix
  15       rcc 0 17.8 2.5759 0 0 0.3175 1.905
c    target:  copper
  16       rcc 0 17.8 2.5124001 0 0 0.381 3.81
c    target:  titanium
  17       rcc 0 17.8 1.62339 0 0 0.889 2.2225
c    outside of aluminum skirt around target
  18       rcc 0 17.8 0.03589999 0 0 2.4765 6.2992
c    inside of aluminum skirt around target
  19       rcc 0 17.8 0.03589999 0 0 2.4765 2.2225001
c    Aluminum cover - top
  20       rpp -20.6175 20.6175 38.1 38.4175 -6.685 6.65
c    Aluminum cover - bottom
  21       rpp -20.6175 20.6172 -38.4175 -38.1 -6.685 6.65
c    Aluminum cover - side
c  22       rpp -20.6175 -20.3 -38.4175 38.4175 -6.685 6.65
  22       rpp -20.6175 -20.3 -38.1 38.1 -6.685 6.65
c    Aluminum cover - side
c  23       rpp 20.3 20.6175 -38.4175 38.4175 -6.685 6.65
  23       rpp 20.3 20.6175 -38.1 38.1 -6.685 6.65
c    Aluminum cover - backplate
c  24       rpp -20.6175 20.6175 -38.4175 38.4175 -7.002501 -6.685
  24       rpp -20.6175 20.6175 -38.1 38.1 -7.002501 -6.685
```

```
   25       rcc 0 17.8 -7.1 0 0 0.6 15.2
c    Cutout of backplate
c    25       rcc 0 17.8 -7.0025 0 0 0.3175 15.2
c    The world
  200       sph 0 0 0 500
c ************************************************************
c moderator
   90       rpp -20.3 20.3 -38.1 38.422 6.66 12.16
c phantom
   91       rcc 0 17.7235 17.796 0 0 1 4.25 $phantom 4.25 cm radius, 1 cm thick
c lead
  100       rpp -9.525 9.525 12.72 22.85 17.671 17.796
c lead
  101       rpp -9.525 9.525 12.597 12.719 12.17 22.33
c moderator
  103       rpp 9.5251 62.6175 12.597 38.42 12.17 25.77
c moderator
  104       rpp -74.3825 62.6175 -38.1 12.596 12.171 25.77
c moderator
  105       rpp -74.3825 62.6175 -38.1 38.42 25.771 44.745
c moderator
  106       rpp -74.3825 53.6175 44.02 75.02 -68.69 44.745
c moderator
  107       rpp -74.3825 9.5251 22.851 38.42 12.16 25.771
c moderator
  108       rpp -74.3825 -20.62 -79.376 38.42 -70.2555 12.159
c moderator
  110       rpp 20.6175 62.6175 -79.376 38.42 -70.2555 12.17
c southern pine wood
  116       rpp -74.3825 53.6175 42.42 44.02 -68.69 44.745
c southern pine wood
  122       rpp -74.3825 43.6175 75.02 76.62 -68.69 44.745
c stainless steel
  123       rpp -74.3825 43.6175 76.62 77.62 -68.69 44.745
c concrete
  124       rpp -150 150 -94.176 -79.376 -150 150
c moderator
  126       rpp -40.62 -20.3 12.596 22.851 12.17 25.77
c moderator brick
  127       rpp -9.5 9.5 12.72 22.809 12.17 17.67
c moderator brick
  128       rpp -19.01 -9.51 12.72 22.809 12.17 17.67
c moderator brick
  129       rpp -19.01 -9.53 12.72 22.809 17.671 25.77
c moderator brick
  130       rpp -74.3825 -19.03 12.72 22.809 12.17 25.77
c moderator in center
  131       rpp -20.62 20.6175 -79.376 -32.376 -70.255 -7.002501
c moderator underneath 1
  132       rpp -20.62 20.6175 -79.376 -38.5 -7.002501 12.16
c moderator underneath 2
```

```
 133       rpp -74.3825 62.6175 -79.376 -38.1 12.2 44.745
c moderator back piece
 134       rpp -71.3825 50.61 -79.37 46.624 44.745 74.745
 135       rpp -15.4765 -15.1765 2.6235 32.9765 -29.8861 -8.3861 $lead around head
 136       rpp -15.1765 15.1765 32.9765 33.2765 -29.8861 -8.3861 $lead around head
 137       rpp 15.1765 15.4765 2.6235 32.9765 -29.8861 -8.3861 $lead around head

mode  n p e
m25   25055.70c          -1  $ Mn with density 7.21
m48   20048.70c          -1  $ Ca with density 1.54g/cm3
m10   1001.70c       -0.022804  $0ppm
     7014.70c      -0.005588 16032.70c      -0.18111
     11023.70c      -0.007133 8016.70c     -0.555429 20040.70c    -0.222512
     17035.70c      -0.003106 12024.70c  -0.002317
m11   1001.70c       -0.0228  $0.5ppm (6.64356E-09)
     7014.70c      -0.00559 16032.70c      -0.18111 25055.70c    -5.6e-07
     11023.70c      -0.00713 8016.70c     -0.55543 20040.70c    -0.22251
     17035.70c      -0.00311 12024.70c  -0.00232
m12   1001.70c       -0.0228  $1ppm (1.3291E-08)
     7014.70c      -0.00559 16032.70c      -0.18111 25055.70c    -1.1e-06
     11023.70c      -0.00713 8016.70c     -0.55543 20040.70c    -0.22251
     17035.70c      -0.00311 12024.70c  -0.00232
m13   1001.70c       -0.0228  $2ppm (2.65889E-08)
     7014.70c      -0.00559 16032.70c      -0.18111 25055.70c    -2.2e-06
     11023.70c      -0.00713 8016.70c     -0.55543 20040.70c    -0.22251
     17035.70c      -0.00311 12024.70c  -0.00232
m14   1001.70c       -0.0228  $5ppm (6.64549E-08)
     7014.70c      -0.00559 16032.70c      -0.18111 25055.70c    -5.6e-06
     11023.70c      -0.00713 8016.70c     -0.55542 20040.70c    -0.22251
     17035.70c      -0.00311 12024.70c  -0.00232
m15   1001.70c       -0.0228  $10ppm (1.32867E-07)
     7014.70c      -0.00559 16032.70c      -0.18111 25055.70c    -1.1e-05
     11023.70c      -0.00713 8016.70c     -0.55541 20040.70c    -0.22251
     17035.70c      -0.00311 12024.70c  -0.00232
m16   1001.70c       -0.0228  $15ppm (1.99367E-07)
     7014.70c      -0.00559 16032.70c      -0.18111 25055.70c    -1.7e-05
     11023.70c      -0.00713 8016.70c     -0.5554 20040.70c    -0.2225
     17035.70c      -0.00311 12024.70c  -0.00232
m17   1001.70c       -0.0228  $20ppm (2.65822E-07)
     7014.70c      -0.00559 16032.70c      -0.18111 25055.70c    -2.2e-05
     11023.70c      -0.00713 8016.70c     -0.55539 20040.70c    -0.2225
     17035.70c      -0.00311 12024.70c  -0.00232
m18   1001.70c       -0.0228  $30ppm (3.98732E-07)
     7014.70c      -0.0056 16032.70c      -0.18109 25055.70c    -3.3e-05
     11023.70c      -0.00713 8016.70c     -0.55537 20040.70c    -0.22249
     17035.70c      -0.00311 12024.70c  -0.00232
m19   1001.70c       -0.0228  $40ppm (5.31489E-07)
     7014.70c      -0.0056 16032.70c      -0.18108 25055.70c    -4.5e-05
     11023.70c      -0.00713 8016.70c     -0.55535 20040.70c    -0.22248
     17035.70c      -0.00311 12024.70c  -0.00232
m208  13027.70c          -1  $aluminum
```

```
m111  5010.70c        -0.199  $boron-10
     5011.70c        -0.801
m209  29063.70c       0.6915  $natural copper
     29065.70c       0.3085
m317  1001.70c         0.333  $copper and water mixture
     8016.70c         0.167 29063.70c       0.34575 29065.70c       0.15425
m236  6000.70c           -1  $graphite
c  Titanium, changed 22050 from 0.056332 to 0.05633
m498  22046.70c     -0.076779  $Titanium density 4.506 g/cm3
     22047.70c     -0.071584 22048.70c     -0.739078 22049.70c     -0.056228
     22050.70c     -0.056331
m1    1001.70c      -0.101172  $soft tissue ICRU 4 component density=1.0 g/c
     6000.70c        -0.111 7014.70c    -0.02790536 7015.70c    -9.464e-005
     8016.70c     -0.7616075 8017.70c   -0.0002205451
c MODERATORS
m256  1001.70c      -0.143711  $polyethylene
     6000.70c      -0.856289
m333  1001.70c     -0.1005977  $30% by weight borated polyethylene p=1.19 g/cm3
     6000.70c     -0.5994023 5010.70c        -0.0588 5011.70c        -0.2412
m434  1001.70c      -0.148605  $paraffin wax p=0.93
     6000.70c      -0.851395
m444  1001.70c     -0.1365255  $5% by weight borated polyethylene p=1.08 g/cm3
     6000.70c     -0.8134745 5010.70c        -0.0098 5011.70c        -0.0402
m228  1001.70c      -0.005558  $concrete (ordinary with ENDF-VI), 2.35
     8016.70c      -0.498076 11023.70c     -0.017101 12024.70c     -0.001999
     12025.70c     -0.000264 12026.70c     -0.000302 13027.70c     -0.045746
     14028.70c     -0.289486 14029.70c     -0.015181 14030.70c     -0.010425
     16032.70c     -0.001216 16033.70c      -1e-005 16034.70c     -5.7e-005
     19039.70c      -0.01788 19040.70c       -2e-006 19041.70c     -0.001357
     20040.70c      -0.08019 20042.70c     -0.000562 20043.70c      -0.00012
     20044.70c      -0.00188 20046.70c       -4e-006 20048.70c     -0.000186
     26054.70c     -0.000707 26056.70c      -0.01139 26057.70c     -0.000265
     26058.70c     -3.6e-005
c end MODERATORS
m252  82206.70c     -0.242902  $lead density = 11.35 g/cm3
     82207.70c     -0.223827 82208.70c      -0.53327
m204  7014.70c     -0.7528855  $air (US S. Atm at sea level)
     7015.70c   -0.002750515 8016.70c      -0.231387 8017.70c   -8.79605e-005
     18036.70c     -3.9e-005 18038.70c       -8e-006 18040.70c     -0.012842
m999  7014.70c     -0.7528855  $air (1e-4 torr pressure)
     7015.70c   -0.002750515 8016.70c      -0.231475 8017.70c   -8.79605e-005
     18036.70c     -3.9e-005 18038.70c       -8e-006 18040.70c     -0.012842
c    Steel
m1000  6000.01p       -0.00075  $Steel
      7014.70c       -0.00125 14000.60c        -0.005 15031.70c       -0.0003
      16000.62c      -0.00015 24000.42c         -0.18 25055.70c       -0.0875
      26000.55c      -0.67505
m492  6000.70c         -0.002  $Steel, HT9 Stainless,
     14028.70c     -0.003675 14029.70c     -0.000193 14030.70c     -0.000132
     15031.70c       -0.0003 16032.70c     -0.000189 16033.70c       -2e-006
     16034.70c       -9e-006 23000.70c        -0.003 24050.70c     -0.004799
```

```
     24052.70c     -0.096256 24053.70c     -0.011123 24054.70c     -0.002821
     25055.70c       -0.006 26054.70c     -0.048409 26056.70c     -0.780435
     26057.70c     -0.018188 26058.70c     -0.002468 28058.70c      -0.00337
     28060.70c     -0.001333 28061.70c     -5.9e-005 28062.70c     -0.000189
     28064.70c      -5e-005 42092.70c     -0.001422 42094.70c     -0.000905
     42095.70c     -0.001575 42096.70c     -0.001668 42097.70c     -0.000965
     42098.70c     -0.002463 42100.70c     -0.001003 74183.70c       -0.005
m524  1001.70c      -0.057889  $Southern Pine Wood, -.64
     6000.70c      -0.482667 8016.70c      -0.459444
mt208 al27.12t
mt236 grph.10t
mt256 poly.10t
phys:n 20
phys:p 15 0 0
phys:e 20
c act fission=n nonfiss=none dn=prompt dg=mg thresh=1.0 nap=1000
sdef erg=fdir=d3 par=n pos=0 17.8 1.62338 axs=0 0 1 ext=0 &
vec=0 0 1 dir=d2 ara=10 rad=2.0
c ***************************************************************************
c *  Reaction kinematics valid for deuteron kinetic energy = 110 keV *
c *  Reaction kinematics calculated with DROSG-2000                 *
c ***************************************************************************
si2 L 1 0.999912028 0.999652741 0.999215271 0.998601995 0.997824541 &
0.996862316 0.995740805 0.994430298 0.992944828 0.991307631 0.989475339 &
0.987468954 0.985318642 0.98296744 0.980477623 0.977783237 0.974916815 &
0.971919946 0.968713242 0.965336099 0.961836881 0.958122893 0.954292506 &
0.950244253 0.94602881 0.941705652 0.937160258 0.932449975 0.927640831 &
0.922605429 0.917407699 0.912120116 0.906602609 0.90100132 0.895167868 &
0.889176915 0.883111416 0.876810691 0.870355696 0.863835505 0.857077397 &
0.85026037 0.843203841 0.835998956 0.828744666 0.821248805 0.81360845 &
0.805928282 0.798004853 0.789941019 0.781847028 0.773508466 0.765146196 &
0.756538698 0.74779809 0.739043499 0.730043012 0.720914077 0.711780905 &
0.702401554 0.693024454 0.683401201 0.673657707 0.663926213 0.653948927 &
0.643856583 0.633785968 0.623470308 0.613182832 0.602651022 0.592013179 &
0.581413184 0.570570241 0.55962691 0.548731033 0.537593975 0.52636233 &
0.515187671 0.503773977 0.49242356 0.480835744 0.469163327 0.457563562 &
0.445729165 0.433816346 0.421985437 0.409923034 0.397948631 0.385745023 &
0.373473545 0.361299106 0.348899199 0.336437906 0.324082536 0.311505793 &
0.298874241 0.286357333 0.273623491 0.261009993 0.248182704 0.235311749 &
0.22256955 0.209618563 0.196630695 0.183779793 0.170725434 0.157813385 &
0.144701602 0.131564359 0.118577272 0.105396307 0.092196799 0.079155056 &
0.065925598 0.05285883 0.03960861 0.026351421 0.013264113 6.12574e-17 &
-0.013264113 -0.026351421 -0.03960861 -0.05285883 -0.065925598 &
-0.079155056 -0.092196799 -0.105396307 -0.118577272 -0.131564359 &
-0.144701602 -0.157813385 -0.170725434 -0.183779793 -0.196630695 &
-0.209618563 -0.22256955 -0.235311749 -0.248182704 -0.261009993 &
-0.273623491 -0.286357333 -0.298874241 -0.311505793 -0.324082536 &
-0.336437906 -0.348899199 -0.361299106 -0.373473545 -0.385745023 &
-0.397948631 -0.409923034 -0.421985437 -0.433816346 -0.445729165 &
-0.457563562 -0.469163327 -0.480835744 -0.49242356 -0.503773977 &
-0.515187671 -0.52636233 -0.537593975 -0.548731033 -0.55962691 &
```

-0.570570241 -0.581413184 -0.592013179 -0.602651022 -0.613182832 &
-0.623470308 -0.633785968 -0.643856583 -0.653948927 -0.663926213 &
-0.673657707 -0.683401201 -0.693024454 -0.702401554 -0.711780905 &
-0.720914077 -0.730043012 -0.739043499 -0.74779809 -0.756538698 &
-0.765146196 -0.773508466 -0.781847028 -0.789941019 -0.798004853 &
-0.805928282 -0.81360845 -0.821248805 -0.828744666 -0.835998956 &
-0.843203841 -0.85026037 -0.857077397 -0.863835505 -0.870355696 &
-0.876810691 -0.883111416 -0.889176915 -0.895167868 -0.90100132 &
-0.906602609 -0.912120116 -0.917407699 -0.922605429 -0.927640831 &
-0.932449975 -0.937160258 -0.941705652 -0.94602881 -0.950244253 &
-0.954292506 -0.958122893 -0.961836881 -0.965336099 -0.968713242 &
-0.971919946 -0.974916815 -0.977783237 -0.980477623 -0.98296744 &
-0.985318642 -0.987468954 -0.989475339 -0.991307631 -0.992944828 &
-0.994430298 -0.995740805 -0.996862316 -0.997824541 -0.998601995 &
-0.999215271 -0.999652741 -0.999912028 -1
sp2 0.006420429 0.006420429 0.00641793 0.006412932 0.006407933 &
0.006402935 0.006392938 0.006382942 0.006372945 0.006360449 &
0.006345454 0.006330458 0.006312964 0.00629547 0.006275476 &
0.006255483 0.00623299 0.006207998 0.006183006 0.006158014 &
0.006130523 0.006100533 0.006070542 0.006040552 0.006008062 &
0.005975573 0.005940584 0.005905595 0.005868108 0.00583062 &
0.005793132 0.005753145 0.005715657 0.00567317 0.005633183 &
0.005590697 0.005548211 0.005503225 0.00545824 0.005415753 &
0.005368269 0.005323283 0.005278298 0.005230813 0.005183328 &
0.005135844 0.005088359 0.005040874 0.00499339 0.004945905 &
0.004895921 0.004848436 0.004798452 0.004750968 0.004703483 &
0.004653499 0.004606015 0.00455853 0.004508546 0.004461061 &
0.004413577 0.004366092 0.004318607 0.004273622 0.004226137 &
0.004181152 0.004136166 0.004091181 0.004046195 0.00400121 &
0.003958723 0.003916237 0.003873751 0.003831264 0.003791277 &
0.00375129 0.003711303 0.003671316 0.003633828 0.00359634 &
0.003558852 0.003523864 0.003488875 0.003453886 0.003421397 &
0.003388907 0.003356418 0.003326427 0.003296437 0.003266447 &
0.003238955 0.003211464 0.003183973 0.003158981 0.003133989 &
0.003111497 0.003089004 0.003066511 0.003046517 0.003026524 &
0.00300903 0.002991535 0.002974041 0.002959046 0.002944051 &
0.002929055 0.002916559 0.002904063 0.002894067 0.00288407 &
0.002874073 0.002866576 0.002859078 0.00285158 0.002846582 &
0.002841584 0.002839084 0.002836585 0.002834086 0.002831587 &
0.002831587 0.002834086 0.002834086 0.002836585 0.002841584 &
0.002844083 0.002849081 0.00285408 0.002861577 0.002869075 &
0.002876572 0.002886569 0.002894067 0.002904063 0.002916559 &
0.002926556 0.002939052 0.002951548 0.002966543 0.002979039 &
0.002994034 0.00300903 0.003026524 0.003041519 0.003059013 &
0.003076508 0.003094002 0.003113996 0.00313149 0.003151484 &
0.003171477 0.003191471 0.003213963 0.003233957 0.00325645 &
0.003276443 0.003298936 0.003321429 0.003343922 0.003368914 &
0.003391406 0.003413899 0.003438891 0.003463883 0.003486376 &
0.003511368 0.00353636 0.003561351 0.003586343 0.003611335 &
0.003636327 0.003661319 0.003686311 0.003711303 0.003736295 &
0.003761287 0.003786279 0.00381377 0.003838762 0.003863754 &

```
0.003888746 0.003913738 0.00393873 0.003963722 0.003986214 &
0.004011206 0.004036198 0.00406119 0.004083683 0.004108675 &
0.004131168 0.00415366 0.004176153 0.004201145 0.004223638 &
0.004243631 0.004266124 0.004288617 0.00430861 0.004328604 &
0.004351097 0.00437109 0.004388585 0.004408578 0.004428572 &
0.004446066 0.004463561 0.004481055 0.004498549 0.004516044 &
0.004531039 0.004548533 0.004563528 0.004576024 0.004591019 &
0.004606015 0.004618511 0.004631007 0.004643502 0.004653499 &
0.004665995 0.004675992 0.004685989 0.004695986 0.004703483 &
0.004710981 0.004718478 0.004725976 0.004733473 0.004738472 &
0.00474347 0.004748469 0.004750968 0.004755966 0.004758465 &
0.004760965 0.004760965 0.004763464 0.004763464
ds3 L 2.87434 2.8743 2.87419 2.87401 2.87374 2.87341 2.873 &
2.87252 2.87196 2.87133 2.87062 2.86984 2.86899 2.86806 &
2.86706 2.86599 2.86485 2.86363 2.86234 2.86098 2.85955 &
2.85805 2.85648 2.85483 2.85312 2.85134 2.84949 2.84757 &
2.84558 2.84353 2.8414 2.83922 2.83696 2.83464 2.83226 &
2.82981 2.8273 2.82472 2.82209 2.81939 2.81663 2.8138 &
2.81092 2.80798 2.80499 2.80193 2.79882 2.79565 2.79242 &
2.78914 2.78581 2.78242 2.77898 2.77549 2.77195 2.76836 &
2.76472 2.76103 2.75729 2.75351 2.74968 2.74581 2.74189 &
2.73793 2.73392 2.72988 2.72579 2.72167 2.71751 2.71331 &
2.70907 2.70479 2.70048 2.69614 2.69177 2.68736 2.68292 &
2.67845 2.67395 2.66942 2.66487 2.66029 2.65568 2.65105 &
2.6464 2.64172 2.63702 2.6323 2.62756 2.62281 2.61803 &
2.61324 2.60843 2.60361 2.59877 2.59392 2.58906 2.58419 &
2.57931 2.57441 2.56951 2.56461 2.55969 2.55477 2.54985 &
2.54492 2.53999 2.53506 2.53013 2.52519 2.52026 2.51533 &
2.51041 2.50548 2.50056 2.49565 2.49074 2.48584 2.48095 &
2.47607 2.47119 2.46633 2.46148 2.45664 2.45181 2.447 &
2.4422 2.43741 2.43265 2.42789 2.42316 2.41845 2.41375 &
2.40908 2.40442 2.39979 2.39518 2.39059 2.38602 2.38148 &
2.37696 2.37247 2.36801 2.36357 2.35916 2.35478 2.35043 &
2.3461 2.34181 2.33755 2.33331 2.32911 2.32495 2.32081 &
2.31671 2.31264 2.30861 2.30462 2.30066 2.29673 2.29284 &
2.28899 2.28518 2.28141 2.27767 2.27398 2.27032 2.2667 &
2.26313 2.25959 2.2561 2.25265 2.24924 2.24588 2.24256 &
2.23928 2.23604 2.23285 2.22971 2.22661 2.22356 2.22055 &
2.21759 2.21467 2.2118 2.20898 2.20621 2.20348 2.2008 &
2.19817 2.19559 2.19306 2.19058 2.18814 2.18576 2.18343 &
2.18114 2.17891 2.17673 2.1746 2.17252 2.17049 2.16852 &
2.16659 2.16472 2.1629 2.16113 2.15942 2.15776 2.15615 &
2.15459 2.15309 2.15164 2.15024 2.1489 2.14761 2.14638 &
2.14519 2.14407 2.143 2.14198 2.14101 2.14011 2.13925 &
2.13845 2.13771 2.13702 2.13638 2.1358 2.13528 2.13481 &
2.13439 2.13403 2.13373 2.13348 2.13329 2.13315 2.13307 2.13304
nps 1e6
c  ******************************************
c  Neutron Flux in the Phantom Divided into Energy Bins
c  ******************************************
f4:n 29
```

```
e4    1.0e-10 1.50e-10 2.0e-10 2.5e-10
      1.0e-9  1.5e-9    2.0e-9  2.5e-9 8i
      1.0e-8 8i 1.5e-8 5i   2.0e-8 8i 2.5e-8  8i
      1.0e-7 8i 1.5e-7  8i  2.0e-7 3i 2.5e-7 10i
      1.0e-6 10i 1.5e-6 10i   2.0e-6 10i 2.5e-6 15i
      1.0e-5 10i 1.5e-5  10i  2.0e-5 10i 2.5e-5 15i
      1.0e-4 10i 1.5e-4  10i  2.0e-4 10i 2.5e-4  15i
      1.0e-3 5i 1.5e-3 10i   2.0e-3 10i 2.5e-3  15i
      1.0e-2 10i 1.5e-2 10i   2.0e-2 10i 2.5e-2 15i
      1.0e-1 10i 1.5e-1 10i   2.0e-1 10i 2.5e-1 15i 2.75e-1 20i
      1.0e+00 8i 1.5e+00 8i 2.0e+00 5i 2.5e+00 10i 3e+00
c  ******************************************
c Mn activation tally
c  ******************************************
f14:n 29
fm14 5.31489E-07 25 102
sd14 1
c  ******************************************
c  Ca activation tally
c  ******************************************
f24:n 29
fm24 5.67597E-06 48 102
sd24 1
c  ******************************************
c  ICRP 74 FLUX TO DOSE CONVERSION FACTORS(mrem/h-per source particle)
c  ******************************************
f34:n 29
de34  1.00E-09 1.00E-08 2.53E-08 1.00E-07 2.00E-07 5.00E-07 1.00E-06 2.00E-06
      5.00e-06 1.00E-05 2.00E-05 5.00E-05 1.00E-04 2.00E-04 5.00E-04 1.00E-03
      0.002 0.005 0.01 0.02 0.03 0.05 0.07 0.1 0.15 0.2 0.3 0.5 0.7 0.9 1 1.2
      2 3
df34  2.3760E-03 3.2400E-03 3.8160E-03 4.6440E-03 4.8600E-03 4.8960E-03
      4.7880e-03 4.6440E-03 4.3200E-03 4.0680E-03 3.8160E-03 3.5640E-03
      3.3840e-03 3.2040E-03 2.9880E-03 2.8440E-03 2.7720E-03 2.8800E-03
      3.7800e-03 5.9760E-03 8.5320E-03 1.4796E-02 2.1600E-02 3.1680E-02
      4.7520e-02 6.1200E-02 8.3880E-02 1.1592E-01 1.3500E-01 1.4400E-01
      1.4976e-01 1.5300E-01 1.5120E-01 1.4832E-01
c  ******************************************
c  MCNP Dose Function Method of Neutron Dose Calculation Output[Sv/h/(source neutron/s)]
c  ******************************************
f44:n 29
df44 IU 2 IC 20
c  ******************************************
c  MCNP Dose Function Method of Photon Dose Calculation Output[Sv/h/(source neutron/s)]
c  ******************************************
f54:p 29
df54 IU 2 IC 10
print 110
```

N-Type HPGe Detector MCNP Input File

```
   MCNPX Visual Editor Version X_24E
c     Created on: Tuesday, August 22, 2017 at 11:04
    1     1   -5.32 -2 4 -3 (32 :11 :-33 )#17 #15 #14 #40 #41  $Ge
    2   208 -2.6989 18 -6 11 -46 102  $Al
    3   208 -2.6989 102 45 -46 -18
    5   458   -1.38 5 -4 -46 -102  $mylar
  500   208 -2.6989 -5 500 -46
    6   208 -2.6989 47 -48 -23 12
    7     0        -45 102 -18 (52 :3 )
    8     0        -23 -47 12 (6 :46 :-500 )
    9     0        18 -6 -11
   10   204 -0.001225 -1 (-13 :23 :48 :55 )#19 #20 #40 #41 #38 #39 #43 #44 #45 &
#46 #47 #48 #49 #50 #51 #52
   11     0        1
   14     0        -49 -3 (-50 :51 )
   15     0        -52 102 53 -34 (36 :-35 :38 :-37 :41 :-40 :43 :-44 )
   16   208 -2.6699 -12 13 -48
   17     1   -5.32 -3 -11 (-32 :19 )#14  $dead layer, inner
   18     1   -5.32 2 -52 (-33 :-3 )#40 #15 #8 #16 #11 $dead layer, outer crysta
          #10 #500 #5 #38 #39 #44 #50
   19   208 -2.6989 23 -55 -56 (57 :54 :-58 )86
   20   204 -0.001225 58 -54 -57
   38     5   -2.23 -97 -98 86 (99 :100 :105 ) $Glass portion of Vial Source
   39     6  -1.033 -99 -100 -105  $ Solution portion of Vial Source
   40     1   -5.32 (-53 33 )(36 :-35 :38 :-37 :41 :-40 :43 :-44 )-34 -52 4 $40 is the outer dead layer in the
rounded region
   41     1   -5.32 102 -52 -4 (-4 :-53 )#40 #15  $ dl on the top of the detec
   43   252   -11.35 -107 $bottom blocks of lead
   44   252   -11.35 -108 $front block
   45   252   -11.35 -109 $LEft side block
   46   252   -11.35 -110 $Right Side block
   47   252   -11.35 -111 $Right Side block
   48   252   -11.35 -112 $LEft outer side block
   49   252   -11.35 -113 $RIght outer side brick
   50   252   -11.35 -114 $front outer brick
   51   252   -11.35 -115 $back block
   52   252   -11.34 -116 $topmost block

    1       so 100  $world
    2       cx 3.775  $crystal
    3       px 4.88  $crystal
    4       px -4.24  $crystal
    5       px -4.273  $Al/Mylar window
  500         px -4.276
    6       px 8.71  $Cup length
   11        cx 0.57  $inside cylinder
   12        px -4.676  $Gap
   13        px -4.826  $Al
   18        px 8.41  $Al
   19        px -2.92
```

```
 23       px 14.357  $fictional stop
 32        s -2.94 0 0 0.57
 33       tx -3.41 0 0 2.975 0.83 0.83
 34       px -3.41
 35       pz -2.975
 36       pz 2.975
 37       py -2.975
 38       py 2.975
 40        p 0 0.70710678859302 0.70710678859302 -2.99
 41        p 0 0.70710681270686 0.70710681270686 2.99
 43        p 0 0.70710678859302 -0.70710678859302 3
 44        p 0 0.70710678859302 -0.70710678859302 -3
 45       cx 4.2
 46       cx 4.28
 47       cx 4.65
 48       cx 4.8
 49       cx 0.5
 50        s -2.94 0 0 0.5
 51       px -2.85
 52       cx 3.77503
 53       tx -3.41 0 0 2.975 0.855 0.855
 54       cx 4.9
 55       cx 5
 56       px 25.957
 57       px 25.857
 58       px 14.457
 77       py -5.8
 78       py 15.8
 80       px 4.793
 81       px 14.793
 86       pz -5
 97      c/z -5.944 0 1  $-9.793 0 1
 98       pz 1.5
 99      c/z -5.944 0 0.95  $$-9.793 0 1
100       pz 0.3
101       pz -5.4
102       px -4.27
103       cx 4  $phantom
104       px -5.793
105       k/z -5.944 0 -4.7 0.85 1
106       px -7.2
107       rpp -15.103 56.46 -10.16 10.16 -10.08 -5 $Bottom blocks of lead
108       rpp -15.103 -10.023 -10.16 10.16 -5 5.16 $Front brick 1
109       rpp -10.023 30.617 5.08 10.16 -5 5.16 $Left side brick
110       rpp -10.023 30.617 -10.16 -5.08 -5 5.16 $ Right side brick
111       rpp -15.103 25.537 -10.16 10.16 5.16 10.24 $top brick layer
112       rpp -15.103 25.537 10.16 15.24 -5 5.16 $LEft outer side brick
113       rpp -15.103 25.537 -15.24 -10.16 -5 5.16 $RIght outer side brick
114       rpp -25.263 -15.103 -10.16 10.16 -10.08 10.24 $Front outer block
115       rpp 25.537 30.617 -10.16 10.16 5.16 15.32 $Back block
116       rpp -20.183 0.137 -10.16 10.16 10.24 15.32 $topmost block
```

```
mode  p
m204  7000.        -0.755636  $air (US S. Atm at sea level)
     8000.        -0.231475 18000.        -3.9e-005 18000.         -8e-006
     18000.       -0.012842
m208  13000.             -1  $aluminum
m458  1000.         -0.04196  $Polyeth Terephthalate (Mylar),
     6000.        -0.625016 8000.        -0.333024
c    Germanium
m1    32000.             -1  $Germanium
c    lithium
m21   3000.            -0.1  $lithium
     32000.           -0.9
c    boron
m31   5000.            -0.1  $boron
     32000.           -0.9
m252  82000.             -1  $lead
m4    1000.        -0.059642  $wood, from pnnl, -0.64
     6000.        -0.497018 7000.         -0.00497 8000.         -0.427435
     12000.       -0.001988 16000.         -0.00497 19000.        -0.001988
     20000.       -0.001988
c Pyrex Glass, 2.23
m5    5000.        -0.040064
     8000.        -0.539562 11000.        -0.028191 13000.        -0.011644
     14000.        -0.37722 19000.        -0.003321
c HCl, 1.19 g/cm3
m6    1000.       -0.02764674
     17000.       -0.9722984
m300  1001.       -0.02132674  $Phantom, 10K
     7014.       -0.01753001 11023.       -0.01791878 20040.       -0.1930784
     16032.       -0.1636846 8016.        -0.5241159 17035.       -0.01673809
     12024.      -0.04560757
m301  1001.       -0.02238885  $Phantom, 4K
     7014.       -0.01840304 11023.       -0.01881117 20040.        -0.202694
     16032.       -0.1660356 8016.        -0.5349441 17035.       -0.01757168
     12024.      -0.01915157
m302  1001.        -0.0227668  $Phantom, 2K
     7014.        -0.0187137 11023.       -0.01912872 20040.       -0.2061157
     16032.       -0.1668721 8016.        -0.5387973 17035.       -0.0178683
     12024.      -0.00973743
m303  1001.       -0.02296059  $Phantom, 1K
     7014.       -0.01887299 11023.       -0.01929155 20040.       -0.2078702
     16032.       -0.1673011 8016.         -0.540773 17035.       -0.0180204
     12024.      -0.004910159
m304  1001.       -0.02305873  $Phantom, 500
     7014.       -0.01895366 11023.       -0.01937401 20040.       -0.2087587
     16032.       -0.1675183 8016.        -0.5417736 17035.       -0.01809742
     12024.      -0.002465573
m305  1001.       -0.02313785  $Phantom, 100
     7014.        -0.0190187 11023.       -0.01944048 20040.        -0.209475
     16032.       -0.1676935 8016.        -0.5425802 17035.       -0.01815952
     12024.      -0.000494807
```

```
m306  1001.       -0.02314778  $Phantom, 50
     7014.       -0.01902686 11023.      -0.01944882 20040.       -0.2095648
     16032.       -0.1677155 8016.        -0.5426814 17035.      -0.01816731
     12024.     -0.000247509
m307  1001.       -0.02315772  $Phantom, 0
     7014.       -0.01903502 11023.      -0.01945717 20040.       -0.2096548
     16032.       -0.1677375 8016.        -0.5427827 17035.      -0.01817511
imp:p   1 9r        0           1 20r        $ 1, 44
imp:e   1 9r        0           1 20r        $ 1, 44
c PTRAC file=asc max=1e7 nps=1,1e8 type=p event=src,col cell=1 write=all
nps 1e9
f8:p 1
e8 0 1e-5 1e-3 16383i 3.40196
c e1 0 1e-5 1e-3 16383i 3.40196
c ft8 geb -0.0007802 0.0606 1504 $ levenberg marquardt
c ft8 geb 0.0008644 0.0008052  0.7319 $ trust region
c ft1 geb 0.0008644 0.0008052  0.7319 $ trust region
sdef pos= -5.944 0 -4.7  rad=d1 ext=d2  erg=d3 axs=0 0 1 cel=39
si1 0 0.95
si2 0 5
si3 L 0.088 0.122 0.159 0.392 0.514 0.662 0.898 1.173 1.333 1.836
sp3 D 1.2357E-02 4.0631E-03 2.4135E-04 4.9013E-04 9.6203E-6
     1.9682E-01 9.244E-04 2.1023E-1 2.1023E-1 9.7756E-04
prdmp 2j 1
```

APPENDIX B. CADAVER BONE SAMPLE IMAGES

Figure A.1. Sample #27898

Figure A.2. Sample #225457

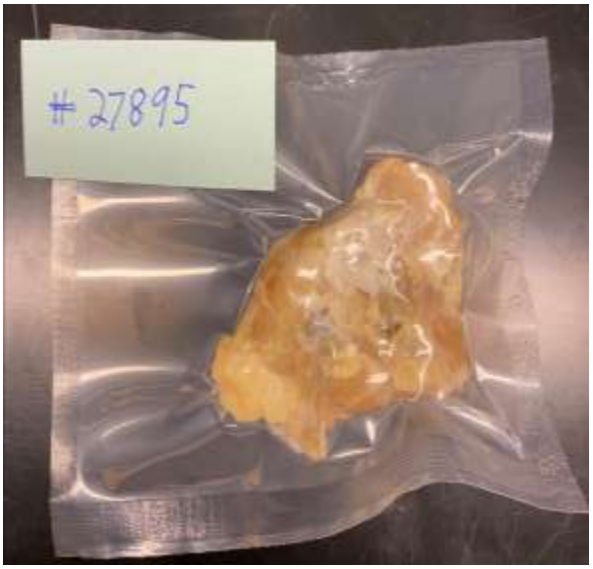

Figure A.3. Sample #27895

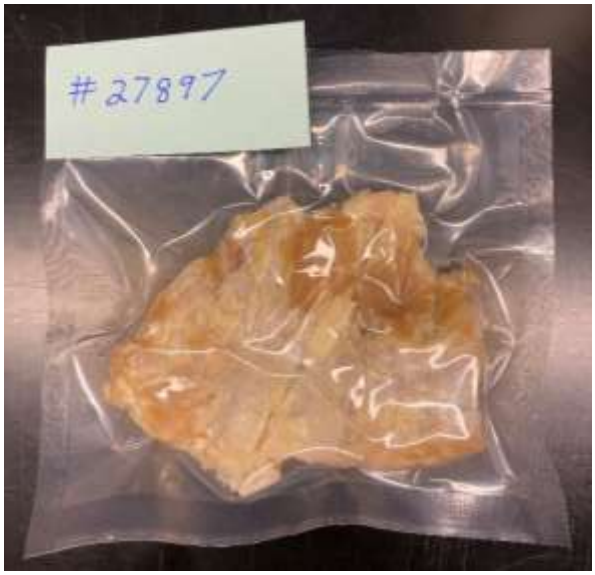

Figure A.4. Sample #27897

Figure A.5. Sample #29697

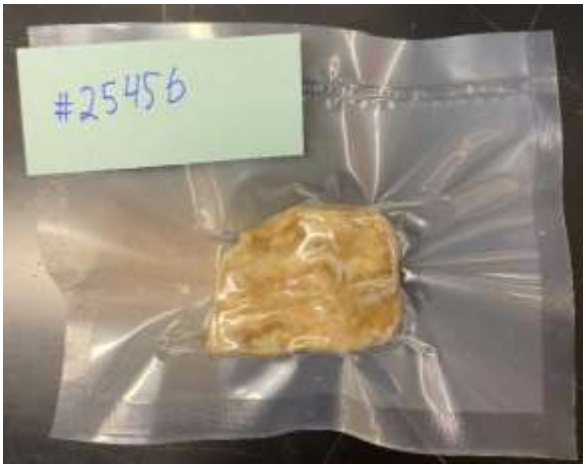

Figure A.6. Sample #25456

Figure A.7. Sample #29696

Figure A.8. Sample #27896

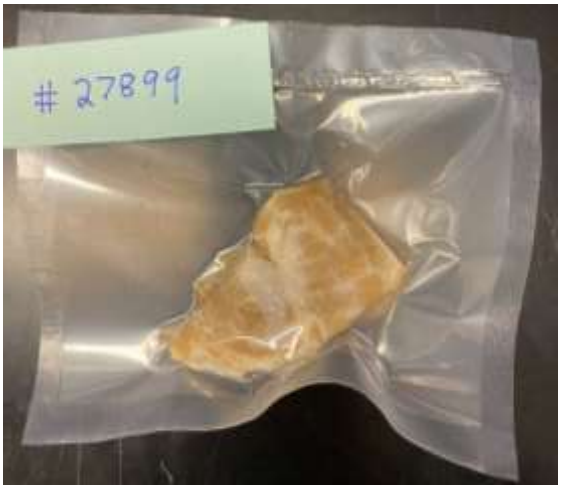

Figure A.9. Sample #27899

Figure A.10. Sample #29699

Figure A.11. Sample #29698

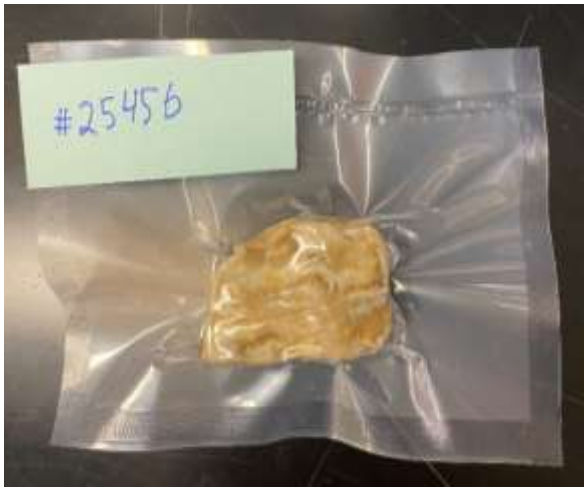

Figure A.12. Sample #25456

REFERENCES

[1] Kehl-Fie, T. E. & Skaar, E. P. Nutritional immunity beyond iron: a role for manganese and zinc. *Current Opinion in Chemical Biology* vol. 14 (2010).

[2] Jeanne H. Freeland-Graves. Manganese: An Essential Nutrient for Humans. *Nutrition Today* **November/December**, (1998).

[3] Chen, P., Bornhorst, J. & Aschner, M. Manganese metabolism in humans. *Frontiers in Bioscience - Landmark* **23**, (2018).

[4] Crossgrove, J. & Zheng, W. Manganese toxicity upon overexposure. *NMR in Biomedicine* vol. 17 (2004).

[5] National Institute of Health. Biomarkers. *Health & Education*.

[6] Zheng, W., Fu, S. X., Dydak, U. & Cowan, D. M. Biomarkers of manganese intoxication. *NeuroToxicology* vol. 32 (2011).

[7] Conley, T. E. , C. R. J. P. N. D. T. J. S. G. R. G. L. S. F. R. O. R. D. R. S. Bone manganese is a sensitive biomarker of ongoing elevated manganese exposure, but does not accumulate across the lifespan. *Environmental Research* **204**, (2022).

[8] Glascock, M. D. An overview of neutron activation analysis. *Malaysian Magazine of Physics, Science and Ideas* **1**, (1996).

[9] L'Annunziata, M. F. *Handbook of Radioactivity Analysis*. *Handbook of Radioactivity Analysis* (2003). doi:10.1016/B978-0-12-436603-9.X5000-5.

[10] IAEA. Atlas of Neutron Capture Cross Sections.

[11] IAEA. Live Chart of Nuclides.

[12] Radovic, L. R. & Schobert, H. H. Energy and Fuels in Society: Analysis of Bills and Media Reports. in *McGraw-Hill* (1992).

[13] Werner, C. J. *et al.* MCNP6.2 Release Notes. *Report LA-UR-18-20808* (2018).

[14] Douglas Harper. Online Etymology Dictionary .

[15] Nuclear Regulatory Commison. *10 CFR Part 20 Standards for Protection Against Radiation*. (1991).

[16] Adelphi Technologies, Inc. *Neutron Generator Models DD-109M & DD110M Operation Manual*. (2016).

[17] Soo Hyun Byun. Radioisotopes and Radiation Methodology: Chapter 8 Hyper-Pure Germanium Detector .

[18] Jin, Y., Gardner, R. P. & Verghese, K. A semi-empirical model for the gamma-ray response function of germanium detectors based on fundamental interaction mechanisms. *Nuclear Inst. and Methods in Physics Research, A* **242**, (1986).

[19] Liu, Yingzi. A Compact In Vivo Neutron Activation Analysis System to Quantify Manganese in the Human Hand Bone. *Thesis. Purdue University*. (2015)

[20] Valentin, J. & Streffer, C. Basic anatomical and physiological data for use in radiological protection: Reference values - ICRP Publication 89. *Ann ICRP* **32**, (2002).